Biological and Bioinspired Photonic Materials for Passive Radiative Cooling and Waveguiding

Norman Nan Shi

Submitted in partial fulfillment of the

requirements for the degree of

Doctor of Philosophy

in the Graduate School of Arts and Sciences

Columbia University

2018

ABSTRACT

Biological and Bioinspired Photonic Materials for Passive Radiative Cooling and Waveguiding

Norman Nan Shi

Animals have evolved diverse strategies to control solar and thermal radiations so that they can better adapt to their natural habitats. Structured materials utilized by these animals to control electromagnetic waves often surpass analogous man-made optical materials in both sophistication and efficiency. Understanding the physical mechanism behind these structured materials of nature inspires one to create novel materials and technologies.

Our optical and thermodynamic measurements of insects (Saharan silver ants and cocoons of the Madagascar comet moth) living in harsh thermal environments showed their unique ability to simultaneously enhance solar reflectivity and thermal emissivity, and to maintain a cool body temperature.

Saharan silver ants, *Cataglyphis bombycina*, forage on the desert surface during the middle of the day. The ants' conspicuous silvery glance is caused by a coating of hairs with unique triangular cross-sections. The hair coating enhances not only the reflectivity of the ant's body surface in the visible and near-infrared range of the spectrum, where solar radiation culminates, but also the emissivity of the ant in the mid-infrared. The latter effect enables the animals to efficiently dissipate heat back to the surroundings via blackbody radiation under full daylight conditions.

The fibers produced by the wild comet moth, *Argema mittrei*, are populated with a high density of air voids that have a random distribution in the fiber cross-section but are invariant along the fiber. These filamentary air voids strongly back-scatter light in the solar spectrum, which, in combination with the fibers' intrinsic high emissivity in the mid-infrared, enables the cocoon to function as an efficient radiative-cooling device, preventing the pupa inside from overheating.

The reduced dimensionality of the random voids leads to strong optical scattering in the transverse direction of the cocoon fibers. This enables tightly confined optical modes to propagate along the fibers via transverse Anderson localization. We made the first observation of transverse Anderson localization in a natural fiber and further demonstrated light focusing and image transport in the fibers. This discovery opens up the possibility to use wild silk fibers as a biocompatible and bioresorbable material for transporting optical signals and images.

Drawing inspirations from these discoveries, we designed and developed high-throughput fabrication processes to create coatings and fibers with passive radiative-cooling properties. The radiative-cooling coatings consist of various nanoparticles imbedded within a silicone thin film. The sizes and materials of the nanoparticles were chosen to provide simultaneously high solar reflectivity and thermal emissivity. The coating has been implemented in two site studies on real roofs and has demonstrated reduced roof temperature by up to 30^{o}C in the summer and associated reduction of electricity usage by up to 30%. We also made biomimetic fibers from regenerated silk fibroin and a thermoplastic using wet spinning. Spectroscopic measurements showed that these man-made fibers exhibit exceptional optical properties for radiative-cooling applications.

Table of Contents

List of Figures

Acknowledgments

Looking back at my journey at Columbia University as my work and dissertation draws to its conclusion, I am truly grateful and thankful for all the people that helped me and supported me along the way. This work would not have been possible without them.

First and foremost, I need to thank my advisor and mentor, Prof. Nanfang Yu for giving me the opportunity to continue pursue my dream by taking me on as a PhD student after my leave of absence. Thank you for believing in me. He was always there when I needed help, whether it's when I'm stuck on an experiment, or when I needed inspiration to develop new ideas. When experiments took a long time to evolve and develop, he gave me the freedom and the room to explore and devise alternative approaches, all the while offering support and encouragement. His calm demeaner, especially under pressure always made me realize things would work out, as long as I kept pushing forward. I could not have asked for a better mentor, who cared about not just my work and research, but my well-being, and for that, I'm grateful.

I would also like to thank my dissertation committee members for all their help and support over the years, from the oral qualifying exam, dissertation proposal to the defense:

Prof. James Im, who welcomed me into the materials science and engineering department at Columbia with open arms, and a smile that always made me feel at ease. Prof. Shalom Wind, who introduced to me the world of nanotechnology and nanofabrication through his interactive and informative class. Prof. Siu-Wai Chan, for offering and helping me

with practicing my dissertation presentation, and for her genuine interest in my research. Prof. Michal Lipson, who generously shared her attention and offered wonderful suggestions for my dissertation and future research. I am both honored and grateful to have all of them on my dissertation committee.

All the works presented in this dissertation are made possible by collaborations with a wonderful group of researchers in the fields of physics, engineering and biology.

I would like to thank Prof. Rüdiger Wehner (University of Zurich), Prof. Naomi Pierce (Harvard University), Prof. Gary Bernard (University of Washington), and Dr. Catherine Craig (CPALI) for introducing to me the wonderful world of entomology. Your passion and determination to learn and to understand everything you possibly can from these insects was a constant inspiration of my research. Thank you for teaching me and showing me this beautiful and fascinating research field.

I would like to thank Dr. Ming Lu, Dr. Matt Sfeir, Dr. Fernando Camino, and Kim Kissllinger, Dr. Yuan Huang (currently at CAS) and Dr. Jiabao Zheng (currently at MIT) from Brookhaven National Laboratory for teaching me about nanofabrication, ultrafast lasers, sectioning of samples and everything in between.

My appreciation goes out to all the present and past group members in Prof. Nanfang Yu's research group: Dr. Myoung-hwan Kim, Dr. Zhaoyi Li for teaching me about FTIR, optical simulation, nanofabrication and infrared optics, I will never forget our memorable journey in the snowstorm. Cheng-Chia Tsai, for always there to offer help. Adam Overvig and Sajan Shrestha for all the wonderful discussions over the years. Michael

Carter, who helped with preparing regenerated silk fibroin solutions. Dr. Guozhen Liang for teaching me about terahertz lasers.

I would like to thank Prof. Yuan Yang and Jyotirmoy Mandal for suggesting and helping me explore alternative materials for my research in radiative cooling fibers. Jyotirmoy's unique and diligent approach to research and problem solving, and his desire to create affordable and practical technologies have served as an inspiration.

I would like to thank Dr. Brian Patterson from Los Alamos National Lab for his help with nano-CT of the ant hair structures.

I would like thank Dr. April Tian for all her encouragement and support over the years, and Julian Yu for offering his thin hair to be used in building the thermodynamic measurement setup.

I would also like to thank Dr. David Soltz for inspiring me and introducing me to the world of optics. Dr. Thomas Boone, for all his encouragement and help over the years, and for helping me to continue to pursue my Ph.D. Dr. Anika kinkhabwala, for teaching me about photoluminescence, confocal microscopy, and free space optics which enabled me to jump right into graduate research. Dr. Se-heon Kim, for his guidance and support over the years and for teaching me about numerical simulations.

There are many individuals whose encouragements, help and support through the years made it possible for me to complete my dissertation: Dina Amin, Montserrat (Montse) Fernandez-Pinkley, Michael Garcia, Dr. Jiangjun Zheng, Dr. Junlin Liang, Dr. Jie Gao, Dr. Zhenda Xie. I want to thank them for their support and for sharing their knowledge.

I want to thank my family for supporting me throughout my school and career. I want to thank my wife, Christine, for always standing by my side and supporting me, and for all the joy you and Nova brought into my life.

Dedication

To my family

Chapter 1

Theory and background

1.1 Theoretical aspects of thermal radiation

1.1.1 Blackbody radiation

Blackbody radiation is defined as electromagnetic waves emitted from the surfaces of an object caused by molecular vibrations associated with the internal energy of the object. These electromagnetic waves can be characterized by the wavelength λ_0 in vacuum, and the wavelength range of interest in this study include the long-wavelength part of the ultraviolet (λ_0 = 0.35 - 0.4 μm), the visible region (λ_0 = 0.4 – 0.7 μm), the near-infrared region (λ_0 = 0.7 – 2.5 μm), and the mid-infrared region (λ_0 = 2.5 – 25 μm). At any given body surface, radiation in the form of electromagnetic waves can either be reflected by the surface, absorbed as it travels beyond the surface and into the medium of the body, or transmits and passes through the body. A body is defined as opaque when all the radiation that passes through its surface is absorbed. A combination of low surface reflectivity and high internal absorption makes a body a good absorber for incident radiation at a given wavelength of light. A material can be a good absorber at one wavelength, but transparent at a different wavelength. Glass, for example is highly transparent in the visible spectrum, but highly absorptive in the mid-infrared. A blackbody, which is a perfect absorber, is one that allows incident light waves at all

wavelengths and all incidence angles to pass into the body with zero reflection and total internal absorption. Aside from being a perfect absorber, a blackbody is also a perfect emitter, at every wavelength and at every emitting angle, as governed by the second law of thermodynamics.

The total intensity of radiation is defined as the integral of the spectral intensity over all wavelengths:

$$i_b = \int_{\lambda=0}^{\infty} i_{b\lambda}(\lambda) d\lambda \tag{1.1}$$

where i_b is the total intensity, and $i_{b\lambda}$ is the radiative intensity as a function of wavelength. The intensity of blackbody radiation is independent of the direction of emission, as is shown in Fig. 1.1a. The power of emitted radiation, however, is a function of emission direction and is defined by the equation:

$$e_{\lambda b}(\lambda, \theta, \varphi) = i_{b\lambda}(\lambda) cos\theta \tag{1.2}$$

also known as the Lambert's cosine law. Radiation generated by a diffuse surface also follows this cosine law (Fig. 1.1b).

As shown in Fig. 1.1c, the shaded area is given by dω = sinθdθdφ, and the spectral emission from an area dA to the shaded area per unit wavelength is:

$$i_{\lambda b}(\lambda) cos\theta d\omega d\lambda = i_{b\lambda}(\lambda) cos\theta sin\theta d\varphi d\lambda \tag{1.3}$$

The blackbody spectral emission over the entire hemisphere can be obtained by integrating equation 1.3 over all solid angles:

$$e_{\lambda b}(\lambda) d\lambda = i_{b\lambda}(\lambda) d\lambda \int_{\varphi=0}^{2\pi} \int_{\theta=0}^{\frac{\pi}{2}} cos\theta sin\theta d\varphi d\lambda = \pi i_{b\lambda}(\lambda) d\lambda \tag{1.4}$$

This relationship shows that the hemispherical emissive power is simply π multiplied by the blackbody intensity, a relationship that will be used later in this study.

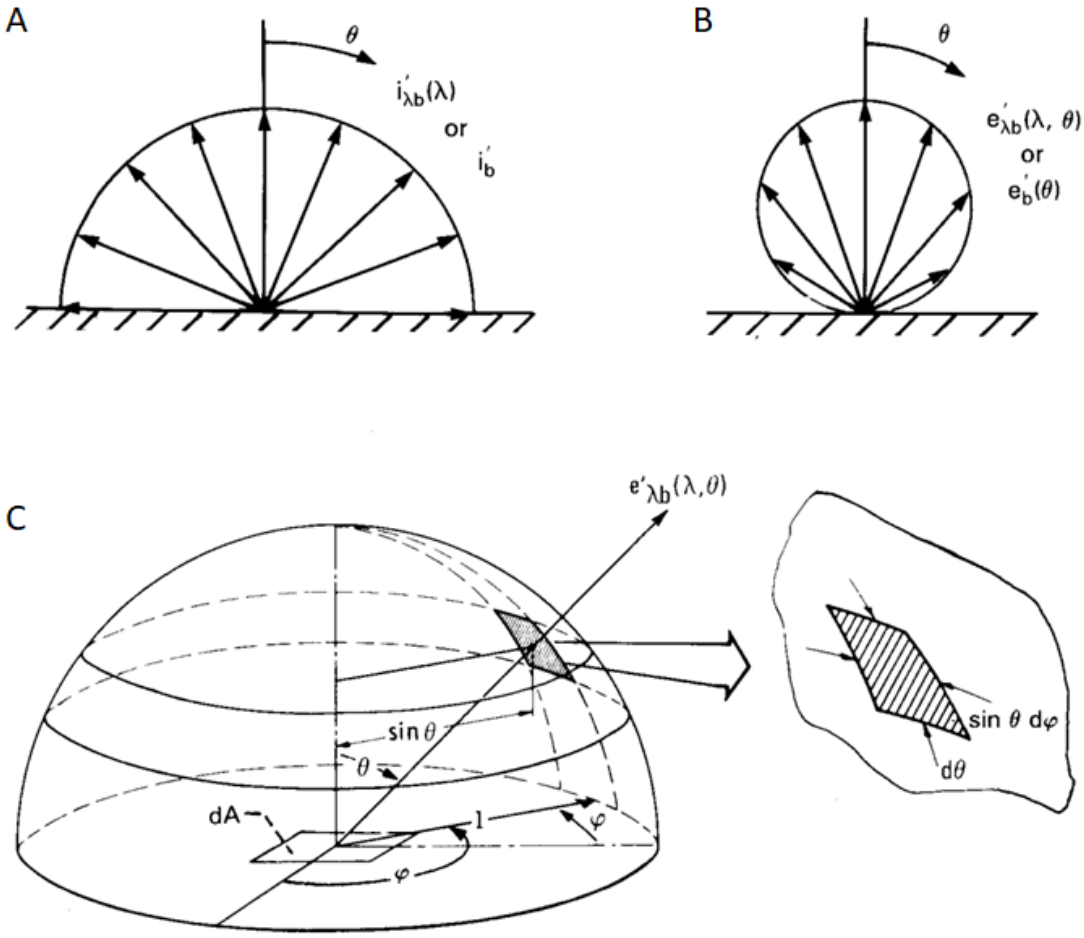

Figure 1.1 (A) Angular distribution of blackbody intensity and (B) blackbody directional emissive power. (C) Unit hemisphere used to obtain the relationship between blackbody hemispherical emissive power and intensity. All images in this figure are reproduced from [1].

1.1.2 Spectral distribution of emissive power, Planck's law and Stefan-Boltzmann Law

Radiation emitted by a blackbody has a broad spectrum distribution, with fixed amount of energy radiating at any given wavelength that's a function of temperature. The exact expression was derived by Max Planck, where the total emissive power at any given wavelength is a function of temperature:

$$e_{\lambda b}(\lambda, T) = \pi i_{b\lambda}(\lambda) = \frac{2\pi C_1}{\lambda^5 (e^{\frac{C_2}{\lambda T}} - 1)} \quad (1.5)$$

where $C_1 = hc_0^2$ and $C_2 = hc_0 / k$. Here, h is the Plank's constant, k is the Boltzmann constant and c_0 is the speed of light in vacuum.

One can also calculate the overall hemispherical total emissive power of a blackbody surface by integrating equation 1.5 over all wavelength range.

$$e_b = \int_0^\infty e_{\lambda b}(\lambda) d\lambda = \int_0^\infty \pi i_{b\lambda}(\lambda) d\lambda = \sigma T^4 \quad (1.6)$$

where σ is the Stefan-Boltzmann constant.

1.1.3 Radiation from the sun and atmospheric transparency windows

The energy exchange between an animal and its surrounding environment is complex and involves many variables. Mechanisms that can affect an animal's temperature include its metabolism, rate of water evaporation, and thermal convection, conduction, and radiation. In this section we start to build the thermodynamic model by only including radiative energy exchange.

Radiative energy exchange in an animal's natural environment includes absorption of solar radiation in the ultraviolet, visible and the near-infrared, and radiative energy

exchange between the animal's body and the surrounding environment in the mid-infrared. The sun has a temperature of ~5778 K. Using equation 1.5 and by treating it as a blackbody, it has a radiation spectrum shown in Fig. 1.2. On a clear day, the atmospheric transparency windows allow a significant amount of solar radiation to pass through the atmosphere and reach the earth surface. In this study, we use the reference solar irradiance distribution provided by American Society for Testing and Materials (ASTM) [2], which is also shown in Fig. 1.2. Furthermore, a model (MODTRAN) was developed for estimating the transmission of the atmosphere in the mid-infrared [3] (Fig. 1.2). The MODTRAN model assumes that an infrared detector is looking down at the earth at an elevation of 70 kilometers above the sea level. Thermal radiation through this mid-infrared atmospheric transparency window allows the earth to lose heat to outer space, thereby achieving an energy balance with incoming solar energy and maintaining long-term stability of its temperature.

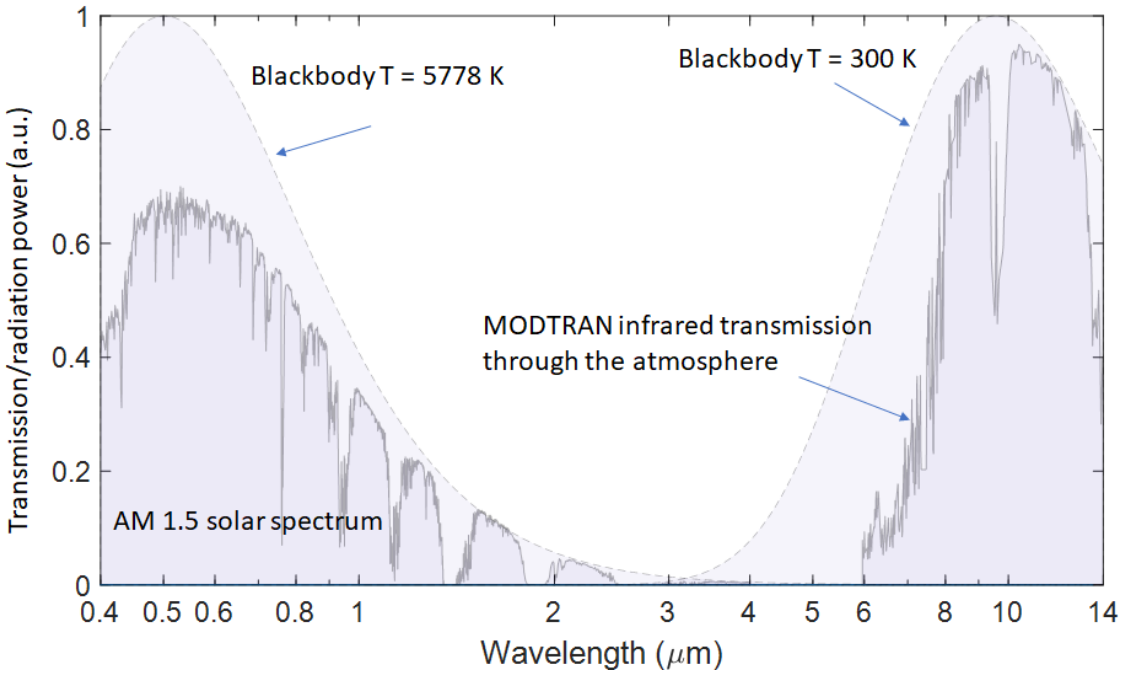

Figure 1.2 AM 1.5 solar irradiance spectrum and MODTRAN infrared transmission spectrum through the atmosphere, and blackbody radiation spectra for T = 5778 K (temperature of the sun) and T = 300 K (ambient temperature or body temperature of an animal).

1.1.4 Kirchhoff's law of thermal radiation

If an element dA (Figure 1.1C) at temperature T is placed inside an isothermal enclosure (also a blackbody) also at temperature T, to maintain the energy balance between the enclosure and the element, the intensity of radiation incident on dA from a given direction (θ, φ) has to be equal to the intensity of radiation emitting from dA in the same direction. We can express the above relationship with the following equation [1]:

$$\varepsilon_\lambda(\lambda, \theta, \varphi, T) = \alpha_\lambda(\lambda, \theta, \varphi, T) \tag{1.7}$$

In other words, Kirchhoff's law of thermal radiation can be stated as directional and wavelength-specific thermal emissivity is equal to the corresponding absorptivity.

1.1.5 Heat transfer model

In section 1.1.3, we only considered the basic terms related to radiative energy exchange. In this section, the heat transfer model between a body and its surrounding environment will be addressed in more detail.

The temporal temperature profile of an animal in its natural environment can be described by the following equation [4]:

$$C\frac{dT}{dt} = \alpha' Ps - \varepsilon\sigma T^4 s' + \alpha\sigma T_s^4 s + \alpha''\sigma T_g^4 s - hs'\left(T - T_a\right) \tag{1.8}$$

CdT/dt describes the overall rate of change in stored thermal energy. The thermal capacity $C = cw$, where c, is the specific heat (1.56 $Jg^{-1}K^{-1}$ for chitin [5]) and w is the weight of the specimen.

$\alpha' Ps$ is the absorbed power of the light source (the Sun, or the Xenon lamp in the thermodynamic measurements); α' is the absorptivity averaged over the spectrum of the light source; P is the light intensity (power per unit area) incident onto the specimen; and s is the specimen area that intersects the incoming light beam (projected area).

$-\varepsilon\sigma T^4 s'$ is the thermal radiation from the specimen to the surrounding environment, hence its negative sign; ε is the emissivity averaged over the entire surface of the specimen and averaged over the spectrum of a blackbody at temperature T; σ is the Stefan-Boltzmann constant 5.67×10^{-8} $Wm^{-2}K^{-4}$; and s' is the surface area of the specimen.

$\alpha\sigma T_s^4 s$ is the absorption of blackbody radiation from the sky; α is absorptivity of the specimen averaged over the spectrum of a blackbody at temperature T_s, the radiative temperature of the sky [6].

$\alpha''\sigma T_g^4 s$ is the absorption of blackbody radiation from the terrestrial environment; α'' is absorptivity of the specimen averaged over the spectrum of a blackbody at temperature T_g, the temperature of the surface of the terrestrial environment.

$hs'(T-T_a)$ is the power transferred through thermal convection; h is heat transfer coefficient; and T_a is the ambient temperature.

Note that α and α'' may have different values: in the case of the silver ants, the absorptivity of the hairy top and lateral sides of their body differs from that of the bald ventral body surface. We assume that there is minimal heat transfer through conduction: for example, the thin long legs of the desert ants minimize thermal conduction from the desert floor [7].

In order to obtain analytical solution from equation (1.8), the thermal radiation term $\varepsilon\sigma T^4 s'$ can be linearized in the following way:

$$\varepsilon\sigma T^4 s' = \varepsilon\sigma s'\left(T_{avg} + T - T_{avg}\right)^4 = \varepsilon\sigma s' T_{avg}^{\ 4}\left(1+\frac{T-T_{avg}}{T_{avg}}\right)^4$$
$$\approx \varepsilon\sigma s' T_{avg}^{\ 4}\left(1+4\frac{T-T_{avg}}{T_{avg}}\right) = \varepsilon\sigma s' T_{avg}^{\ 4} + 4\varepsilon\sigma s' T_{avg}^{\ 3}\left(T-T_{avg}\right) = 4\varepsilon\sigma s' T_{avg}^{\ 3} T - 3\varepsilon\sigma s' T_{avg}^{\ 4} \quad (1.9)$$

Equation (1.8) can then be simplified to:

$$C\frac{dT}{dt} = -\left(4\varepsilon\sigma s' T_{avg}{}^3 + hs'\right)T + \left(3\varepsilon\sigma s' T_{avg}{}^4 + \alpha' Ps + \alpha\sigma T_s^4 s + \alpha'' \sigma T_g^4 s + hs' T_a\right) \equiv -BT + A \tag{1.10}$$

where $B = \left(4\varepsilon\sigma s' T_{avg}{}^3 + hs'\right)$ and $A = \left(3\varepsilon\sigma s' T_{avg}{}^4 + \alpha' Ps + \alpha\sigma T_s^4 s + \alpha'' \sigma T_g^4 s + hs' T_a\right)$

Solving the ordinary differential equation above, the temperature T of the specimen can be expressed as

$$T \propto \pm \exp\left(-\frac{B}{C}t\right) \tag{1.11}$$

where

$$\tau_r = \tau_d = \frac{C}{B} = \frac{C}{4\varepsilon\sigma s' T_{avg}{}^3 + hs'} \qquad \text{(in air)} \tag{1.12}$$

is the rise and decay time constant characterizing the specimen's temperature change. This equation shows that the time constants are proportional to the thermal capacity, *C*, of the specimen, and inversely proportional to the sum of radiative and convective heat transfer rates. The equation also shows that the rise and decay time constants are identical.

For thermodynamic measurements performed in vacuum, the equation can be further simplified by taking out the effect that is due to convective heat transfer (setting parameter *h* to zero). The rise and decay time constants can then be expressed as

$$\tau_r = \tau_d = \frac{C}{4\varepsilon\sigma s' T_{avg}{}^3} \qquad \text{(in vacuum)} \tag{1.13}$$

The specimen reaches its equilibrium body temperature when dT/dt is equal to zero, i.e., when there is no net heat transfer. For vacuum experiments without convective heat transfer, the resulting relationship is:

$$\varepsilon\sigma T^4 s' = \alpha' P s + \alpha\sigma T_s^4 s + \alpha'' \sigma T_g^4 s \quad \text{(in vacuum)} \tag{1.14}$$

with the equilibrium temperature:

$$\mathrm{T} = [\frac{1}{\varepsilon\sigma s'}(\alpha' P s + \alpha\sigma T_s^4 s + \alpha'' \sigma T_g^4 s)]^{1/4} \approx \left(\frac{\alpha' P s}{\varepsilon\sigma s'}\right)^{1/4} \qquad \text{(in vacuum)} \tag{1.15}$$

when blackbody radiation from the sky and the terrestrial environment is small as compared to the radiation from the sun or Xenon lamp (as it has been the case in the thermodynamic measurements), the equilibrium temperature is proportional to α', i.e., the absorptivity of the specimen averaged over the solar spectrum, and inversely proportional to ε, i.e., the emissivity of the specimen in the mid-infrared.

In the presence of convection and at thermal equilibrium, according to equation (1.8) we have

$$\alpha' P s - \varepsilon\sigma T^4 s' + \alpha\sigma T_s^4 s + \alpha'' \sigma T_g^4 s - h s' (T - T_a) = 0 \qquad \text{(in air)} \tag{1.16}$$

The equilibrium temperature T can be obtained by numerically solving the above equation.

1.2 Reflection and scattering of light

1.2.1 Reflection and refraction at an optical interface for polarized light

Consider an interface between two optically smooth dielectric media where the refractive indices for the two media are n_1 and n_2. When a polarized light beam is incident upon the interface at an angle from the side with lower refractive index, a portion of the light is reflected, and the rest is transmitted through. The reflection and transmission coefficients are functions of the incident angle and the refractive indices of the two media, also known as the Fresnel equations:

$$r_x = \frac{n_1 cos\theta_1 - n_2 cos\theta_2}{n_1 cos\theta_1 + n_2 cos\theta_2}$$

$$r_y = \frac{n_1 sec\theta_1 - n_2 sec\theta_2}{n_1 sec\theta_1 + n_2 sec\theta_2}$$

$$t_x = 1 + r_x$$

$$t_y = \left(1 + r_y\right) \frac{cos\theta_1}{cos\theta_2}$$

(1.17)

where r_x and r_y are the reflection coefficients for TE and TM polarized light, respectively, as defined by Fig. 1.3A, and θ_1 and θ_2 are governed by Snell's law:

$$n_1 sin\theta_1 = n_2 sin\theta_2 \tag{1.18}$$

While r_x increases continuously as a function of incident angle, r_y does reach a point where no light is reflected, this position is known as the Brewster's angle. From equation (1.18), we can show that the Brewster angle is:

$$\theta_B = \arctan (n_2 / n_1) \tag{1.19}$$

While the Brewster angle only occurs when n_1 is smaller than n_2, total internal reflection can occur when n_1 is larger than n_2, and again using equation (1.18), we can show that the critical angle where total internal reflection starts to occur is

$$\theta_c = \arcsin (n_2 / n_1) \tag{1.20}$$

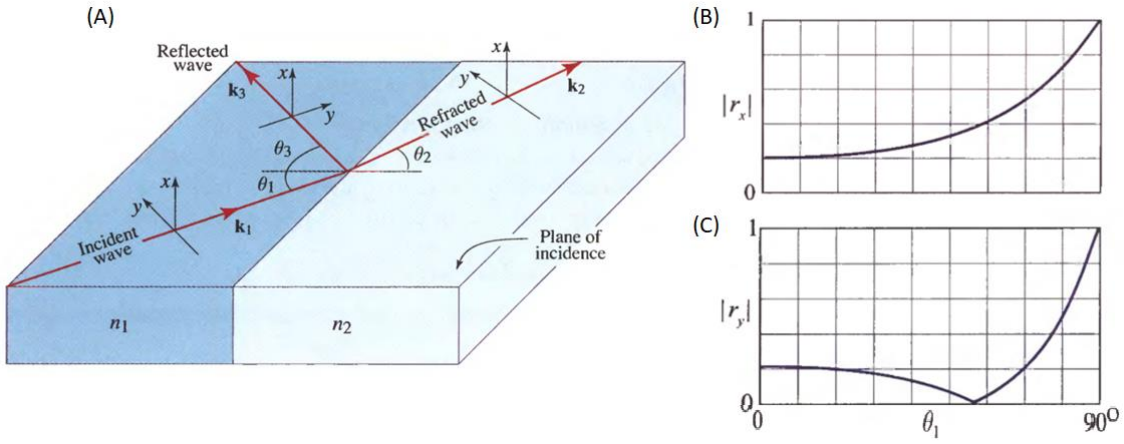

Figure 1.3 (A) Schematic diagram of the reflection and refraction at the boundary between two dielectric media. (B) Reflection coefficient for TE polarized light as a function incident angle θ_1. (C) Reflection coefficient for TM polarized light as a function of incident angle θ_1. All images in this figure are reproduced from [8].

1.2.2 Effective medium theory

Consider a material composed of a periodic array of fine structures. When estimating the reflection and transmission of light interacting with the material, as the wavelength of light becomes significantly larger than the constitutive structures at the interface and within the material, an approximation known as the effective medium theory is often used to estimate and describe the optical properties of the material. A zeroth-order approximation is used when the size and periodicity of the structure is much smaller than the wavelength of light, while a second-order approximation is used when the size and periodicity of the structure is smaller, but do begin to support higher-order diffraction waves, the two approximations are presented below [9]:

Zeroth-order approximation:

$$\varepsilon_{TE}^{(0)}(\mathrm{z}) = f(\mathrm{z})\varepsilon_s + (1-f(\mathrm{z}))\varepsilon_i \ ,$$

$$\frac{1}{\varepsilon_{TM}^{(0)}(\mathrm{z})} = \frac{f(\mathrm{z})}{\varepsilon_s} + \frac{(1-f(\mathrm{z}))}{\varepsilon_i} \ , \tag{1.21}$$

Second-order approximation

$$\varepsilon_{TE}^{(2)}(\mathrm{z}) = \varepsilon_{TE}^{(0)}(\mathrm{z})\left[1+\frac{\pi^2}{3}\left(\frac{\Lambda}{\lambda}\right)^2 f^2(\mathrm{z})[1-f(\mathrm{z})]^2 \frac{(\varepsilon_s-\varepsilon_i)^2}{\varepsilon_0\varepsilon_{TE}^{(2)}(\mathrm{z})}\right] ,$$

$$\varepsilon_{TM}^{(2)}(\mathrm{z}) = \varepsilon_{TM}^{(0)}(\mathrm{z})\left[1+\frac{\pi^2}{3}\left(\frac{\Lambda}{\lambda}\right)^2 f^2(\mathrm{z})[1-f(\mathrm{z})]^2(\varepsilon_s-\varepsilon_i)^2 \frac{\varepsilon_{TE}^{(2)}}{\varepsilon_0}\left(\frac{\varepsilon_{TM}^{(0)}(\mathrm{z})}{\varepsilon_i\varepsilon_s}\right)^2\right] \tag{1.22}$$

The equation set (1.21) corresponds to the zeroth-order approximation of the effective permittivity of the interface for TE and TM incident light. Here *f* is the filling factor at a

given layer of the effective medium marked by its z position. Λ is the width of the structure's cross section, ε_s and ε_i are the permittivity of the constitutive structures and air, respectively, and λ is the wavelength of interest. This estimation is accurate only when wavelength is much larger than individual structures. When wavelength is only a few times larger than the structure (e.g., mid-infrared light interacting with hair structures of the silver ants), the second-order approximation is used, as shown above in equation set (1.22).

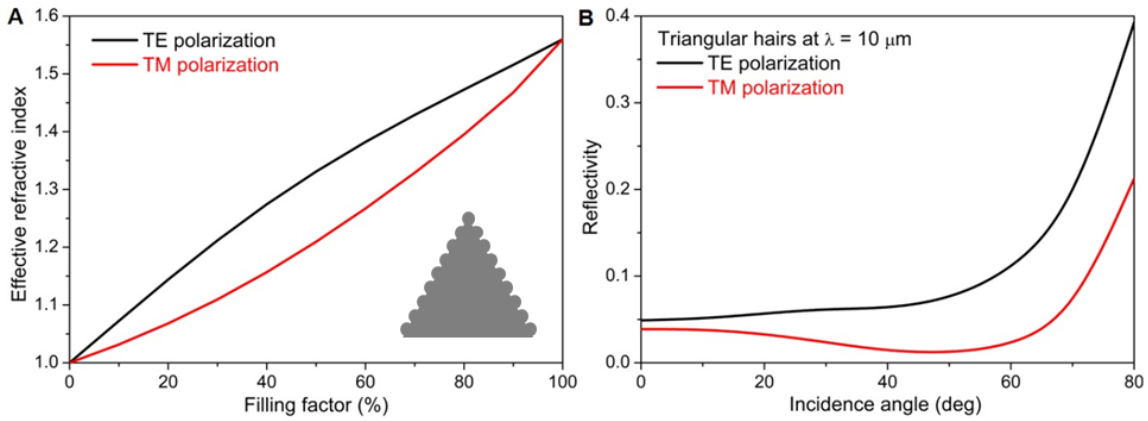

Figure 1.4 (**A**) Theoretically calculated effective index of a layer of triangular hairs as a function of the filling factor (percentage of space filled with the chitin-protein complex). Zero filling factor represents the apexes of the triangles, where the effective refractive index n_{eff} = 1.0 is matched with that of free space. Filling factor of 100% corresponds to the cuticular surface (refractive index of cuticle: 1.56; we here assume that there is no gap between triangular hairs and the cuticle). (**B**) Simulated reflectivity spectra of a single layer of triangular hairs situated on a cuticular substrate at λ = 10 μm for TE and TM polarizations. Reflectivity is uniformly lower (i.e., emissivity uniformly higher) for TM polarization at all incidence angles.

As an example, we calculated the effective refractive index of a layer of triangular hairs (2 μm high, and 2 μm wide) of n=1.56 on a substrate of n=1.56 using the second-order approximation of the effective medium theory, and reflectivity as a function of incidence angle for both TE and TM light waves with λ=10 μm(Fig. 1.4).

1.2.3 Mie scattering and dielectric resonators

In 1908, Gustav Mie published a paper where he rigorously explained the theory behind optical phenomena associated with gold colloidal particles [10]. The work explored the interaction of electromagnetic waves with spheres that are smaller than or comparable to the wavelength of light, and enabled the understanding of the color of gold colloids due to the scattering and absorption of light. The theory demonstrated for the first time how light can be controlled by nanoscaled resonant scatterers.

As one fast forwards to present day, optical resonances in metallic and dielectric nanostructures have enabled the development of a broad range of applications such as solar cells and hard drive technologies, and new research fields such as metasurfaces [11]–[13].

Due to the high losses of metal plasmonic resonators, dielectric resonators, especially high refractive index dielectric resonators, have become an increasingly attractive candidate for a wide range of applications due to its low optical losses, and also their abilities to control both electric and magnetic field components of light waves.

To demonstrate the optical properties of a dielectric resonator, we use a simple spherical particle as an example, and use numerical methods to illustrate how optical resonances arise in dielectric nanostructures.

In this numerical model, a broadband plane-wave light source is incident onto a lossless dielectric sphere, which has a refractive index of 3 and a radius of 100 nm. The scattering properties of a Mie resonator is a function of its shape, size, the dielectric permittivity ε and the wavelength of light λ. In this particular example, the fundamental resonance mode of the sphere, characterized by enhanced scattering, lies at $\lambda \sim 623$ nm, and a second-order mode at $\lambda \sim 430$ nm. The fundamental mode shown here is the magnetic dipole mode of the sphere. The resonant dipole is created as a result of coupling of incoming polarized light to circular displacement currents of the electric field, where phase retardation inside the particle plays an important role [14]. As the size or the refractive index of the sphere increases, the fundamental resonance modes will shift to larger wavelengths, and a number of higher-order modes appear at shorter wavelengths. At these resonance modes, the scattering strength is enhanced both in the forward and backward direction, and stronger scattering strength is normally observed for materials with higher refractive indices. It's also interesting to note that resonance modes with high scattering strength are not only observed in spherical particles; studies have shown similar resonance modes in disks, cylinders and rings as well. By varying the size, shape and refractive index of these dielectric structures, one can achieve strong resonance modes covering a large span of the solar spectrum, as will be discussed in further detail in Chapter 3.

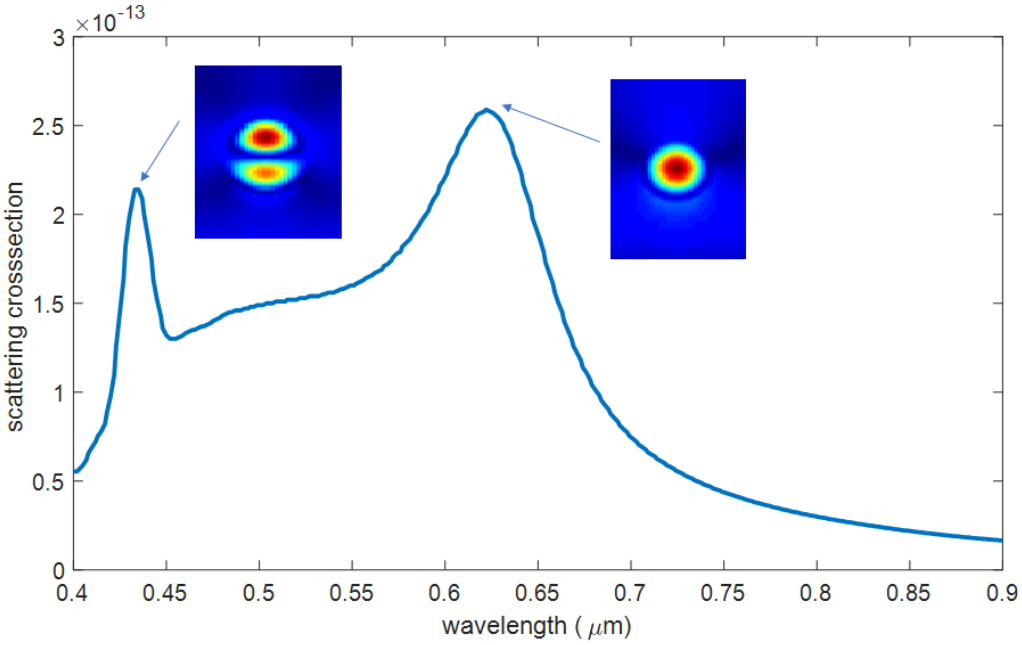

Figure 1.5 Numerically calculated scattering cross section spectrum for a dielectric sphere with n = 3 and radius of 100 nm. The two distinct response peaks are the fundamental (magnetic dipole) and second-order (magnetic quadrupole) resonance modes of the dielectric sphere. The magnitude of the cross-sectional magnetic field of the two modes are shown as insets.

1.3 Anderson localization

1.3.1 Anderson localization

The concept of localization was first proposed by Philip Warren Anderson in 1958 [15], who studied spin diffusion and electronic conduction in random lattices. The concept of mean free path was introduced with the classical Drude model to describe conduction and diffusion of electrons in a solid. In this model, electrons bounce between heavy, stationary ions sitting at the metal lattice sites, and the average length an electron travels before it collides with an ion is used to characterize the material's electrical conductivity. With the introduction of quantum mechanics, the model was modified, where only impurities introduced into a perfect lattice act as scattering centers that affect the mean free path of the electrons traveling in a metal. As the density of the defects increases to a critical value, Anderson pointed out that the electron movement can no longer be characterized by the diffusion model, and that electrons become completely localized and conductivity comes to a halt.

The original study went unnoticed for over a decade [16], until the concept became broadly adopted by the physics community, and remains a heavily studied field today. The concept of localization is not limited to electrons, but has been extensively studied for light, microwave, and ultrasound waves.

To experimentally observe the effect of Anderson localization of light, researchers need a scattering medium composed of scatterers with high refractive indices, minimal absorption, and small sizes compared to the wavelength of light. Experimental demonstrations of Anderson localization of light have been reported in scattering media

composed of Titania powders and grounded Gallium Arsenide powders; however, debates still exist to this day on the interpretation of the measurement results for three-dimensional materials [17]–[19]. In three-dimensional systems, localization effects are characterized by the transport length l^* and the Ioffe-Regel condition, which states that Anderson localization can be observed when the system satisfies the criterium $kl^* \sim 1$, where k is the wavevector inside the medium. While it is extremely challenging to realize Anderson localization in bulk media, coherent waves can always be localized in one-dimensional and two-dimensional systems [20]. Localization of light in optical media with reduced dimensionality gives rise to an interesting phenomenon called transverse Anderson localization, which will be studied in detail in the second half of Chapter 4.

1.3.2 Transverse Anderson localization

Transverse Anderson localization was first introduced in 1989 [21], but experimental demonstration of this phenomenon was not realized until 2007 [22]. In the experiments, a gaussian beam was launched into a photo-refractive crystal, where a disordered lattice was introduced by photo-refractive effects [23]. By increasing the disorder of the lattice in the transverse direction, while maintaining invariance in the propagation direction of the beam, researchers observed transverse localization of the beam, i.e., a constant beam profile along the propagation direction and exponential decay of optical intensity in the transverse direction. By fitting the intensity profile of the localized beam exiting the crystal, they obtained a localization length of $\xi = 64\ \mu m$. The localization length is a function of the level of disorder, density of defects, and the refractive index contrast between the defect and background material. A defect filling fraction of close to 50%,

and a high refractive index contrast between the defect and the background material have further reduced the localization length to ~ 31 μm in recent studies [24]. Since then, researchers have explored potential applications utilizing transverse Anderson localization for image transport, light focusing and secure information transport [25]–[28].

1.4 References

[1] R. S. John R. Howell, M. Pinar Menguc, *Thermal Radiation Heat Transfer*, 5th ed. Taylor & Francis Group, 2011.

[2] R. E. Bird, R. L. Hulstrom, and L. J. Lewis, "Terrestrial solar spectral data sets," *Sol. Energy*, vol. 30, no. 6, pp. 563–573, 1983.

[3] D. C. Berk, Alexander ; Bernstein, Lawrence S ; Robertson, "MODTRAN: A Moderate Resolution Model for LOWTRAN," *Def. Tech. Inf. Cent.*, vol. 3, 1987.

[4] D. M. Gates, *Biophysical Ecology*. New York, NY: Springer New York, 1980.

[5] R. Muzarelli, *Chitin*. Pergamon Press, 1977.

[6] J. L. Monteith and W. E. Reifsnyder, "Principles of Environmental Physics," *Phys. Today*, vol. 27, no. 3, pp. 51–52, Mar. 1974.

[7] S. Sommer and R. Wehner, "Leg allometry in ants: Extreme long-leggedness in thermophilic species," *Arthropod Struct. Dev.*, vol. 41, no. 1, pp. 71–77, Jan. 2012.

[8] B. E. A. Saleh and M. C. Teich, *Fundamentals of Photonics*. New York, USA: John Wiley & Sons, Inc., 1991.

[9] D. H. Raguin and G. M. Morris, "Analysis of antireflection-structured surfaces with continuous one-dimensional surface profiles," *Appl. Opt.*, vol. 32, no. 14, p. 2582, May 1993.

[10] G. Mie, "Beiträge zur Optik trüber Medien, speziell kolloidaler Metallösungen," *Ann. Phys.*, vol. 330, no. 3, pp. 377–445, 1908.

[11] W. A. Challener, C. Peng, A. V. Itagi, D. Karns, W. Peng, Y. Peng, X. Yang, X. Zhu, N. J. Gokemeijer, Y.-T. Hsia, G. Ju, R. E. Rottmayer, M. A. Seigler, and E. C. Gage, "Heat-assisted magnetic recording by a near-field transducer with efficient optical energy transfer," *Nat. Photonics*, vol. 3, no. 4, pp. 220–224, Apr. 2009.

[12] H. A. Atwater and A. Polman, "Plasmonics for improved photovoltaic devices," *Nat. Mater.*, vol. 9, no. 3, pp. 205–213, Mar. 2010.

[13] N. Yu, P. Genevet, M. A. Kats, F. Aieta, J.-P. Tetienne, F. Capasso, and Z. Gaburro, "Light Propagation with Phase Discontinuities: Generalized Laws of Reflection and Refraction," *Science (80-.).*, vol. 334, no. 6054, pp. 333–337, Oct. 2011.

[14] A. I. Kuznetsov, A. E. Miroshnichenko, M. L. Brongersma, Y. S. Kivshar, and B. Luk'yanchuk, "Optically resonant dielectric nanostructures," *Science (80-.).*, vol. 354, no. 6314, p. aag2472, Nov. 2016.

[15] P. W. Anderson, “Absence of Diffusion in Certain Random Lattices,” *Phys. Rev.*, vol. 109, no. 5, pp. 1492–1505, Mar. 1958.

[16] A. Lagendijk, B. van Tiggelen, and D. S. Wiersma, “Fifty years of Anderson localization,” *Phys. Today*, vol. 62, no. 8, pp. 24–29, Aug. 2009.

[17] S. John, “Electromagnetic Absorption in a Disordered Medium near a Photon Mobility Edge,” *Phys. Rev. Lett.*, vol. 53, no. 22, pp. 2169–2172, Nov. 1984.

[18] P. W. Anderson, “The question of classical localization A theory of white paint?,” *Philos. Mag. B*, vol. 52, no. 3, pp. 505–509, Sep. 1985.

[19] A. A. Chabanov, M. Stoytchev, and A. Z. Genack, “Statistical signatures of photon localization,” *Nature*, vol. 404, no. 6780, pp. 850–853, Apr. 2000.

[20] P. W. ANDERSON, “Scaling Theory of Localization: Absence of Quantum Diffusion in Two Dimensions,” 2005, pp. 537–541.

[21] H. De Raedt, A. Lagendijk, and P. de Vries, “Transverse Localization of Light,” *Phys. Rev. Lett.*, vol. 62, no. 1, pp. 47–50, Jan. 1989.

[22] T. Schwartz, G. Bartal, S. Fishman, and M. Segev, “Transport and Anderson localization in disordered two-dimensional photonic lattices,” *Nature*, vol. 446, no. 7131, pp. 52–55, 2007.

[23] N. K. Efremidis, S. Sears, D. N. Christodoulides, J. W. Fleischer, and M. Segev, “Discrete solitons in photorefractive optically induced photonic lattices,” *Phys. Rev. E*, vol. 66, no. 4, p. 46602, Oct. 2002.

[24] S. Karbasi, R. J. Frazier, C. R. Mirr, K. W. Koch, and A. Mafi, “Fabrication and

Characterization of Disordered Polymer Optical Fibers for Transverse Anderson Localization of Light," *J. Vis. Exp.*, no. 77, Jul. 2013.

[25] S. Karbasi, R. J. Frazier, K. W. Koch, T. Hawkins, J. Ballato, and A. Mafi, "Image transport through a disordered optical fiber mediated by transverse Anderson localization," *Nat. Commun.*, vol. 5, pp. 5–6, 2014.

[26] M. Leonetti, S. Karbasi, A. Mafi, and C. Conti, "Light focusing in the Anderson regime," *Nat. Commun.*, vol. 5, pp. 1–6, 2014.

[27] M. Leonetti, S. Karbasi, A. Mafi, E. Delre, and C. Conti, "Secure information transport by transverse localization of light," *Nat. Publ. Gr.*, no. June, pp. 1–7, 2016.

[28] J. ZHAO, J. E. Antonio-Lopez, R. A. Correa, A. Mafi, M. Windeck, and A. Schülzgen, "Image Transport Through Silica-Air Random Core Optical Fiber," in *Conference on Lasers and Electro-Optics*, 2017, p. JTu5A.91.

Chapter 2

Materials and techniques

2.1 Materials

2.1.1 Chitin

The hairs of the Saharan silver ants are mainly composed of chitin $(C_8H_{13}O_5N)_n$, which is a long-chain polymer commonly found in the natural world. It is the characteristic composite of the exoskeletons of arthropods, including crustaceans (such as crabs and shrimps) and insects. The optical properties of chitin have not been studied thoroughly due to the difficulty in the production of optical-grade materials and its various derivatives depending on the sources. An average refractive index of 1.56 has been used in many publications and previous studies reported the dispersive complex refractive indices of shrimp chitin samples only in the UV and visible spectral range (λ = 250–750 nm) [1], [2]. Here, the dispersive complex refractive indices of chitin in the mid-infrared range (λ = 2.5–20 μm) were derived from spectra measured from butterfly wing membranes.

Table 2.1 Parameters used in the Lorentz oscillator model of chitin

#	Resonant frequency (cm^{-1})	Resonant wavelength (μm)	$\lambda_p=2\pi c/\omega_p$ (μm)	$2\pi\gamma$ (10^{15} Hz)	Origin
1	3284	3.0451	21	0.05	O-H, N-H stretching
2	2920	3.4247	48	0.025	C-H stretching
3	1651	6.0569	37.8	0.01	Amide I (C-O stretching)
4	1547	6.4641	46.2	0.01	Amide II (N-H stretching)
5	1456	6.8681	66	0.01	C-H bending
6	1383	7.2307	74.4	0.01	CH_x deformation
7	1306	7.6570	75.6	0.015	Amide III
8	1244	8.0386	52.2	0.018	NA
9	1157	8.6430	115.8	0.005	C_3-OH
10	1115	8.9686	122.4	0.006	C_3-OH
11	1076	9.2937	87	0.006	C_6-OH
12	1034	9.6712	73.2	0.01	C-O-C bridge stretching
13	690	14.4928	36	0.055	NA

The chemical composition and molecular structure of chitin have been identified using various methods including infrared spectroscopy and X-ray diffraction [3], [4]. Thirteen resonance frequencies in the mid-infrared spectral range corresponding to the major vibrational and rotational bands of chitin molecules (Table 2.1) have been characterized and applied in the Lorentz oscillator model [5],

$$\frac{\varepsilon(\omega)}{\varepsilon_0}=1+\sum_m\left[\varepsilon_r\left(\omega_{0,m},\omega_{p,m},\gamma_m\right)+i\varepsilon_i\left(\omega_{0,m},\omega_{p,m},\gamma_m\right)\right]=1+\sum_m\left[\frac{\omega_{p,m}^2\left(\omega_{0,m}^2-\omega^2\right)}{\left(\omega_{0,m}^2-\omega^2\right)^2+\omega^2\gamma_m^2}+i\frac{\omega_{p,m}^2\gamma_m\omega}{\left(\omega_{0,m}^2-\omega^2\right)^2+\omega^2\gamma_m^2}\right] \quad (2.1)$$

to calculate the complex refractive indices $n_c(\omega) = n(\omega) + ik(\omega) = \sqrt{\varepsilon(\omega)}$, which were then used in the transfer matrix method to calculate the absorption spectrum of a thin film of chitin. In equation (2.1), *m* labels the various vibrational and rotational bands of chitin, and $\varepsilon_o = 8.854 \times 10^{-12}$ $C^2N^{-1}m^{-2}$ is the permittivity of free space, and $\omega_{o,m}$ is the m^{th} resonance frequency. The values of plasma frequency, $\omega_{p,m}$, and collision frequency, γ_m, were simultaneously tuned to obtain the best fit between the calculated absorption spectrum and a measured spectrum from a piece of butterfly wing membrane with scales carefully removed, which can be considered as a relatively flat slab with a uniform thickness. The absorption spectrum of the scale-less wing membrane was measured using a Fourier transform infrared spectrometer and its thickness was determined using a scanning electron microscope.

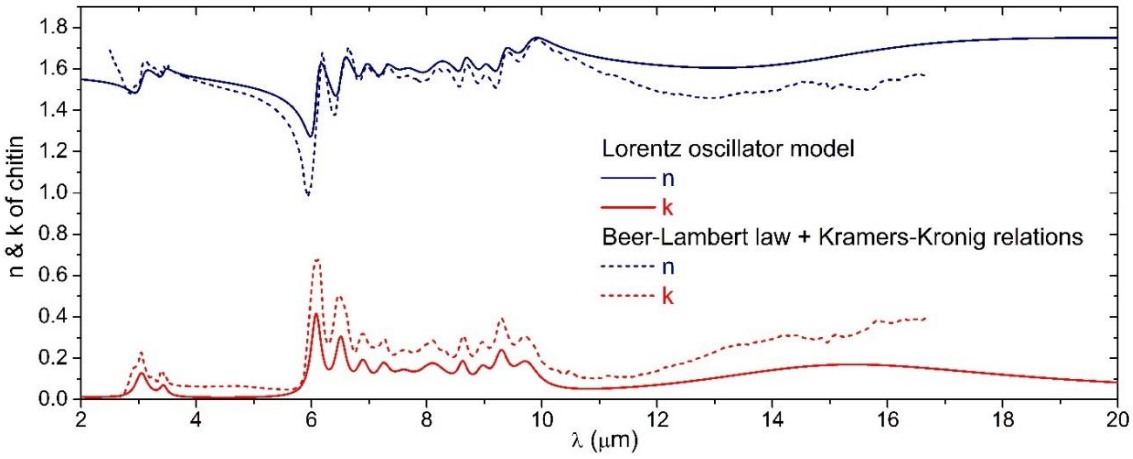

Figure 2.1 Complex refractive indices of chitin in the infrared obtained using two methods. Solid curves were obtained using the Lorentz oscillator model and transfer matrix method, which considers multiple-beam interference effects (i.e., multiple reflection of light inside chitin thin films). Dashed curves are obtained based on the Beer-Lambert law and Kramers-Kronig relations: the red dashed curve is the extinction coefficient, *k*, directly calculated from the measured absorption spectrum using the Beer-Lambert law, and the navy blue dashed curve is the corresponding real part of the complex refractive index calculated using the Kramers-Kronig relations. Because the Beer-Lambert law only considers a single pass of light through chitin thin films, the extinction coefficient is overestimated. We used the values based on the Lorentz oscillator model and transfer matrix method (solid curves) for full-wave simulations of the interactions between infrared light and nano-structured ant hairs.

2.1.2 Silkworm fibers and silk protein

Silkworms produce silk-protein (polyamino acid) based cocoon fibers to protect themselves from their surrounding environment. The material exhibits extraordinary mechanical properties such as high tensile strength and extensibility. The material is also biocompatible and bioabsorbable, making it a good candidate for biomedical applications [6], [7].

Natural silk fibers come in many different shapes and forms, exhibiting different compositions, structures, and mechanical and optical properties. Spider silk fibers are known to have superior mechanical properties compared to silk produced by domestic silkworms, but under the right spinning conditions, regenerated silk fibroin (from domestic silkworm) fibers have been shown to exhibit mechanical strength comparable to spider silk fibers [8].

Silk fibroin protein is primary composed of a recurring amino acid sequence (Gly-Ser-Gly-Ala-Gly-Ala)$_n$ (Fig. 2.2). These proteins form layers of antiparallel beta sheets (the main composition of silk fibroin), contributing to the silk's superior tensile strength, rigidity and extensibility.

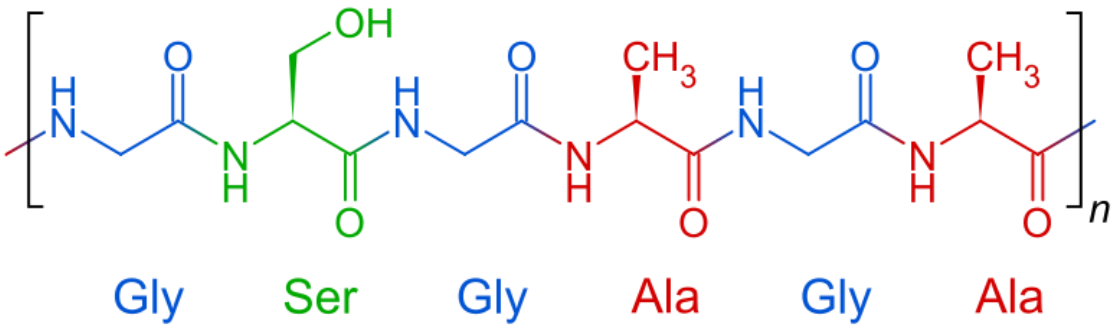

Figure 2.2 Primary structure of silk fibroin, $(Gly\text{-}Ser\text{-}Gly\text{-}Ala\text{-}Gly\text{-}Ala)_n$. Figure reproduced from [9].

The backbone of these protein molecules gives rise to high absorption in the mid-infrared, with the N-H stretching, alkyl and Amide bands representing the strongest absorption peaks. The strength and position of the absorption peaks vary depending on the sources of silk, but the absorption spectra all have a significant overlap with the mid-infrared atmospheric transparency window and the radiation spectrum corresponding to the ambient temperature.

2.2 Morphology characterization

2.2.1 SEM/FIB dual beam system

All the cross-sectional images shown in this thesis were prepared with a focused ion beam/scanning electron microscopy dual system (FEI Helios NanoLab DualBeam). This system allows us to mill a specimen with a high-energy focused Gallium ion beam and image the exposed cross-sections using SEM.

Due to accumulation of electrons on the surface of non-conductive materials, all specimens were sputtered with a 10-nm layer of gold before SEM/FIB sessions. All biological specimens were dried and degassed in a low vacuum chamber to minimize contamination to the sputtering chamber and the SEM/FIB chamber.

Before FIB milling, a layer of 500-nm Platinum was deposited on top of a specimen at the position of an intended cross-sectional cut to protect the milling edge from milling

induced damages. A high-current ion beam (Ga^+, 30 kV, 21 nA) was then used to cut through the specimen and expose a cross-section, followed by using a small-current ion beam (30 kV, 0.96-2.8nA) to polish the cross-sectional surface. The cross-section was then imaged using a scanning electron beam (5 kV, 85 pA).

2.3 Direct laser writing lithography

A direct laser write lithography process based on two-photon polymerization was used to create biomimetic optical materials. The 3D lithography system is a commercial instrument designed and built by Photonic Professional GT, Nanoscribe GmbH. It is a powerful platform for creating complex three-dimensional micro- and nanostructures with resolution of ~200 nm in the horizontal plane and of ~1 μm in the vertical direction. Suspended structures fabricated with this technique, however, have to include supporting structures and channels for the developer to dissolve unexposed photoresists.

An acrylic-based photoresist (IP-DIP, Nanoscribe GmbH) was used. It has a refractive index matching with that of the 63×, 1.4 N.A. emersion objective lens used in the system. A femtosecond fiber laser with a pulse width of 100 fs, a repetition rate of 80 MHz, and wavelength of ?? nm was used as the light source. The lens focuses emission from the laser to form a confined voxel in the photoresist to induce two-photon absorption and polymerization (Fig 2.3B). During the direct laser writing process, the photoresist was drop-casted on a transparent glass substrate and immersed with the objective lens. The lens was first brought to focus at the interface of the glass and the photoresist. A scanning galvo-mirror system was then used to control the writing in the x and y directions, while

a piezoelectric stage was used to control the writing in the z direction. A laser power of 65 mW and a scanning speed of 50 mm/s were used during the writing process.

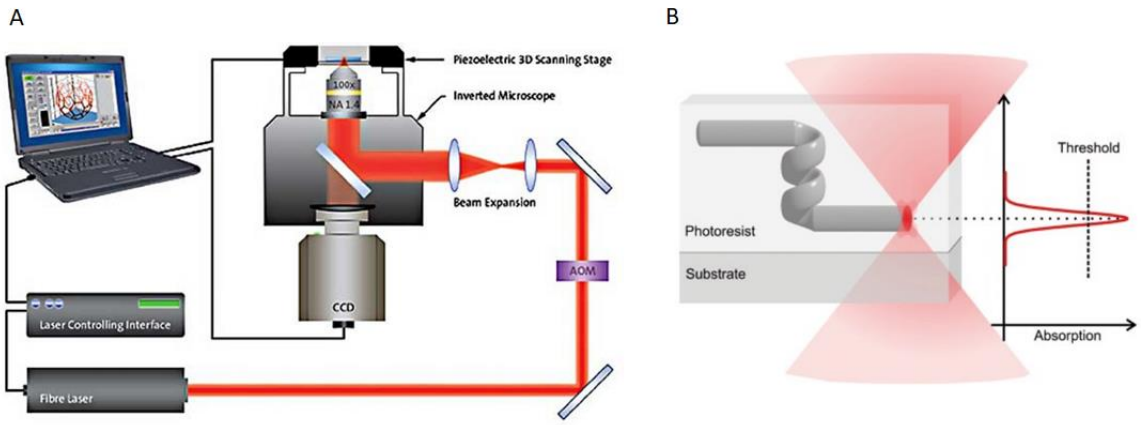

Figure 2.3 (A) Schematic diagram of the Nanoscribe direct laser writing lithography system. (B) Formation of the voxel and the writing process. Images reproduced from [10].

2.4 Optical characterization techniques

2.4.1 Hemispherical reflection and transmission measurements

Reflection and transmission measurements in the visible and near-infrared were carried out using a Fourier-transform-based spectrometer (Bruker Vertex 80) equipped with a laser stabilized high brightness Xenon plasma light source (Energetiq eq-99). Forward or backward scattered light was captured with a 2-inch visible/near-infrared integration sphere (Thorlabs IS200-4), coupled with a set of Silicon and Indium Gallium Arsenide

detectors. To measure transmission spectra, specimens were placed at the entrance port of the integration sphere so that forward scattered light waves were captured by the integration sphere. To measure reflection spectra, specimens were loaded onto a high reflectivity sample holder and placed at the center of the integration sphere so that back scattered light waves were captured by the integration sphere. The high reflectivity wall material of the integration sphere was used to calibrate measured reflection spectra. Spectral measurements in the mid-infrared were carried out using a Fourier transform infrared spectrometer (Bruker Vertex 70v), a 2-inch mid-infrared integrating sphere (Labsphere Model 4P-GPS-020-SL, with diffuse gold coatings), and a Mercury Cadmium Telluride detector.

2.4.2 Time of flight measurement

The photon lifetime of ultra-short pulses passing through a scattering optical medium (e.g., cocoon fibers) was characterized using the time-of-flight measurement technique [11], [12]. Two ultra-short pulsed laser beams, the probe beam and the reference or gate beam, were used. A schematic of the experimental setup is illustrated in Fig. 2.4. A 50× long-working-distance objective was used to focus the probe beam (λ = 600 nm) onto a specimen. An imaging arm was added to ensure proper alignment between the input beam and the specimen. The light that passed through the specimen was collected using a parabolic reflector. The collected signal and the reference beam (λ = 800 nm) were focused and spatially and temporally super-positioned onto a Beta Barium Borate (BBO) crystal. The generated sum-frequency signal (λ = 342.86 nm) passed through a narrow bandpass filter and was collected with a photomultiplier tube (PMT). By varying the

delay between the two beams, the temporal profile of the probe beam after its interaction with the specimen can be reconstructed. Instrument response function (IRF) of the experimental setup was similarly obtained, where the probe beam did not interact with any specimen.

The probe beam and the reference beam have very similar gaussian shaped temporal profiles, and therefore the cross-correlation of the two pulses should also be represented by a gaussian function. A gaussian function was first used to fit the temporal profile of the cross-correlation between the reference and the probe beam. The fitted function was then convolved with an exponential decaying function with a time constant τ to fit measured temporal profiles of TE and TM polarized pulses after exiting the specimen. The best fit yields photon lifetime τ, which characterizes the strength of light scattering inside the specimen.

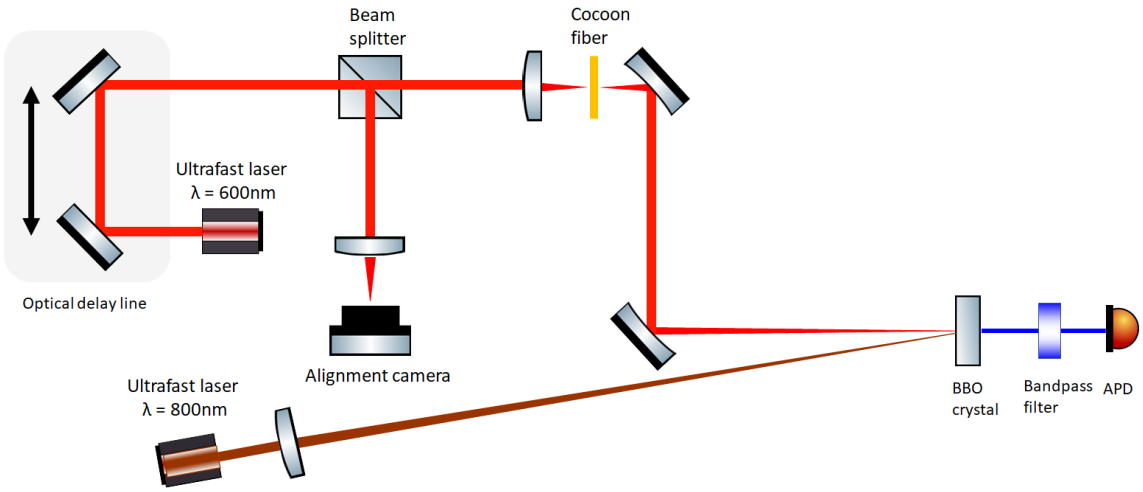

Figure 2.4 Schematic diagram of the time-of-flight measurement technique.

2.2.3 Fiber characterization

A supercontinuum laser (SuperK extreme EXU-6) coupled to a filter-based monochromator (λ= 400 -1050 nm, LLTF Contrast) was used as the light source. Light was focused onto the entrance facet of one cocoon fiber with a 50× long-working-distance objective (Mitutoyo 50× M Plan APO). An imaging arm branched out with a removable 50/50 beam splitter was used to align the incident beam with the entrance facet of the fiber. A matching objective, coupled to an imaging camera, was used to image the intensity distribution on the exit facet of the fiber. A variable neutral density filter was used to maintain the peak intensity at below 80% of the saturation level of the camera for all the images collected. The cocoon fibers and the exit facet imaging arm of the setup were mounted on separate XYZ linear translation stages to allow independent alignment and focusing adjustments with respect to the incoming beam.

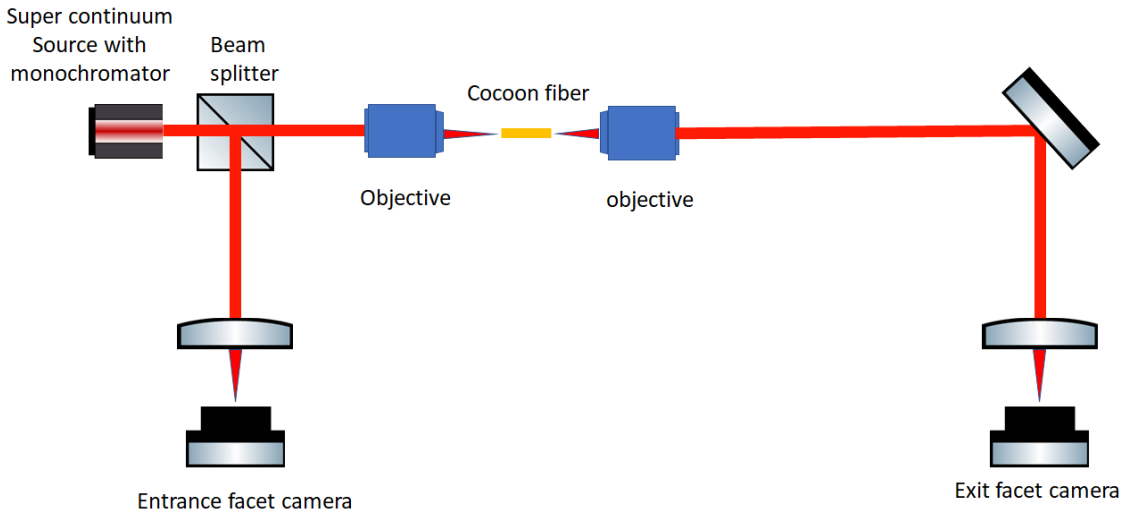

Figure 2.5 Schematic diagram of the optical setup used to characterize light transport in cocoon fibers supporting transverse Anderson localization.

2.5 Thermodynamic measurement

2.5.1 Ant hair removal

The hairs of the ants were removed by gently rubbing a blunt tungsten needle along the skin of the ants. The hairs break easily from their sockets and electrostatically attach to the needle. There is no loss of cuticular material from the ant specimens and all material loss (<1%) is due to the removal of the hairs.

2.5.2 Thermodynamic measurement setup

In the thermodynamic measurements, all radiative heat transfer effects, which the silver ants experience in their natural foraging environment, were mimicked. A high-power Xenon lamp (Thorlabs HPLS-30-04) was used to simulate solar radiation, creating a spatially uniform power distribution at the ant specimens' surface (~1000 W m^{-2}). The radiation spectrum of the lamp matches well with the solar spectrum. A large thermoelectrically cooled metal plate (TE Technology CP-200), maintained at 5°C and coated with a high-emissivity paint, was used to simulate background radiation of a clear sky. The specimens (head or gaster of silver ants) were suspended in still air on a specimen holder made of two pairs of thin human hairs to minimize thermal conduction. Fig. 2.6 shows how an ant head is placed on the hairs and the experimental setup.

Thermodynamic measurements were also conducted in vacuum. In this case, thermal convection was minimized and the dominant channel of heat dissipation was thermal radiation. The specimen was suspended on two thin metal wires and placed inside a vacuum chamber (Janis ST-100), where the pressure is maintained at below 0.001 Pa.

The same high-power Xenon lamp was used and the optical power at the ant specimens' surface was ~760W m^{-2}.

The rise and fall of body temperature of the ant specimens was recorded with a thermal camera (FLIR T640) at 30 frames per second. The camera was equipped with an infrared macro lens to capture detailed images of the ant body. The lamp was turned on and off at ~40-second intervals during recording, in order to obtain a specimen's temporal temperature profile, from which the rise and decay time constants and the equilibrium temperature reached with the lamp in the on-state could be determined.

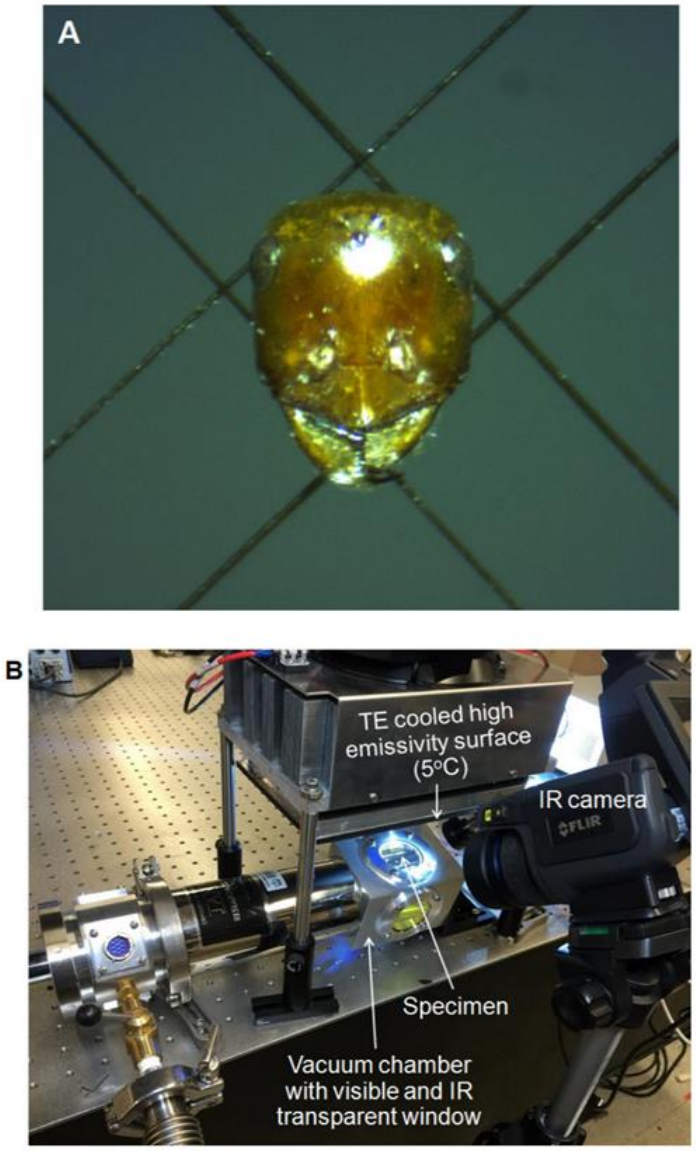

Figure 2.6 Photos of specimen and experimental setup. (A) Photo of an ant head with hairs removed placed on two pairs of thin hairs. (B) Photo of the thermodynamic measurement setup.

2.6 Simulation techniques

2.6.1 FDTD

Finite-difference time-domain (FDTD) method was used throughout our studies to simulate the optical properties of structured biological and biomimetic materials as a function of wavelength and angle of incidence. In a typical FDTD simulation, we created the structural details of the subjects in computer models, assigned realistic complex refractive indices (e.g., those chitin and silk protein complex) to the structures, and conducted full-wave simulations to study how light waves interact with these structures.

2.7 References

[1] H. L. Leertouwer, B. D. Wilts, and D. G. Stavenga, "Refractive index and dispersion of butterfly chitin and bird keratin measured by polarizing interference microscopy," *Opt. Express*, vol. 19, no. 24, p. 24061, Nov. 2011.

[2] D. E. Azofeifa, H. J. Arguedas, and W. E. Vargas, "Optical properties of chitin and chitosan biopolymers with application to structural color analysis," *Opt. Mater. (Amst).*, vol. 35, no. 2, pp. 175–183, Dec. 2012.

[3] J. Kumirska, M. Czerwicka, Z. Kaczyński, A. Bychowska, K. Brzozowski, J. Thöming, and P. Stepnowski, "Application of Spectroscopic Methods for Structural Analysis of Chitin and Chitosan," *Mar. Drugs*, vol. 8, no. 5, pp. 1567–1636, Apr. 2010.

[4] J. Brugnerotto, J. Lizardi, F. . Goycoolea, W. Argüelles-Monal, J. Desbrières, and M. Rinaudo, “An infrared investigation in relation with chitin and chitosan characterization,” *Polymer (Guildf).*, vol. 42, no. 8, pp. 3569–3580, Apr. 2001.

[5] B. E. A. Saleh and M. C. Teich, *Fundamentals of Photonics*. New York, USA: John Wiley & Sons, Inc., 1991.

[6] N. Huby, V. Vie, A. Renault, S. Beaufils, T. Lefevre, F. Paquet-Mercier, M. Pezolet, and B. Beche, “Native spider silk as a biological optical fiber OP - Applied Physics Letters, 2013, Vol.102(12),” *Appl. Phys. Lett.*, vol. 102, no. 12, 2017.

[7] Y. Reddy, Narendra; Jiang, Qiuran; Yang, “Biocompatible Natural Silk Fibers from Argema mittrei,” *J. biobased Mater. bioenergy*, vol. 6, pp. 558–563, 2012.

[8] G. Zhou, Z. Shao, D. P. Knight, J. Yan, and X. Chen, “Silk fibers extruded artificially from aqueous solutions of regenerated bombyx mori silk fibroin are tougher than their natural counterparts,” *Adv. Mater.*, vol. 21, no. 3, pp. 366–370, 2009.

[9] Sponk, “Primary structure of fibroin,” *wikipedia*. .

[10] J. Fischer, “General introduction to Nanoscribe,” 2012.

[11] M. Burresi, L. Cortese, L. Pattelli, M. Kolle, P. Vukusic, D. S. Wiersma, U. Steiner, and S. Vignolini, “Bright-white beetle scales optimise multiple scattering of light,” *Sci. Rep.*, vol. 4, pp. 1–8, 2014.

[12] B. D. Wilts, X. Sheng, M. Holler, A. Diaz, M. Guizar-Sicairos, J. Raabe, R.

Hoppe, S. H. Liu, R. Langford, O. D. Onelli, D. Chen, S. Torquato, U. Steiner, C. G. Schroer, S. Vignolini, and A. Sepe, “Evolutionary-Optimized Photonic Network Structure in White Beetle Wing Scales,” *Adv. Mater.*, vol. 1702057, pp. 1–6, 2017.

Chapter 3

Enhanced solar reflection and radiative heat dissipation in Saharan silver ants

3.1 Background

The silver ants of the Sahara Desert, *Cataglyphis bombycina*, inhabit one of the hottest terrestrial environments on earth. There they occupy the unique ecological niche of a "thermophilic scavenger" [1]. In wide-ranging foraging journeys, during which they move at maximum speeds of 0.7 $m \cdot s^{-1}$ across the hot sand surface, they search for corpses of insects and other arthropods that have succumbed to the thermally harsh desert conditions, which they themselves are able to withstand more successfully. On hot summer days, they may reach maximal foraging activities when temperatures of the desert surface are as high as 60° to 70°C [2]. In order to survive under these conditions of peak foraging activity, every now and then they must unload excess heat by pausing on top of stones or sticks of dry vegetation, where due to the steep temperature gradient above the sand surface they encounter considerably lower temperatures. Under the midday sun of a summer day the ants may spend up to 70 % of their entire foraging time in resorting to this kind of thermal respite (cooling-off) behavior. In keeping their body temperature below their critical thermal maximum of 53.6 °C [3], they do not only need mechanisms to reduce heat absorption from the environment, but they must also be able

to efficiently dissipate excess heat, so that they can minimize the amount of time spent in thermal refuges and hence lost in search for prey.

Here we demonstrate by a series of optical and thermodynamic measurements, full-wave simulations and heat-transfer modeling how a dense array of uniquely shaped hairs characteristic for *Cataglyphis bombycina* enables the ants to maintain lower body temperatures by (i) reflecting a large portion of the solar radiation in the visible and near-infrared range of the spectrum, and (ii) radiating heat to the surrounding environment by enhancing the emissivity in the mid-infrared, where the blackbody radiation spectrum of the ant's body culminates. The thermoregulatory solutions that the silver ants have evolved to cope with thermally stressful conditions show that these animals are able to control electromagnetic waves over an extremely broad range of the electromagnetic spectrum (from the visible to the MIR) and that different physical mechanisms are employed in different spectral ranges to realize an important biological function.

3.2 Characterization

Specimens of *Cataglyphis bombycina* collected in Tunisia (34°10'N, 08°18'E) were used for all the morphology, optical, and thermodynamic measurements.

3.2.1 Morphology Characterization

In these ants, those parts of the body that strike by a brilliant silvery glare (Fig. 3.1A) are covered by dense and uniform arrays of hairs (Fig. 3.1B). This hair cover occupies the dorsal and lateral sides of the body leaving the ventral surface exposed (Fig. 3.2). As SEM images show, the hairs, which gradually taper off at the tip, are locally aligned in

the same direction (Fig. 3.1C). Their most remarkable structural feature is their triangular cross-section characterized by two corrugated top facets and a flat bottom facet facing the ant's body (Figs. 3.1D, E). Cross sectional views obtained by focused ion beam (FIB) milling and scanning electron microscopy (SEM) techniques show that at any given cross-section the dimensions of the hairs vary greatly due to the tapering of the hairs, and that the gap between the bottom hair facet and the cuticular surface also varies but is generally larger than a few hundred nanometers.

The cross-sectional image (Fig. 3.1D) was obtained with a focused ion beam/scanning electron microscopy dual system (FEI Helios NanoLab DualBeam). The detailed description of the milling process is described in Section 2.2.1.

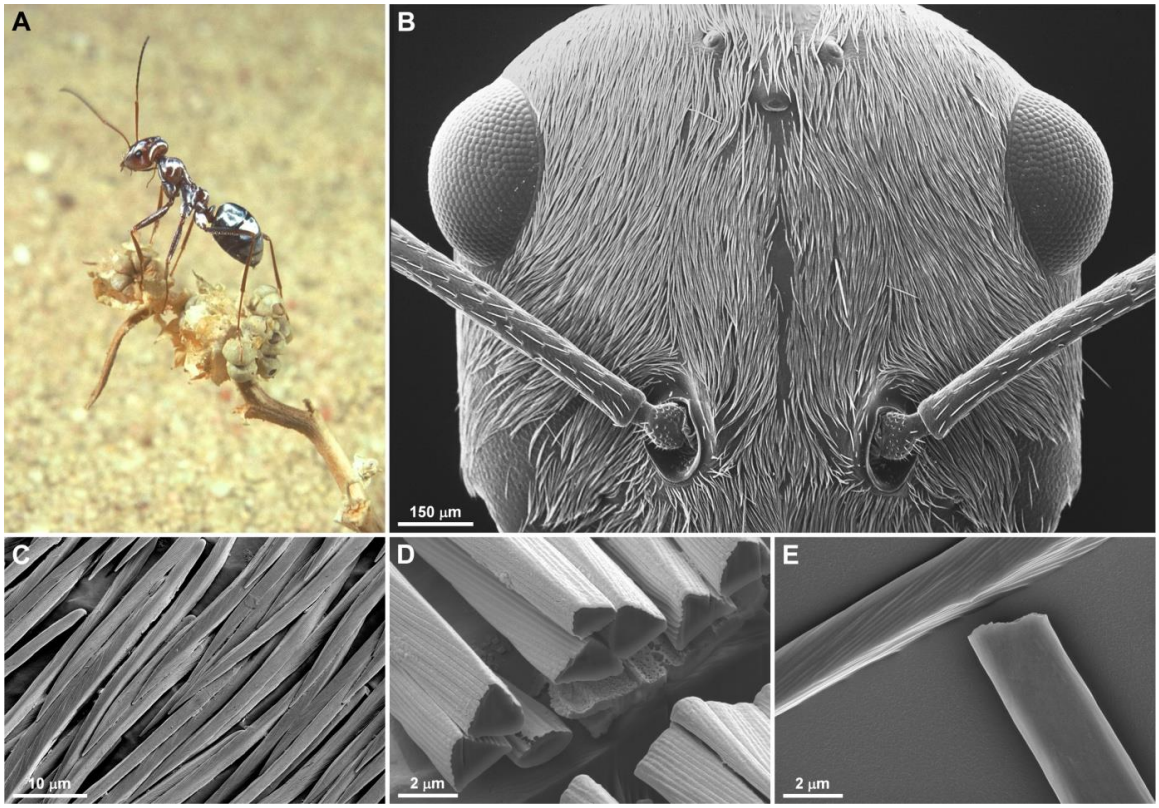

Figure 3.1 The bright glare of the silver ant and its structural basis. (A) Silver ant offloading heat on top of dry vegetation [4]. (B) SEM frontal view of the head densely covered by hairs, which spare only the two compound eyes and the three ocelli. (C) SEM image of the hairs gradually tapering off towards the tip. (D) Cross-sectional view of the hairs milled with FIB and imaged with SEM. (E) SEM image of two hairs with one flipped upside down to exhibit the flat bottom facet.

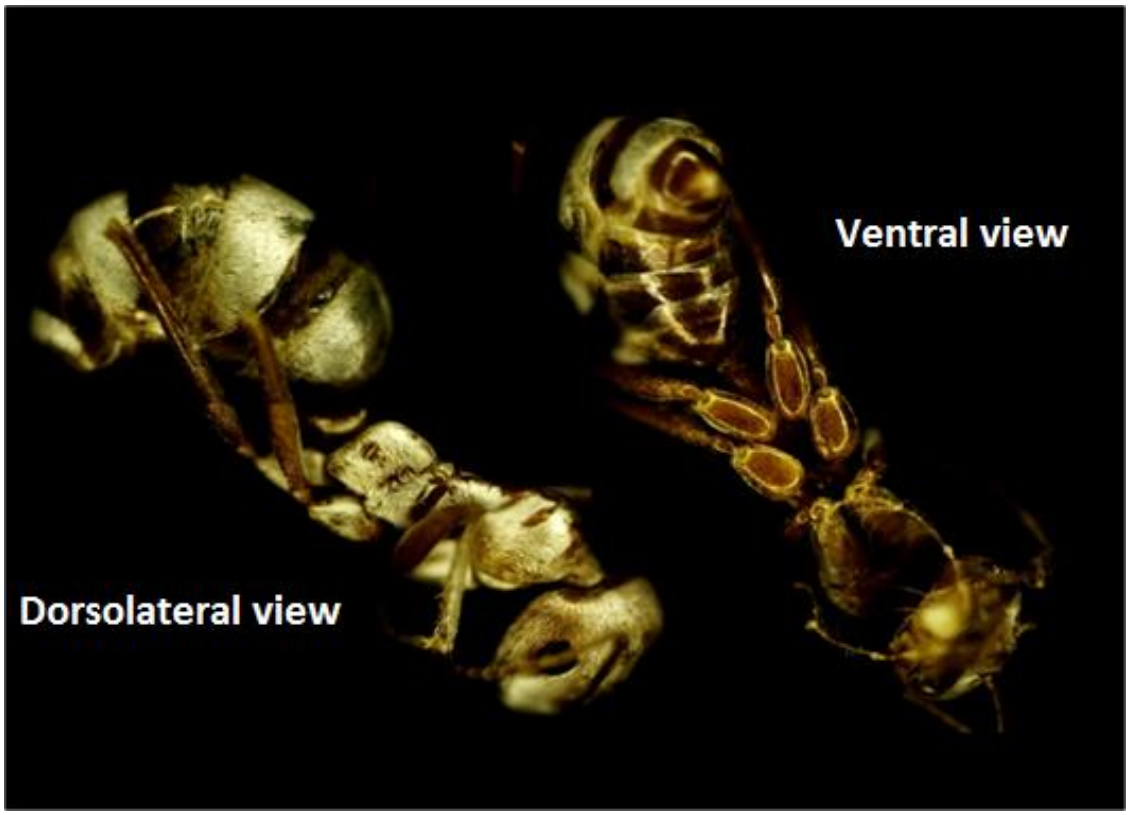

Figure 3.2 Dorsolateral and ventral view of a silver ant as seen in the dark field mode of the optical microscope. The figure shows that the hairs cover only the dorsolateral sides of the ant's body, leaving the ventral side freely exposed to the desert floor.

3.2.2 Optical characterization and simulation in the visible and near-infrared

Optical reflectivity measurements of ant specimens were obtained with two Fourier transform spectrometers, one collecting spectra in the visible and NIR (λ = 0.45 - 1.7μm) and the other in the MIR (λ = 2.5 - 16μm) range of the spectrum. The visible and NIR measurements showed that hemispherical reflection, i.e., the sum of specular and diffuse reflection collected through an integrating sphere is substantially enhanced in regions with intact hair coverage as compared to regions from which the hairs had been removed

(Fig. 3.3A and Fig. 3.2). The hairs help the ants to reflect 67% of the incoming solar radiation rather than only 41% as is the case after their removal. This enhancement is due to scattering within the triangular hairs (Mie scattering), where light gets trapped and then reradiates out in all directions. Individual hairs of given cross-sectional dimensions generate enhanced reflection due to scattering at specific wavelengths where fundamental and higher-order Mie resonance modes are supported [5]–[8]. Due to the variation in cross sectional areas, resonance peaks from individual hairs are averaged out over the visible and NIR spectrum, so that the hair cover effectively acts as a broadband reflection enhancement coating.

This enhancement in reflectivity can be demonstrated with a simple FDTD simulation (Fig. 3.4). Both the height and the width of the triangular hair are set to 2 μm. The gap between the bottom facet of the triangular hair and the surface of the cuticle is set to 600 nm. Simulated reflectivity spectrum for a periodic array of triangular hairs with TE polarized incident light is shown in Fig. 3.4A. Peaks in the spectra are the result of Mie resonances in the triangular hair, where back scattering is substantially enhanced as a result of these dielectric resonance modes. Vertical dashed lines show a few positions on the spectrum where enhanced reflectivity occurs due to Mie resonances. The corresponding distributions of light intensity at these wavelengths are plotted in Fig. 3.4B. Cross-sectional view of the two-dimensional distribution of light intensity ($|\text{Electric field}|^2$) for five exemplary Mie resonances are displayed. The reflectivity peak at λ = 2.880 μm is the fundamental TE resonance mode. The peaks at shorter wavelengths represent higher-order Mie resonances in the triangular hair.

We also measured the reflectivity spectra using transverse-electric (TE), transverse-magnetic (TM), and non-polarized light produced by a laser stabilized Xenon lamp (see method section). The TE (TM) polarization is defined as the situation in which the electric field component of the incident light is parallel (perpendicular) to the orientation of the hair array. Polarized light was created by inserting a broadband wire-grid polarizer into the beam path, at a location before light was focused onto the specimens. Spectra for non-polarized incident radiation were obtained by removing the polarizer. As shown in Fig. 3.3D, the hair array acts as a birefringent layer where higher reflectivity was observed for TE polarized light when compared to TM polarized light. This extra enhancement for TE polarized light is due to stronger Mie resonance mode confinement from the triangular hairs. At the three facets of the triangular hair structure, external reflection for TE polarized light is higher than TM polarized light. This enhanced reflection at the hair/air interface then leads to stronger resonance mode confinement/higher quality factor, which leads to higher overall reflectivity. When the hairs have been removed, there is no difference in the spectra obtained with TE, TM and unpolarized light. The high reflectivity in the near-infrared is partially due to the internal microstructures of the cuticle itself, which will be discussed in section 3.5.

While parts of the dorsal side of the ant face solar radiation at right angles, due to the ellipsoidal shape of the ant's body a large portion of the dorsolateral surface is hit by solar radiation obliquely [3]. This prompted us to examine the reflectivity as a function of the incidence angle of radiation, which was varied from 0° to 80°, with 0° representing the direction normal to the surface. The hairs were aligned parallel with the rotation axis of the radiating beam. As the results show, Mie scattering enhances reflectivity over all

angles when regions with intact hair cover are compared to those with hairs removed (Fig. 3.3C). With increasing angle of incidence, this enhancement becomes particularly strong at beyond 30°. This is the critical angle at which total internal reflection starts to occur at the bottom facets of the hairs (Fig. 3.3B-II). At angles approaching 90°, reflectivity drops off when total internal reflection at one of the top facets starts to direct more of the radiation towards the ant's body (Fig. 3.3B-III).

Next, we performed finite-difference time-domain (FDTD) simulations, in order to demonstrate the functional significance of the triangular cross-section of the hairs in enhancing reflectivity in the visible and NIR range. These simulations compared the reflective properties of triangular and circular hairs of the same cross-sectional area. Even though the enhancement of reflectivity at normal incidence is comparable in both cases, triangular hairs produce an extra enhancement at higher angles of incidence (Fig. 3.3C). The reason is that although Mie scattering of similar strength occurs in both circular and triangular hairs, in the latter the total internal reflection at the bottom of the hairs enhances reflectivity substantially further.

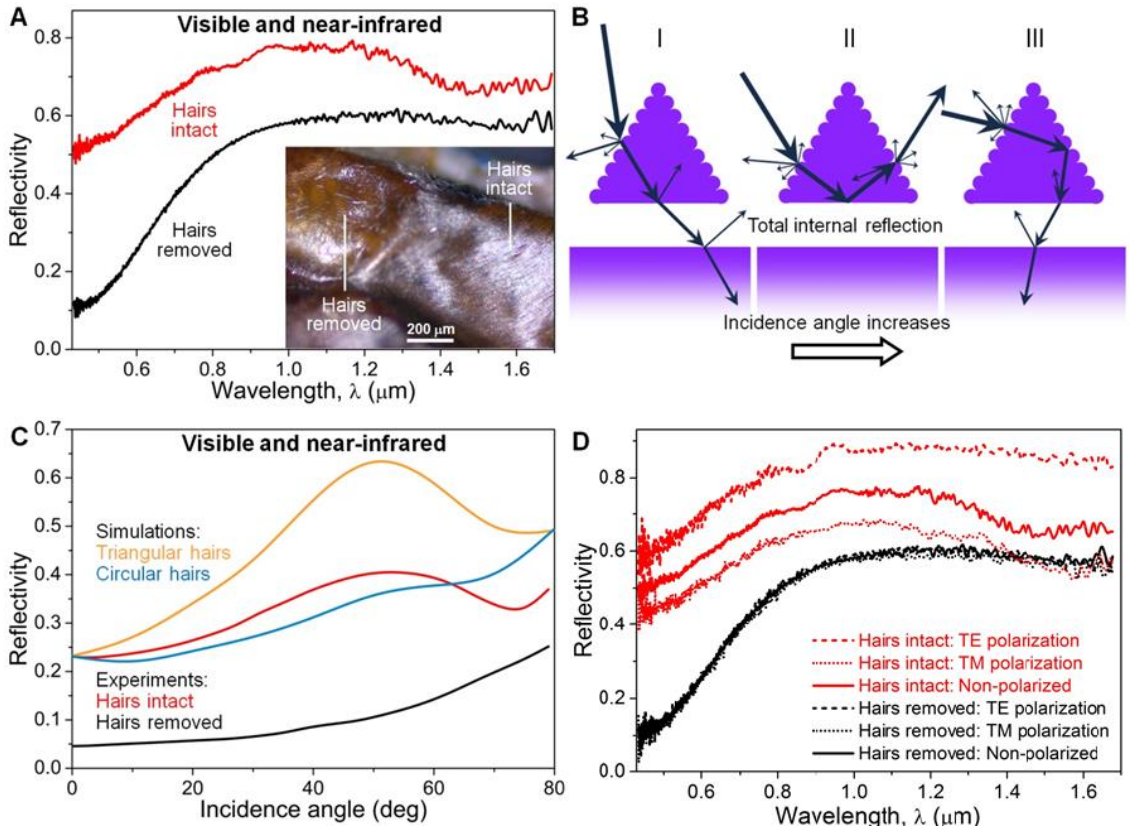

Figure 3.3 Reflectivity of the silver ant's body surface from the visible to the mid-infrared range of the spectrum. (**A**) Hemispherical reflectivity measured in the visible and near-infrared. (**B**) Schematic diagram showing the interaction between light and a hair at small (I), intermediate (II), and large (III) incidence angles. The corrugated upper two facets enhance diffuse reflection in the ultraviolet and visible range. (**C**) Measurement and simulation results showing reflectivity as a function of incidence angle. (**D**) Polarization dependent reflectivity measured in the visible and near-infrared.

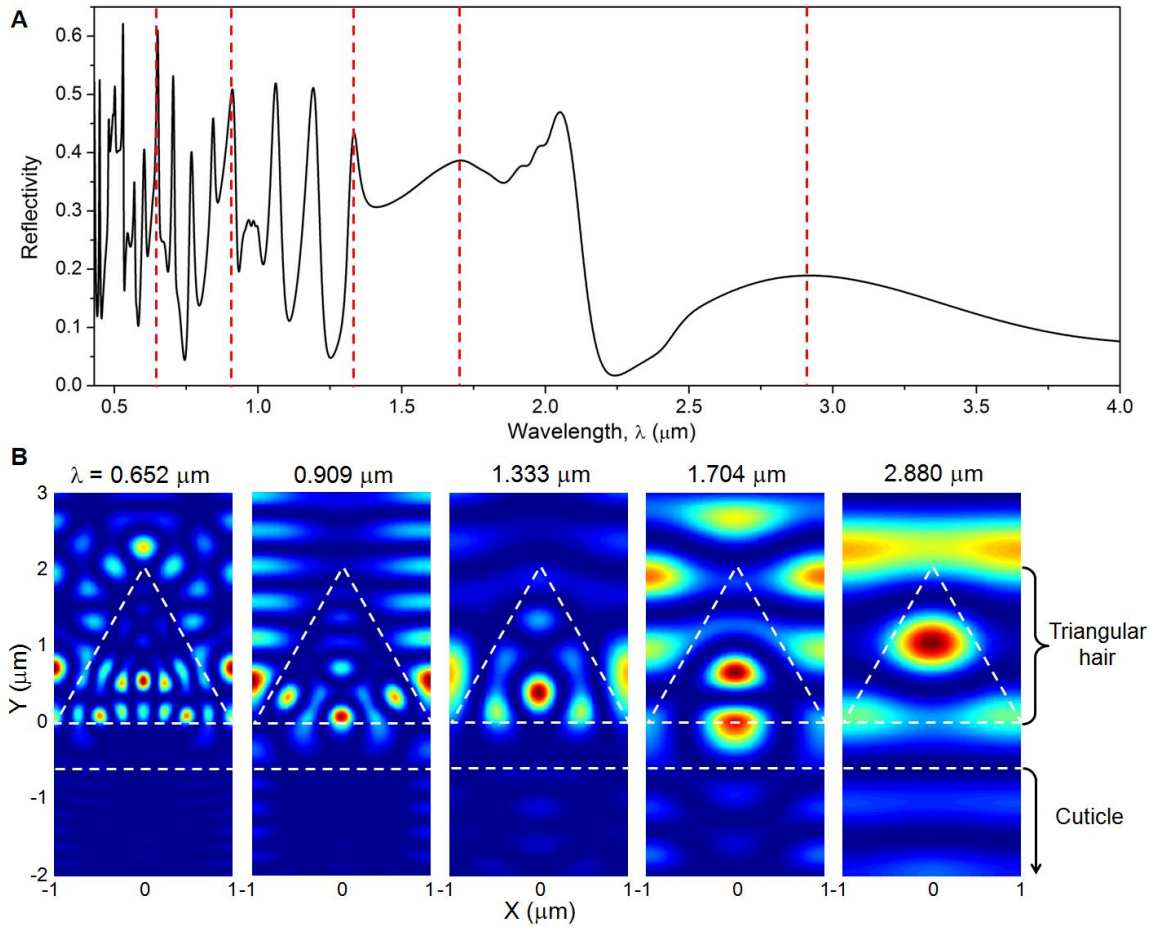

Figure 3.4 (**A**) Reflectivity spectrum for a periodic array of triangular hairs with TE polarized incident light. (**B**) Cross-sectional view of two-dimensional distribution of light intensity (|Electric field|^2) for five exemplary Mie resonances.

3.2.3 Gap between hair and cuticle and wetting and drying experiment

The specimens were put through a series of wetting and drying cycles to demonstrate how the reflectivity was affected by having an index matching fluid, which filled all the gaps between the hairs and the cuticle. A solution of 70% ethanol and 30% water was used as the emersion fluid, and the reflectivity was characterized through a series of optical images taken with the dark field mode of an optical microscope (Zeiss Axio Imager). The wetting and drying cycle experiment (Fig. 3.5A-E) shows that the enhancement in reflectivity is greatly suppressed when the hairs are completely immersed in the ethanol-water solution, which destroys both Mie scattering within the hairs and total internal reflection at the bottom facets of the hairs. As the solution evaporated, individual hairs started to light up, until all the hairs became bright, when the solution had completely evaporated.

As shown in this experiment, the high reflectivity disappeared when the specimens were wetted by an ethanol-water solution, which removed the refractive index contrast between air and hairs, and thus destroyed the conditions required for Mie scattering and total internal reflection. Through simulation (Fig 3.5F), we also show that the reflectivity in the visible and near-infrared increases as the gap opens up. Physically, the near-field coupling between triangular hairs and the substrate (the cuticle) reduces the strength of Mie resonance. This near-field coupling effect becomes weaker as the gap size increases. Reflectivity is very small when the hairs are in contact with the cuticular surface. The simulated averaged reflectivity spectra under TE and TM polarized incident light are plotted.

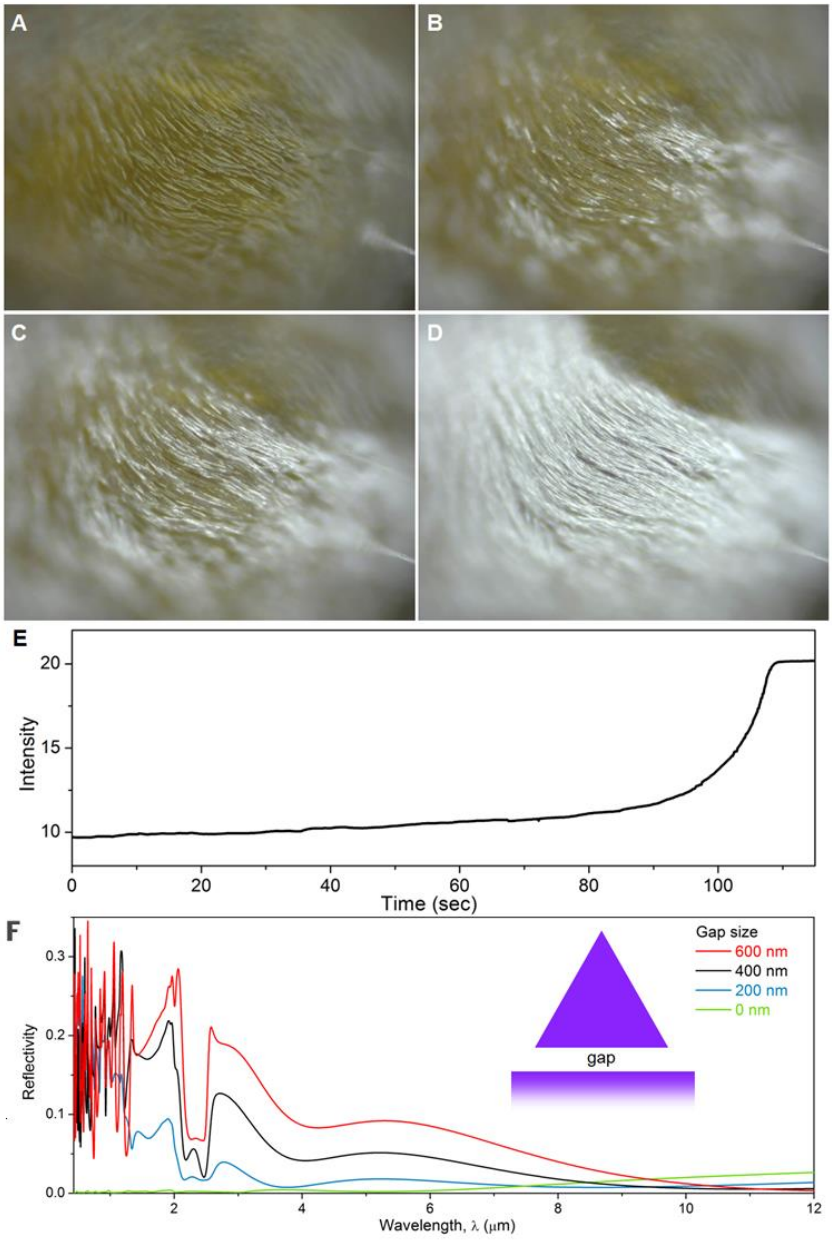

Figure 3.5 Optical images taken during the drying cycle of the wetting and drying experiment, the four frames are captured at (**A**) 10, (**B**) 100, (**C**) 105 and (**D**) 112 seconds after the drying process started. (**E**) Intensity of reflected visible light as a function of time during the drying process. (**F**) FDTD simulation of reflectivity as a function of gap length between hair and cuticle

3.2.4 Optical characterization and simulation in the mid-infrared

Reflectivity measurements performed in the MIR range revealed a second important point in the silver ant thermotolerance story. When proceeding from lower to higher wavelengths, at about 8 μm a remarkable transition occurs in the reflectivity curves obtained from hairy and hair-free regions: the enhanced reflectivity of regions with hair cover as compared to those without hairs reverses to reduced reflectivity (Fig. 3.6A). As Kirchhoff's law of thermal radiation states, reduced reflectivity corresponds to enhanced emissivity . At a body temperature of 50°C, which the silver ants may reach when foraging at peak activity times, the blackbody radiation of the ant's surface would lie in the range of 6 - 16 μm (peaked at ~9 μm) and thus allow the silver ants to offload heat more efficiently through radiative heat transfer. The latter reduces the respite time and further decreases the equilibrium body temperature.

This concept is further explored through FDTD simulation. Where we simulated the reflectivity as a function of wavelength at normal incidence for 30 different random arrangements of the hair structure (Fig 3.7). The refence is for an infinitely thick chitin-protein complex layer with refractive index n = 1.56, resembling that of chitin. The spectra show a significant enhancement of reflectivity in the visible and near-infrared and a decrease of reflectivity (or increase of emissivity) in the mid-infrared. The layered structure and the coupling of modes between neighboring hairs lead to a broadening of the Mie resonance modes. Simulated reflectivity from TE polarized light is higher when compared to TM polarized light. This simulated birefringent effect from the hair array agrees with the measured results (Fig. 3.3D). The MIR reflectivity as a function of incidence angle was also explored through simulation (Fig. 3.6B). Simulation results

show that MIR reflectivity is significantly lower for Hairy region when compared to the bald region over all incident angles simulated (0 - 80˚).

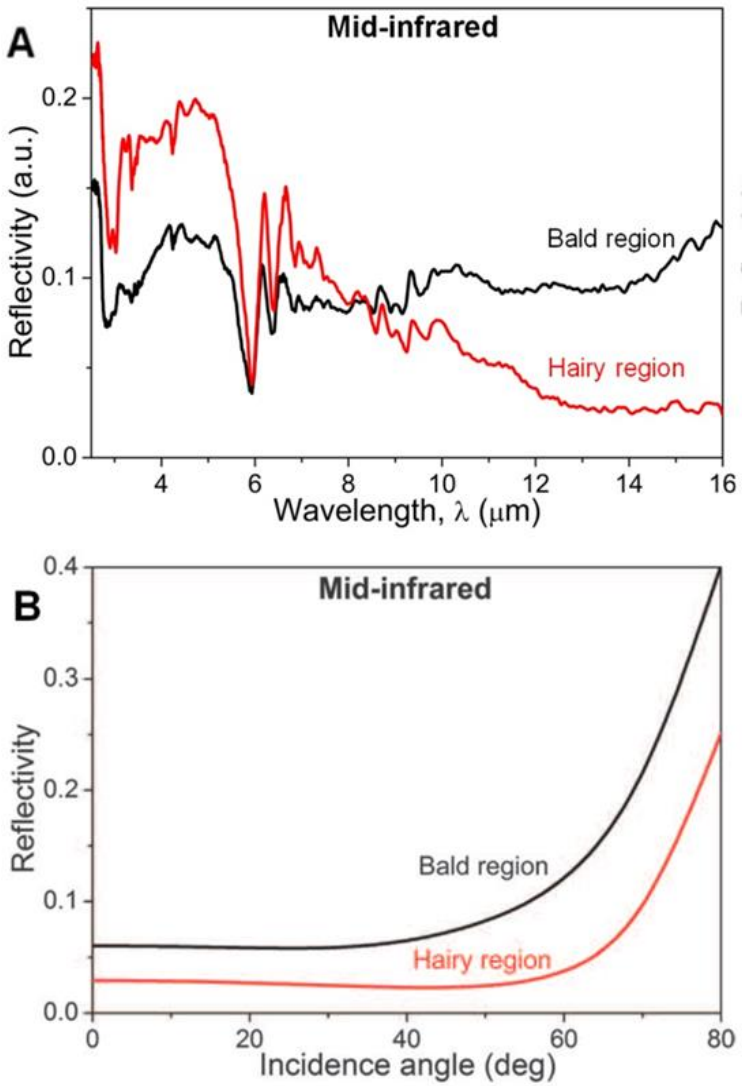

Figure 3.6 (**A**) Integrated hemispherical reflectivity measured in the Mid-infrared for region with hair intact and region with hair removed. (**B**) Simulated reflectivity in the mid-infrared as a function of incidence angle.

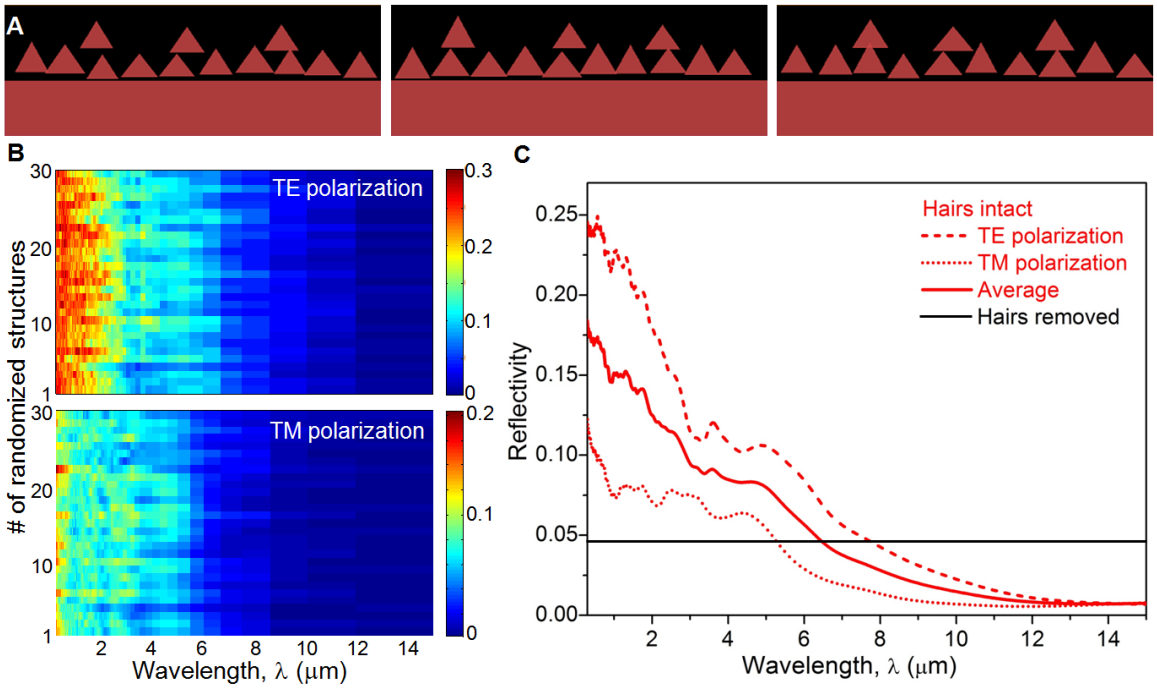

Figure 3.7 (**A**) Three exemplary arrangements of the triangular hairs. (**B**) Simulated reflectivity as a function of wavelength at normal incidence for 30 different random arrangements of the hair structure. (**C**) Reflectivity spectra averaged over 30 simulations.

3.2.5 Thermodynamic measurement

How does the hair cover with its enhanced reflectivity in the visible and NIR and its enhanced emissivity in the MIR affect the radiative heat transfer between the ant's body and the environment? To investigate this question, we performed thermodynamic experiments, which mimicked all radiative heat transfer effects in the silver ants' natural foraging environment. To accomplish this task, we used a high-power xenon lamp to simulate the solar spectral distribution at the desert sand surface [9] and a thermoelectrically cooled high-emissivity metal plate to simulate the clear sky with its

low level of blackbody radiation [10]. The ant specimens were suspended on thin threads to minimize thermal conduction. Thermodynamic experiments were conducted in vacuum to study thermal radiation, as well as in still air to study the interplay of thermal radiation and convection. Under both conditions, the specimens with their natural hair covers were able to maintain significantly lower steady-state body temperatures than the same specimens with the hairs removed (Fig. 3.8).

Thermodynamic experiments were conducted using the gaster and head parts of silver ants. Temporal temperature profiles were taken before and after hair removal in vacuum and in still air. The experiments conducted in vacuum allowed us to exclude conductive and convective thermal transfer effects, so that we can study the sole effect of radiative heat transfer and extract the mid-infrared emissivity before and after hair removal. The experiments conducted in still air allowed us to study the comparative contributions of radiative cooling and natural convection and extract convective heat transfer coefficient *h* with and without hair cover. According to the heat transfer model developed in section 1.1.5, we have

$$\begin{aligned} \tau_{vac,hair} &= \frac{m_{hair}c}{4\bar{\varepsilon}_{hair}\sigma s'\bar{T}_{vac,hair}^{\ 3}}, \quad \tau_{vac,bald} = \frac{m_{bald}c}{4\varepsilon_{bald}\sigma s'\bar{T}_{vac,bald}^{\ 3}} \\ \tau_{air,hair} &= \frac{m_{hair}c}{4\bar{\varepsilon}_{hair}\sigma s'\bar{T}_{air,hair}^{\ 3} + h_{hair}s'}, \quad \tau_{air,bald} = \frac{m_{bald}c}{4\varepsilon_{bald}\sigma s'\bar{T}_{air,bald}^{\ 3} + h_{bald}s'} \end{aligned} \tag{3.1}$$

These four equations allow us to solve for mid-infrared emissivity, $\bar{\varepsilon}_{hair}$ and ε_{bald}, and convective heat transfer coefficients, h_{hair} and h_{bald}, before and after hair removal. The results for the gaster and head sections of silver ants are summarized in table 3.1.

Table 3.1 Thermodynamic measurement result summary for gaster and head

Specimens	**Gaster**		**Head**	
Conditions	Before hair removal	After hair removal	Before hair removal	After hair removal
Mass	0.4774mg	0.4729mg	m_{hair}=0.4836mg	m_{bald} =0.4801mg
Surface area	s' =26.37 mm^2		s' =20.86 mm^2	
Time constant of temperature change in vacuum	$\tau_{vac,hair}$ = 4.627 sec	$\tau_{vac,bald}$ = 4.937 sec	$\tau_{vac,hair}$ = 5.947 sec	$\tau_{vac,bald}$ = 6.126 sec
Time constant of temperature change in air	$\tau_{air,hair}$ = 1.445 sec	$\tau_{air,bald}$ = 1.408 sec	$\tau_{air,hair}$ = 1.713 sec	$\tau_{air,bald}$ = 1.688 sec
Average temperature during thermodynamic experiment in vacuum	$\bar{T}_{vac,hair}$ = $(T_{max}+T_{min})/2$= (50.28°C +30.27°C) = 40.28°C	$\bar{T}_{vac,bald}$ = $(T_{max}+T_{min})/2$= (56.16°C +30.43°C) = 43.30°C	$\bar{T}_{vac,hair}$ = 41.66°C $(T_{max}+T_{min})/2$= (51.42°C +30.43°C) = 41.66°C	$\bar{T}_{vac,bald}$ = 45.36°C $(T_{max}+T_{min})/2$= (60.56°C +32.16°C) = 45.36°C
Average temperature during thermodynamic experiment in air	$\bar{T}_{air,hair}$ = $(T_{max}+T_{min})/2$= (43.50°C +29.74°C) = 36.62°C	$\bar{T}_{air,bald}$ = $(T_{max}+T_{min})/2$= (46.61°C +29.98°C) = 38.30°C	$\bar{T}_{air,hair}$ = 37.54°C $(T_{max}+T_{min})/2$= (44.29°C +30.78°C) = 37.54°C	$\bar{T}_{air,bald}$ = 39.47°C $(T_{max}+T_{min})/2$= (47.45°C +31.49°C) = 39.47°C
Average mid-infrared emissivity	$\bar{\varepsilon}_{hair}$ = 0.89	ε_{bald} = 0.80	$\bar{\varepsilon}_{hair}$ = 0.86	ε_{bald} = 0.80
Convective heat transfer coefficient	h_{hair} = 13.8 $W/m^2/K$	h_{bald} = 14.7 $W/m^2/K$	h_{hair} = 15.3 $W/m^2/K$	h_{bald} = 15.7 $W/m^2/K$

Summary of thermodynamic measurement result parameters for the Gaster and Head of the Saharan silver ants measured in vacuum

The mid-infrared emissivity extracted in the above table is the effective emissivity averaged over the entire surface of the specimen, including both hair-covered regions and naturally bald regions. The average emissivity of the gaster decreases from $\bar{\varepsilon}_{hair}$ = 0.89 to ε_{bald} = 0.80 with hair removed. Considering that the hairs cover approximately 75% of the gaster (dorsal and lateral regions), we have $\bar{\varepsilon}_{hair} = 75\%\varepsilon_{hair} + 25\%\varepsilon_{bald}$. Therefore, we derive that the emissivity of the hair-covered region is ε_{hair} = 0.92, and that the hair cover enhances the mid-infrared emissivity by (0.92-0.8)/0.8=15%.

Similarly, the average emissivity of the silver ant head decreases from $\bar{\varepsilon}_{hair}$ = 0.86 to $\bar{\varepsilon}_{bald}$ = 0.80 with hair removal. Considering that the hairs cover only about 50% of the head (dorsal side), we have $\bar{\varepsilon}_{hair} = 50\%\varepsilon_{hair} + 50\%\varepsilon_{bald}$. Therefore, we derive that the emissivity of the hair-covered region to be ε_{hair} = 0.92, which agrees perfectly with the value obtained from the gaster.

The extracted convective heat transfer coefficient, *h*, increases slightly with hair removal, from h_{hair} = 13.8 W/m^2/K to h_{bald} = 14.7 W/m^2/K for the gaster, and from h_{hair} = 15.3 W/m^2/K to h_{bald} = 15.7 W/m^2/K for the head. The slightly smaller heat transfer coefficient of natural convection with hair cover is because the stagnant air between the hair cover and the cuticle creates a resistance to convective heat transfer from inside the ant body.

The extracted convective heat transfer coefficient, *h*, agrees reasonably well with the value *h* = 12.7 W/m^2/K calculated using the following equations [11], [12]:

$$
\begin{aligned}
&Nu_D = 0.474 Ra_D^{1/4} = \frac{hD}{k} \\
&Ra_D = Gr_D Pr \\
&Pr = 0.711 \\
&Gr_D = \frac{g\beta \Delta T D^3}{\nu^2}
\end{aligned}
\tag{3.2}
$$

where Nu_D, Ra_D, and Gr_D are, respectively, the averaged Nusselt number, the Rayleigh number, and the Grashof number of characteristic length D. Pr = 0.711 is the Prandtl number of air at 40°C. g=9.81 m/s^2 is the acceleration of gravity, β=1/313 1/K is the thermal expansion coefficient of air at 40°C, ΔT=15K (temperature difference between specimen and surrounding air at thermal equilibrium), D~1.2 mm is the diameter of the specimen, v = 16.97×10^{-6} m^2/s is the kinematic viscosity of air at 40°C, and k=0.0271 W/m/K is the thermal conductivity of air at 40°C.

The thermodynamic experiments conducted in vacuum comparing specimens before and after hair removal further revealed that the hair cover decreases the time constants of temperature change (Fig. 3.8, B and E). The shortened time constants indicate an increased rate of radiative heat transfer and are a direct confirmation of the effect of the hairs in enhancing the MIR emissivity. By using the time constants and the heat transfer model, we computed that the hair cover enhances emissivity by about 15% (table 3.1). This enhanced emissivity is due to the fact that at large MIR wavelengths (i.e., at wavelengths much larger than the dimensions of the cross sections of the hairs), the hair structure acts as a gradient refractive index layer (Fig 1.4) [13]–[15], which provides the surface with broadband, broad-angle antireflective properties in the MIR (Fig. 3.6-3.7). Because of the influence of convection, the time constants of temperature change

decreased by a factor of about 3 when the specimens were brought from vacuum into air (Fig. 3.8). This indicates that radiative heat dissipation amounted to about one-half of convection and, therefore, still played a significant role in the presence of natural convection.

Applying experimentally extracted parameters to the heat transfer model revealed that the enhanced visible and NIR reflectivity and enhanced MIR emissivity make comparable contributions to reducing the steady-state temperature in the presence of natural convection. On hot summer days in the Sahara, the foraging activities of silver ants often occur under low wind or even still air conditions, when the ants must rely on enhanced visible and NIR reflectivity and enhanced MIR emissivity equally heavily to reduce their body temperature during the respite behavior.

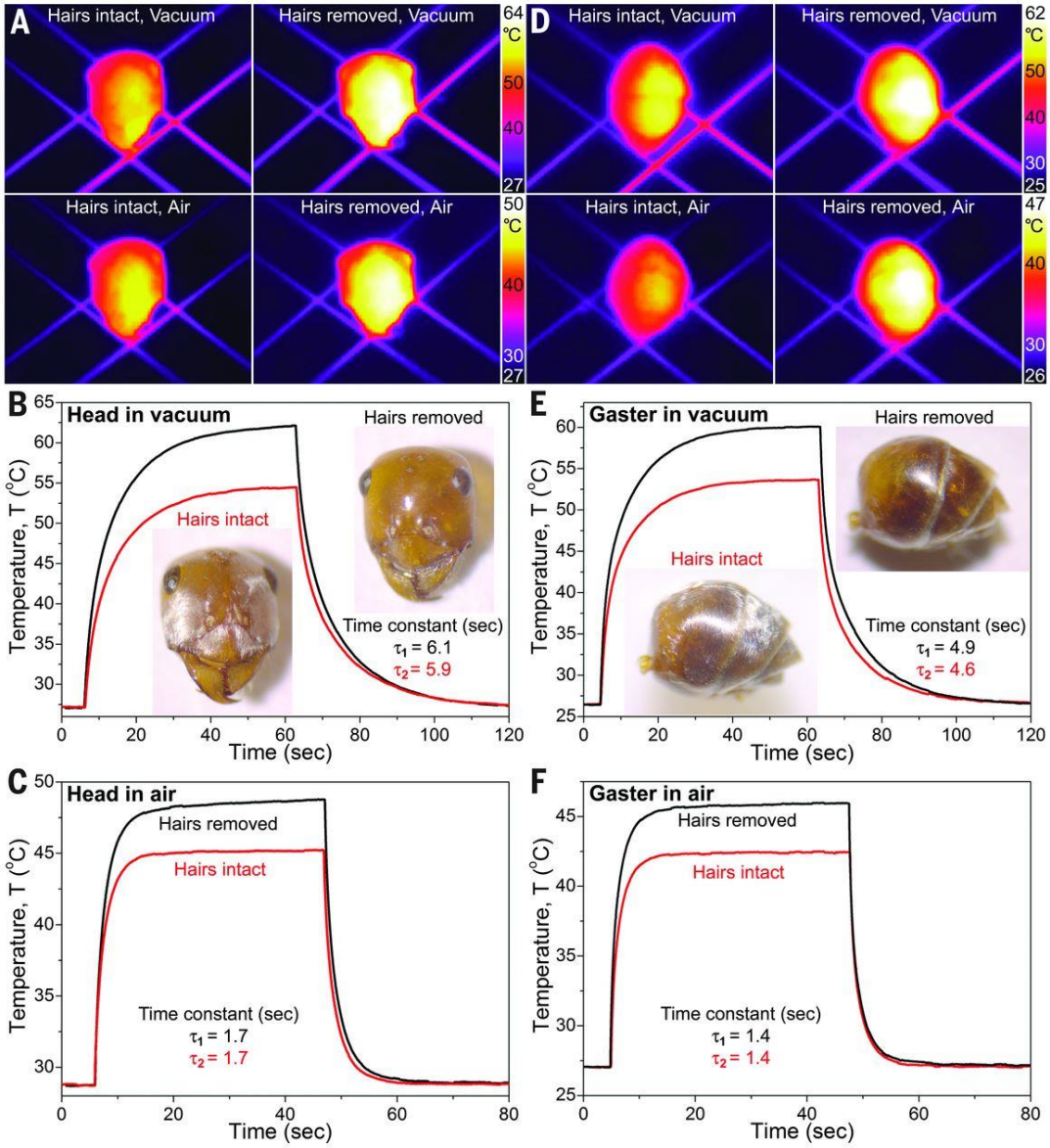

Figure 3.8 (**A**) Thermal camera images showing the head of an ant specimen at the thermal steady state under different conditions. Temporal temperature profile measured for the head before and after hair removal in vacuum (**B**) and in still air (**C**) are shown. (**D** to **F**) Results obtained for the hind part (gaster) of an ant specimen. Insets in (B) and € are photos of specimens before and after hair removal.

3.3 Thermodynamic model of silver ants

Using parameters extracted from experiments, we can numerically solve equation (1.16) to obtain equilibrium temperature, and study the comparative contributions of enhanced visible and near-infrared reflectivity and enhanced MIR emissivity in reducing the equilibrium temperature under different convective heat transfer conditions.

Figure 3.9 shows the equilibrium temperature as a function of visible and near-infrared reflectivity $R_{vis\text{-}NIR}$ and MIR emissivity ε_{MIR} under natural convection. $R_{vis\text{-}NIR}$ ranges from 0.44 to 0.69 (or absorptivity $\alpha_{vis\text{-}NIR}$ ranges from 0.31 (with hairs) to 0.56 (hairs removed)), and ε_{MIR} from 0.8 to 0.89. The way we calculated the variation ranges of $R_{vis\text{-}NIR}$ and ε_{MIR} is described in the subsequent section. Removing hairs from specimens decreases $R_{vis\text{-}NIR}$ from 0.69 to 0.44 and ε_{MIR} from 0.89 to 0.80. As a result, the equilibrium temperature increases from ~34^{o}C to ~39.2^{o}C (i.e., from the upper right corner to the lower left corner in Fig. 3.9. The effects of $R_{vis\text{-}NIR}$ and ε_{MIR} are quite comparable, as the temperature gradient in Fig. 3.9 is essentially diagonal. If $R_{vis\text{-}NIR}$ and ε_{MIR} were able to change independently: (a) when ε_{MIR} increases from 0.8 to 0.89 for a fixed $R_{vis\text{-}NIR}$, equilibrium temperature decreases by ~2^{o}C, (b) when $R_{vis\text{-}NIR}$ increases from 0.44 to 0.69 for a fixed ε_{MIR}, equilibrium temperature decreases by ~3^{o}C.

The way we calculated the variation range of $R_{vis\text{-}NIR}$ and ε_{MIR} according to experimental results are discussed in the following.

Assuming that the body parts (head or gaster) of silver ants can be approximated as a sphere with radius r, and that θ and φ are angles of the spherical coordinate system. The total absorbed power $\boldsymbol{\alpha' Ps}$ is calculated in the following way. The power incident onto a

small area $dA=r^2\sin\theta d\theta\varphi$ on the sphere is $PdA\cos\theta$. Therefore the total power incident onto the upper half of the sphere is:

$$\int_{\varphi=0}^{2\pi}\int_{\theta=0}^{\pi/2}\left(P\cos\theta\right)r^2\sin\theta d\theta d\varphi = P\pi r^2 \tag{3.3}$$

The total reflected power from the upper half of the sphere is:

$$\int_{\varphi=0}^{2\pi}\int_{\theta=0}^{\pi/2}\left[R\left(\theta\right)P\cos\theta\right]r^2\sin\theta d\theta d\varphi \tag{3.4}$$

where $R(\theta)$ is angular dependent reflectivity. Thus, the total absorbed power is the difference between (3.3) and (3.4):

$$\alpha' Ps = \pi r^2 P - \int_{\varphi=0}^{2\pi}\int_{\theta=0}^{\pi/2}\left[R\left(\theta\right)P\cos\theta\right]r^2\sin\theta d\theta d\varphi = \left[1-\frac{1}{\pi}\int_{\varphi=0}^{2\pi}\int_{\theta=0}^{\pi/2}R\left(\theta\right)\sin\theta\cos\theta d\theta d\varphi\right]P\left(\pi r^2\right) \tag{3.5}$$

Therefore, the absorptivity in the visible and near-infrared is:

$$\alpha' = 1-\frac{1}{\pi}\int_{\varphi=0}^{2\pi}\int_{\theta=0}^{\pi/2}R\left(\theta\right)\sin\theta\cos\theta d\theta d\varphi \tag{3.6}$$

The angular dependent reflectivity $R(\theta)$ is calculated in the following way. The reflectivity measured from various spots on the ant body at zero-degree angle of incidence and normalized to solar irradiance according to equation (1) is $R_{hair}(\theta=0)$ = 60%±15% for hair-covered regions and $R_{bald}(\theta=0)$ = 40%±10% for regions with hairs removed. Using the measured increase in reflectivity as a function of incidence angle, $\Delta R_{hair}(\theta)$ and $\Delta R_{bald}(\theta)$ (Fig. 2C), we can then calculate the angular dependent reflectivity:

$$\begin{aligned} R_{hair}(\theta) &= R_{hair}(\theta=0) + \Delta R_{hair}(\theta) \\ R_{bald}(\theta) &= R_{bald}(\theta=0) + \Delta R_{bald}(\theta) \end{aligned}. \tag{3.7}$$

Using equations (18) and (19), the values of absorptivity α' for the hair-covered regions and regions with hairs removed are, respectively,

$$\begin{aligned} \alpha'_{hair} &= 1 - \frac{1}{\pi}\int_{\varphi=0}^{2\pi}\int_{\theta=0}^{\pi/2} R_{hair}(\theta)\sin\theta\cos\theta d\theta d\varphi = 0.31 \\ \alpha'_{bald} &= 1 - \frac{1}{\pi}\int_{\varphi=0}^{2\pi}\int_{\theta=0}^{\pi/2} R_{bald}(\theta)\sin\theta\cos\theta d\theta d\varphi = 0.56 \end{aligned} \tag{3.8}$$

The mid-infrared emissivity ε is calculated using the following equation (*8*),

$$\varepsilon = \frac{\int_{\varphi=0}^{2\pi} d\varphi \int_{\theta=0}^{\pi/2} [1 - R(\theta)]\sin\theta\cos\theta d\theta}{\int_{\varphi=0}^{2\pi} d\varphi \int_{\theta=0}^{\pi/2} \sin\theta\cos\theta d\theta} \tag{3.9}$$

Here *R(θ)*, shown in Fig. 2F,is the mid-infrared reflectivity obtained from full-wave FDTD simulations. It was averaged over TE and TM polarizations, and averaged over azimuthal angle from φ=0 to φ=90^o in step of 10^o. *R(θ)* is also weighted by the blackbody radiation spectrum at 50^{o}C using an equation similar to equation (*1*). We obtained using (21) that the emissivity for the bald and hairy regions, respectively, is ε_{bald} = 0.87 and ε_{hair} = 0.93. ε_{hair} = 0.93 agrees well with the value extracted from the thermodynamic experiments (where we obtained ε_{hair} = 0.92). ε_{bald} = 0.87 seems to be an overestimation: our measurements indicate that the heterogeneous internal structures of ant body enhance MIR reflection. For example, out MIR reflectivity measurements using an integration sphere, which captures all specular and diffuse reflection, showed that the MIR reflectivity at zero-degree incidence angle is 10-20%, which is much larger than 4.8%,

the reflectivity at normal incidence of an interface between air and chitin with n=1.56. Enhanced MIR reflectivity leads to reduced MIR absorption or emissivity. In solving the equilibrium temperature using the heat transfer model, we used $\varepsilon_{bald} = 0.80$ obtained from the thermodynamic experiments.

It is interesting to note that the hairs cover only the top and sides of the ant's body, where they are responsible for the effects described above. The absence of hairs on the bottom surface reduces the radiative energy transfer between the hot sand and the cooler ant body, so that the animals can reduce the absorption of blackbody radiation from the desert floor.

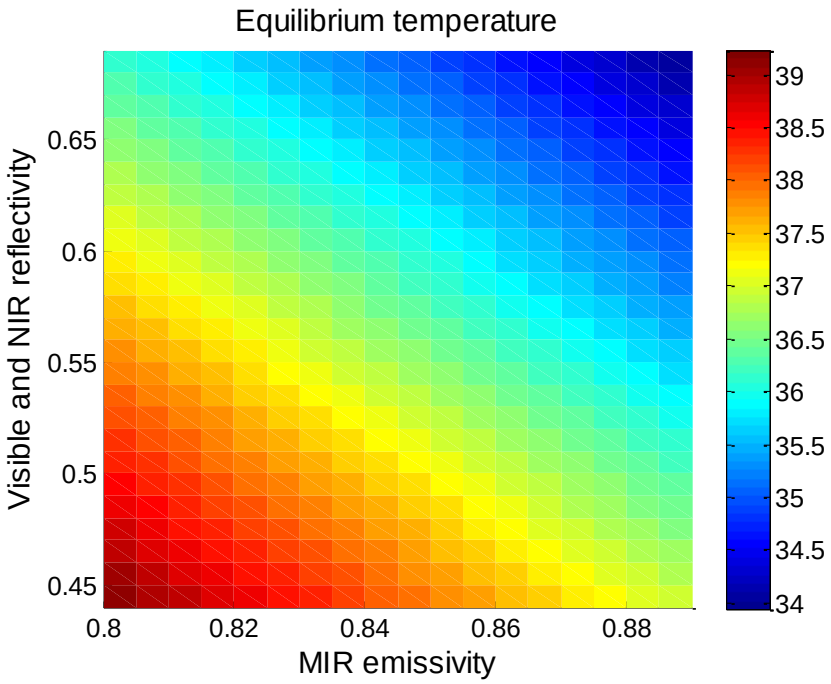

Figure 3.9 Equilibrium temperature as a function of visible and near-infrared reflectivity $R_{VIS-NIR}$ and MIR emissivity ε_{MIR} at h = 15W/m^2/K, which represents natural convection.

3.4 Biomimetic hair structures

Inspired by the hair coating of the Saharan silver ants, we utilized an existing fabrication technique to create biomimetic Metasurfaces for passive radiative cooling of objects. The device shown in figure 3.10 is fabricated using a commercially available nano-3D lithography tool based on two-photon polymerization. The technique itself and the fabrication process and the detailed parameters used are described in section 2.3.1

The photoresist used here have similar optical properties to the natural chitin material, both in refractive index and materials absorption. The photoresist does have significantly higher absorption in the ultraviolet and the blue, where the strong absorption is needed for the polymerization process to take place during writing.

A schematic diagram of the designed unit cell is shown on the right in figure 3.10. In order to have the triangular beams suspended in air to create enhanced Mie resonance within the structure, three rectangular pillars are used to support a single triangular beam, creating an air gap between the substrate and the triangular beams. There is a thin layer of photoresist deposited between the structure and the substrate to enhance adhesion. Gaps are placed in between adjacent triangular beams to allow the developer solution to gain full access to the unexposed photoresist and remove it from the rest of the structure.

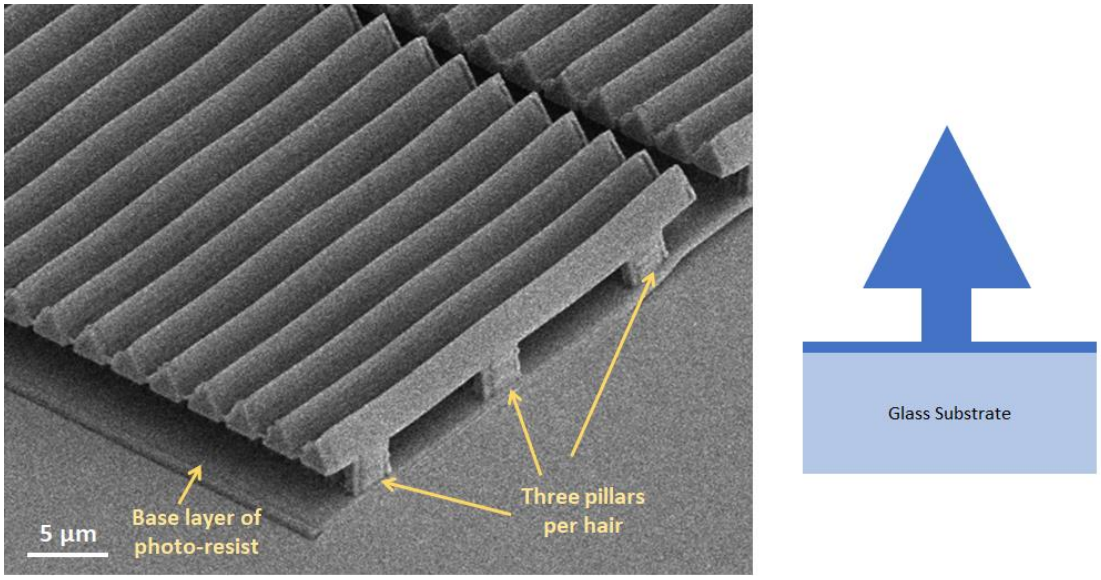

Figure 3.10 Single layer biomimetic triangular hair structure fabricated using nano-3D direct laser write lithography. The schematic diagram on the right is the cross-sectional view of a single triangular beam, where three pillars are used to support and suspend the triangle, and a base layer of photoresist is used to enhance adhesion.

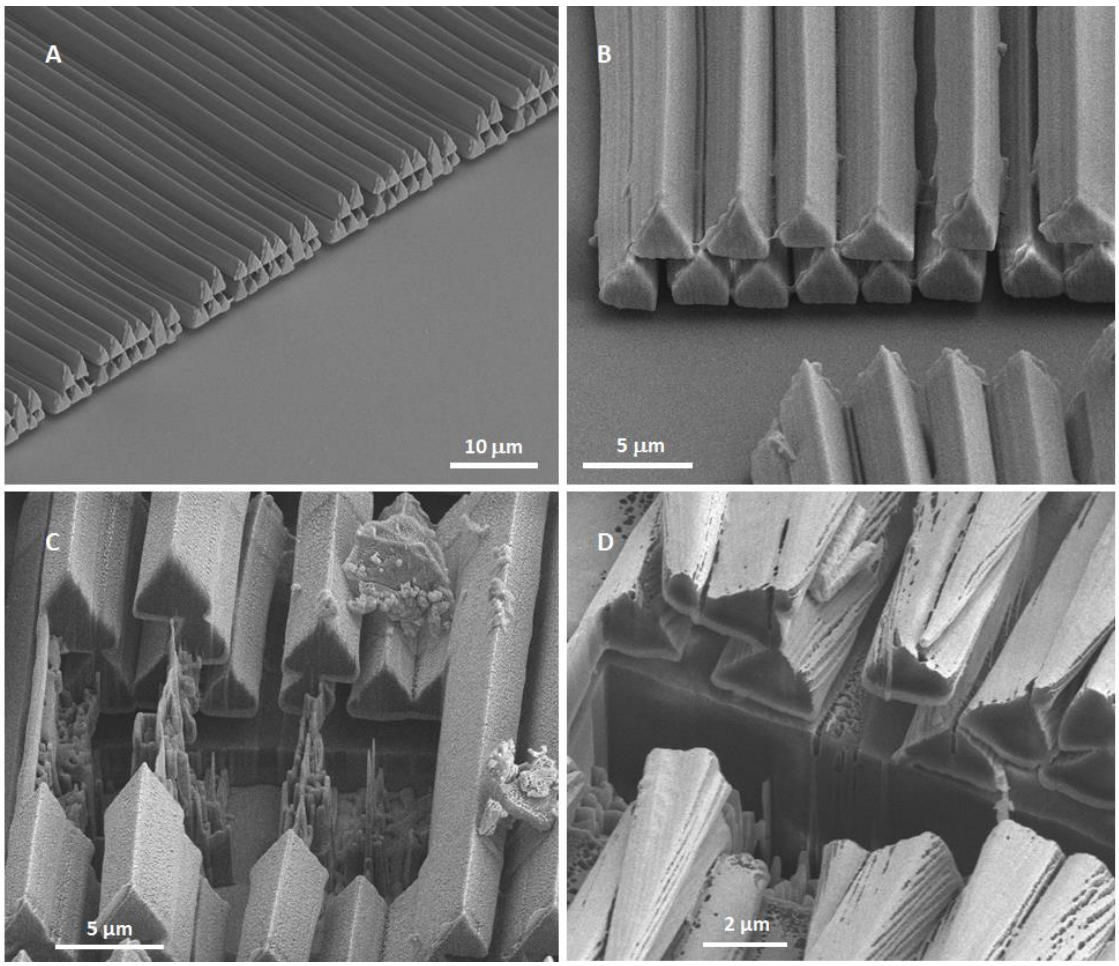

Figure 3.11 (A-B) Two different magnifications and viewing angles of a dual-layer biomimetic hair coating. (C) Cross-sectional view of a three-layer randomly stacked biomimetic hair coating. (D) Cross-sectional view of actual silver ant hair structure (for comparison).

Using this unit cell as the basis of the designed structure, we fabricated devices with two layers and three layers of hair coatings, where the hairs are randomly positioned on top of one another just as they would be in the actual silver ant hair arrangement. In Fig. 3.11 C and D, we compare side by side a manmade structure and the actual hair structure. The capability of the direct laser lithography allows us to fabricate hair structures with similar size and position when compared to natural hair coatings.

To characterize radiative cooling capabilities of the man-made devices, we measured the device's hemispherical reflectivity from the visible to the mid-infrared (red curve, Fig. 3.12), and compared it to results of a glass substrate (blue) and a control sample, consisting of a thin slab of photoresist using the same amount of material as the three-layer biomimetic hair coating (yellow).

The results show that the biomimetic hair coating enhances reflectivity in the visible and near-infrared, and it also suppresses reflectivity in the mid-infrared. The glass substrate has a pronounced phonon resonance peak centered at $\lambda \approx 9$ μm, the biomimetic coating was able to suppress that peak significantly, and the suppression is not only due to materials absorption, as is demonstrated by the controlled structure, but also due to structural suppression of reflection from the triangular beams acting as an anti-reflective coating in the mid-infrared.

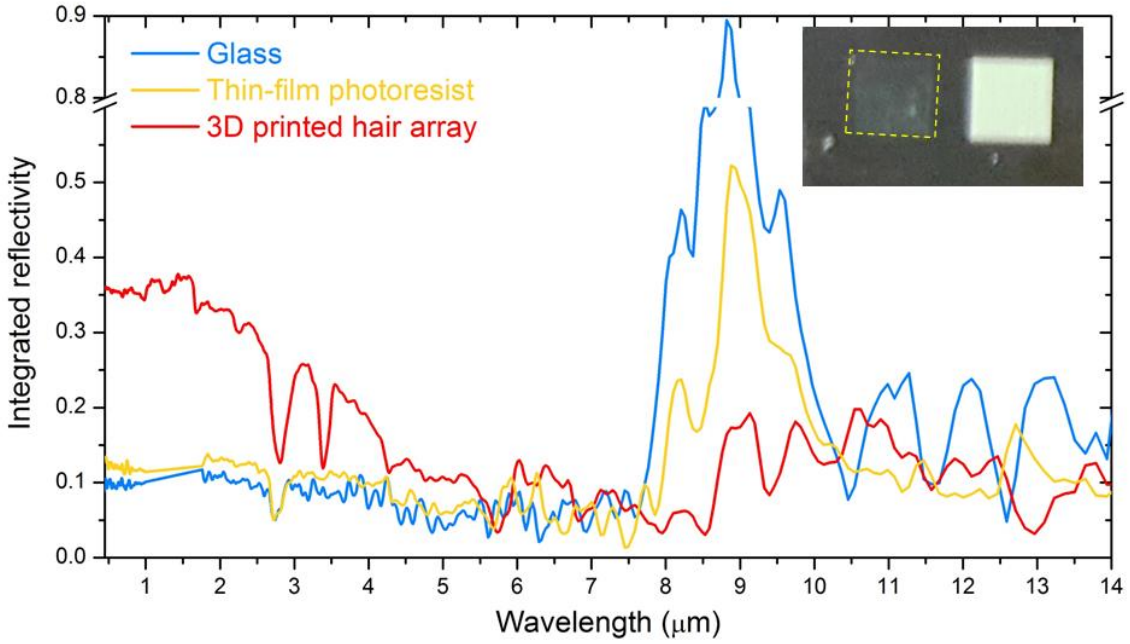

Figure 3.12 Hemispherical reflectivity measurement of a three layer (red) biomimetic hair coating, compared to measurement results of the glass substrate (blue) and a control sample, consisting of a thin slab of photoresist using the same amount of material as the three-layer biomimetic hair coating (yellow).

3.5 Enhanced reflectivity in the ultraviolet and near-infrared

3.5.1 Enhanced reflectivity in the ultraviolet due to hair corrugation

We also investigated possible optical effects of the corrugations on the top two facets of the hair structure (Fig. 3.13A), where the step sizes of the corrugations are ~200 to 300 nm. Reflectivity simulations (Fig. 3.13B) show enhanced reflectivity in the ultraviolet

and blue when comparing structure with corrugated facets to structure with smooth facets. The enhancement can be contributed to enhanced scattering at the corrugated surfaces where the size of the corrugations is optimized to reflect light in the UV and near UV portion of the solar spectrum. The enhancement could protect the ant body from harmful UV radiation, and reduce the overall solar absorption of the ant body.

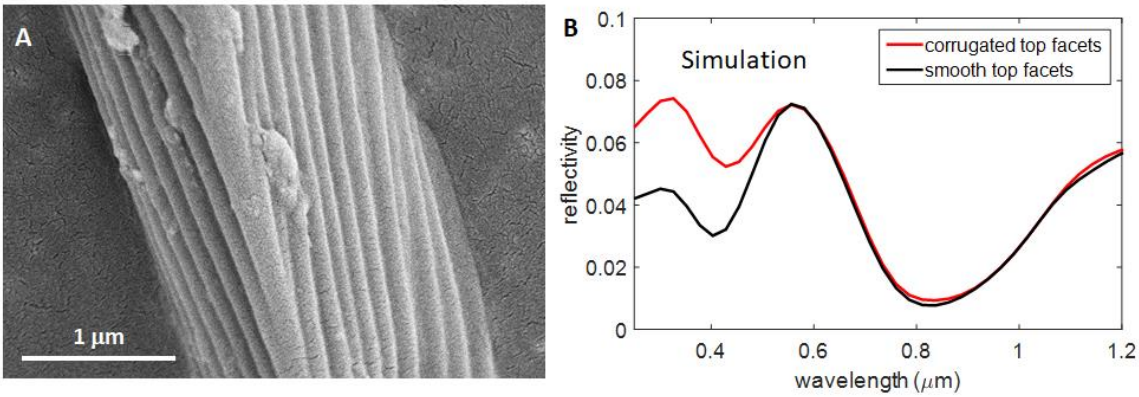

Figure 3.13 Optical effects of hair corrugation. (A) SEM image showing the top two facets of a hair of the Saharan silver ants, showing longitudinal corrugations on the surface of the hair. (B) Simulated reflectivity of a single triangular hair structure with corrugated top facets, indicating enhanced reflectivity in the ultra-violet and the blue when compared to hair structure with smooth top facets.

3.5.2 Near-infrared reflectivity enhancement in desert ants

We measured reflectivity of seven different species of desert ants, and all exhibited enhanced reflectivity in the near-infrared portion of the solar spectrum (λ=1-1.7 µm). The enhanced reflectivity is created by strongly scattering structures located right underneath

the inner cuticle wall (Fig. 3.14). In the case of *Cataglyphis bombycina*, a granular layer was embedded between a thin membrane and the inner wall of the cuticle, whereas in the case of *Cataglyphis noda*, spherical shaped particles were found to be attached to the inner wall of the cuticle. It's interesting to note that while the granular and spherical structures enhance reflectivity in the visible and near-infrared, due to strong absorption of visible light by pigmentations in the cuticular layer, the overall enhanced reflectivity was only observed in the near-infrared.

While broadband enhanced reflection over the entire solar spectrum is ideal for minimizing heating from solar radiation, specific pigmentations develop in different species of ants for various others reasons that are essential to their survival, such as camouflage. Near-infrared light accounts for half of the overall power of solar radiation. In this wavelength range, light is no longer visible to animal eyes, and these species of desert ants have found a way to utilize these unique nanostructures to enhance solar reflection without compromising visible colorations.

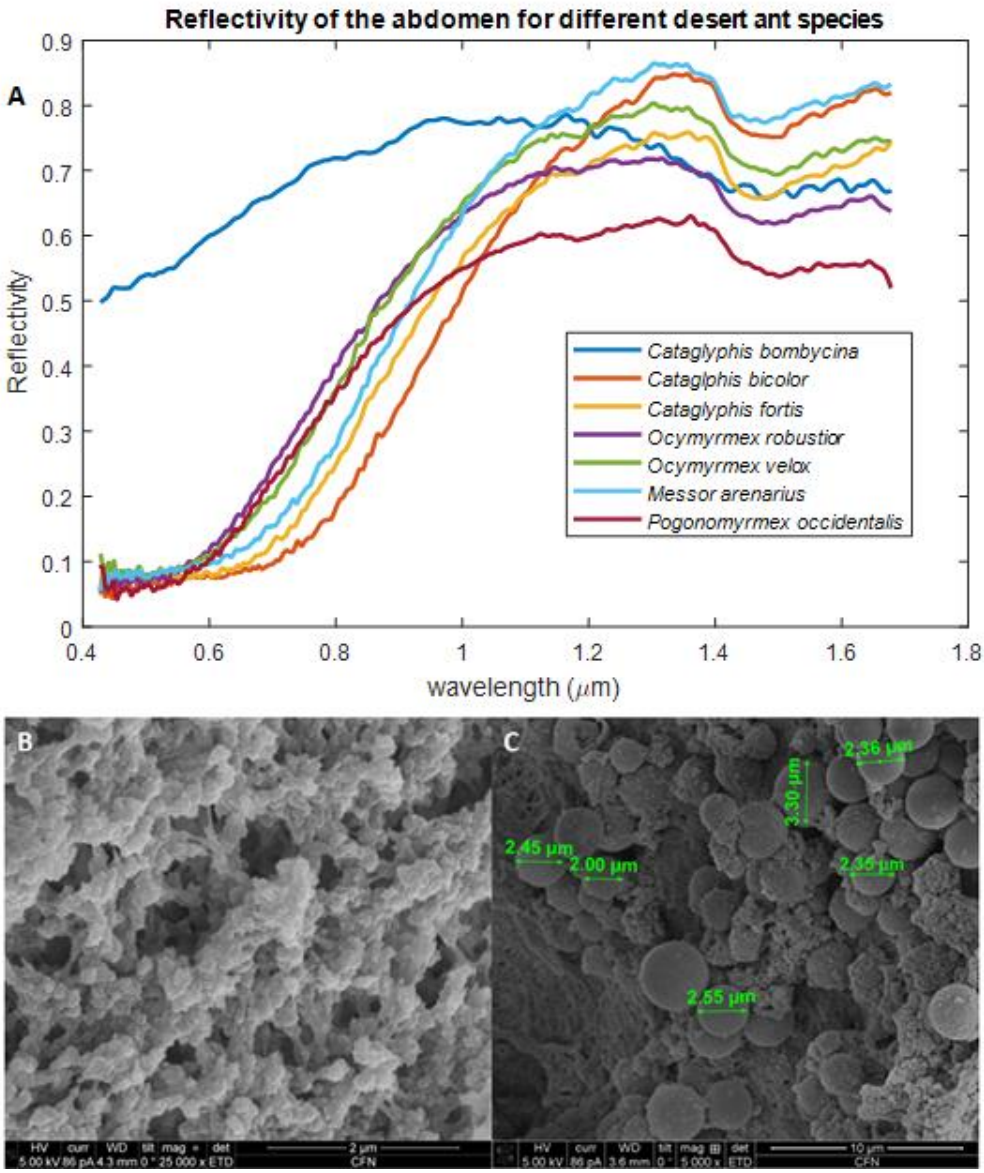

Figure 3.14 (A) Measured hemispherical reflectivity for the abdomen of seven different species of desert ants. All the species exhibit a high reflectivity in the near-infrared region of the solar spectrum. (B-C) Granular and spherical structures found on the inner cuticle wall of *Cataglyphis bombycina* and *Cataglyphis noda*, respectively. Both structures enhanced reflectivity in the visible and near-infrared.

3.5.3 Bioinspired cool roof coating

Inspired by these reflectance-enhancing micro- and nano-structured granules and spheres, we designed and fabricated a cool-roof coating material that introduces a large number of dielectric nanoparticles (SiO_2, TiO_2) into a silicone-based binding material. The particles were selected to have sizes comparable to the wavelength of visible and near-infrared light, enabling strong scattering over the entire solar spectrum. The silicone embedding medium and the particles were also selected so that their absorption bands strongly overlap with the mid-infrared atmospheric transparency window. In this way, we created a coating that also exhibits enhanced thermal emissivity. Thermal measurement of the bioinspired cool-roof coating material showed that it significantly reduced the peak temperature of the roof during the daytime, when compared to a control (asphalt) (Fig. 3.15). It's interesting to note that due to the high emissivity of the roof coating and the asphalt, during nighttime, the coating can be cooled to be significantly lower than the ambient air temperature.

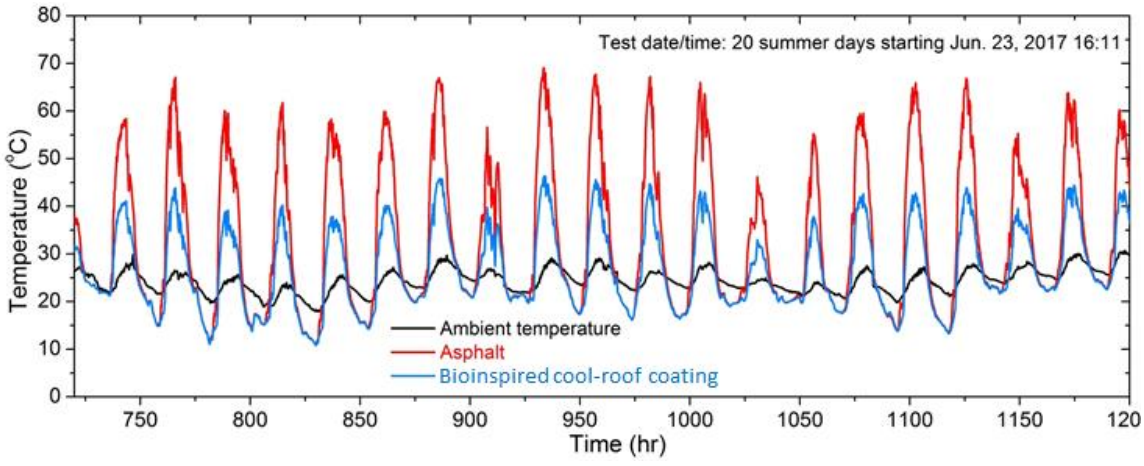

Figure 3.15 Thermal measurement of a roof covered by the bioinspired cool-roof coating compared to an asphalt roof and the ambient air temperature.

3.6 Conclusion

In conclusion, Saharan silver ants are covered with a dense array of uniquely shaped triangular hairs on the top and the sides of their bodies. These silvery hairs protect the ants against getting overheated in at least three ways. First, as a result of total internal reflection and Mie scattering the hairs enhance reflectivity in the visible and near-infrared, where solar radiation culminates. Second, in the mid-infrared, where solar radiation becomes negligible for $\lambda > 2.5$ μm, the hairs acting as an antireflection layer enhance emissivity and thus increase the ants' ability to offload excess heat via blackbody radiation. Third, the ant's bare bottom surface reflects mid-infrared radiation from the hot desert floor more efficiently than if it were covered by hairs. Taken together, these effects result in decreasing the ant's equilibrium body temperature and the time constants of heat transfer and thus enable these thermophilic scavengers to forage at exceedingly high environmental temperatures. In general, the thermoregulatory solutions, which the silver ants have evolved to cope with thermally stressful conditions, provide a first example that an animal is able to control electromagnetic waves over an extremely broad range of the spectrum (from the visible to the mid-infrared, i.e., $\lambda = 400$ nm – 16μm), and that different physical mechanisms are employed in different spectral regimes to realize important biological functions. Furthermore, the present interdisciplinary account on the silver ants could have a significant technological impact by inspiring the

development of biomimetic coatings for passive cooling of objects such as vehicles and buildings [16]–[18]. Interestingly, a recent article reported the demonstration of a multilayered film that can cool down an object by using essentially the same mechanisms as the silver ants, i.e., high reflectivity in the solar spectrum and high emissivity in the mid-infrared [19].

3.7 References

[1] R. Wehner and S. Wehner, "Parallel evolution of thermophilia: Daily and seasonal foraging patterns of heat-adapted desert ants: Cataglyphis and Ocymyrmex species," *Physiol. Entomol.*, vol. 36, no. 3, pp. 271–281, 2011.

[2] R. Wehner, A. C. Marsh, and S. Wehner, "Desert ants on a thermal tightrope," *Nature*, vol. 357, no. 6379, pp. 586–587, 1992.

[3] W. J. Gehring and R. Wehner, "Heat shock protein synthesis and thermotolerance in Cataglyphis, an ant from the Sahara desert.," *Proc. Natl. Acad. Sci.*, vol. 92, no. 7, pp. 2994–2998, 1995.

[4] R. Wehner, "Visuelle Orientierung bei Wüstenameisen," *Jahrb. Akad. Wiss. Lit. Mainz*, pp. 107–112, 1986.

[5] C. F. Bohren and D. R. Huffman, Eds., *Absorption and Scattering of Light by Small Particles*. Weinheim, Germany: Wiley-VCH Verlag GmbH, 1998.

[6] J. A. Schuller, T. Taubner, and M. L. Brongersma, "Optical antenna thermal

emitters," *Nat. Photonics*, vol. 3, no. 11, pp. 658–661, 2009.

[7] D. Lin, P. Fan, E. Hasman, and M. L. Brongersma, "Dielectric gradient metasurface optical elements," *Science (80-.).*, vol. 345, no. 6194, pp. 298–302, Jul. 2014.

[8] A. I. Kuznetsov, A. E. Miroshnichenko, M. L. Brongersma, Y. S. Kivshar, and B. Luk'yanchuk, "Optically resonant dielectric nanostructures," *Science (80-.).*, vol. 354, no. 6314, p. aag2472, Nov. 2016.

[9] K. L. Coulson, "Terrestrial Radiation: Methods of Measurement," in *Solar and Terrestrial Radiation*, Elsevier, 1975, pp. 279–307.

[10] J. L. Monteith and W. E. Reifsnyder, "Principles of Environmental Physics," *Phys. Today*, vol. 27, no. 3, pp. 51–52, Mar. 1974.

[11] *Free-Convective Heat Transfer*. Berlin/Heidelberg: Springer-Verlag, 2005.

[12] H. J. Merk and J. A. Prins, "Thermal convection in laminary boundary layers. I," *Appl. Sci. Res.*, vol. 4, no. 1, pp. 11–24, Jan. 1953.

[13] C.-H. Sun, P. Jiang, and B. Jiang, "Broadband moth-eye antireflection coatings on silicon," *Appl. Phys. Lett.*, vol. 92, no. 6, p. 61112, Feb. 2008.

[14] J.-Q. Xi, M. F. Schubert, J. K. Kim, E. F. Schubert, M. Chen, S.-Y. Lin, W. Liu, and J. A. Smart, "Optical thin-film materials with low refractive index for broadband elimination of Fresnel reflection," *Nat. Photonics*, vol. 1, no. 3, pp. 176–179, Mar. 2007.

[15] M. J. Minot, “Single-layer, gradient refractive index antireflection films effective from 035 to 25 μ,” *J. Opt. Soc. Am.*, vol. 66, no. 6, p. 515, Jun. 1976.

[16] C. G. Granqvist and A. Hjortsberg, “Surfaces for radiative cooling: Silicon monoxide films on aluminum,” *Appl. Phys. Lett.*, vol. 36, no. 2, pp. 139–141, Jan. 1980.

[17] P. Berdahl, “Radiative cooling with MgO and/or LiF layers,” *Appl. Opt.*, vol. 23, no. 3, p. 370, Feb. 1984.

[18] E. Rephaeli, A. Raman, and S. Fan, “Ultrabroadband Photonic Structures To Achieve High-Performance Daytime Radiative Cooling,” *Nano Lett.*, vol. 13, no. 4, pp. 1457–1461, Apr. 2013.

[19] A. P. Raman, M. A. Anoma, L. Zhu, E. Rephaeli, and S. Fan, “Passive radiative cooling below ambient air temperature under direct sunlight,” *Nature*, vol. 515, no. 7528, pp. 540–544, 2014.

Chapter 4

Nanostructured fibers as a versatile photonic platform: Radiative cooling and waveguiding

4.1 Background

Silkworm cocoon fibers are remarkable natural materials that act to protect the pupae from sudden temperature fluctuations, ultraviolet (UV) radiation, and predatory attacks.[1]–[5] These exceptional thermal, optical, and mechanical properties, combined with biocompatible and biodegradable properties, make silk fibers an ideal candidate for tissue engineering and other biomedical applications.[6]–[10] This study aims to build and expand upon the silk fiber's functionalities, bringing it closer to new applications in radiative cooling, light delivery, and image transport.

The moth species, of which its cocoon fibers are being studied here, is *Argema mittrei*, more commonly known as the comet moth. It is one of the largest moths in the world, with cocoons spanning 6-10 cm in length.[11] Under sunlight, the cocoons, as well as individual silk fibers that make up the cocoons, exhibit a bright silvery, metallic sheen (Figure 4.1, 4.2 a-b). While diffuse reflection in randomly structured materials is often observed in nature, light reflection with a high degree of specularity observed in these wild moth cocoon fibers is unique for a natural biological system.[12]–[15]

In Fig. 4.1, we show the dark field microscopy image of a domestic silkworm (*Bombyx mori*) cocoon and compares it to the wild comet moth cocoon, along with the optical images of complete cocoons. The domestic silkworm cocoon exhibits a diffused white shine, while the wild comet moth cocoon exhibits a high degree of specular shine. From the dark field optical microscopy images, it can be shown that the individual domestic silkworm cocoon fibers are mostly transparent, and the overall white shine is a result of multiple scattering at the boundaries of individual fibers. In the case for wild comet moth cocoon fibers, the individual fibers are highly reflective and specular in nature.

As we will show in this study, unique optical properties of these fibers are the results of filamentary air voids propagating along the cocoon fibers. The voids have cross-sectional sizes comparable to wavelengths of visible and near-infrared light, and thus act as scattering centers that enhance the solar reflectance of the fibers. Furthermore, the variety of chemical bonds of the silk proteins leads to a high emissivity in the mid-infrared. The combined effect of high solar reflectance and thermal emissivity enables the cocoons to regulate temperature via passive radiative cooling.[16]–[19] Drawing inspiration from the structure and optical properties of these natural fibers, we fabricated biomimetic fibers embedded with a high density of voids and characterized their radiative cooling capabilities. Aside from radiative cooling, the cocoon fibers with longitudinally invariant voids possess the ability to guide light along their longitudinal direction through transverse Anderson localization. The latter is a phenomenon first observed experimentally in 2007 in a photo-refractive crystal, where small random one-dimensional (1D) perturbations of optical refractive indices were introduced through an optical nonlinear effect.[20], [21] Since then, researchers have been able to create fibers

containing longitudinally invariant random structures using various fiber drawing techniques with different materials systems, and apply them towards applications in image transport, light focusing, and secure information transport.[22]–[27] This study shows the first experimental observation of transverse Anderson localization in a natural biological system, where potential applications in light guiding, image transport, and light focusing are demonstrated.

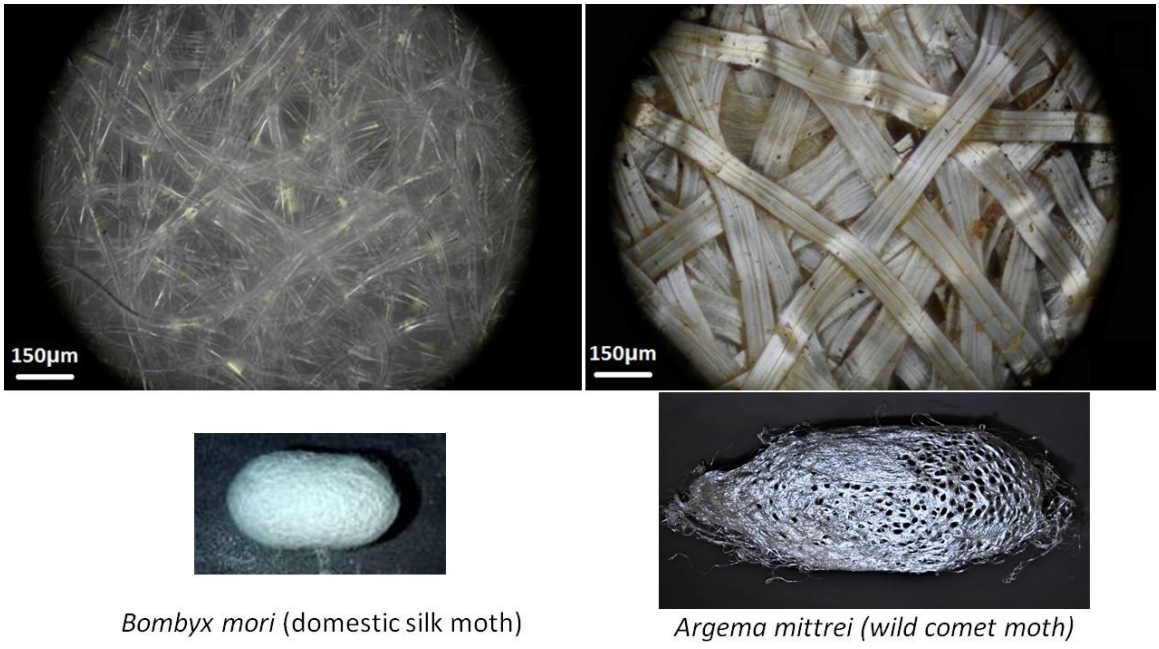

Figure 4.1 Dark field microscopy image and optical image of domestic silkworm cocoon (left) and wild comet moth cocoon (right).

4.2 Characterization

4.2.1 Morphology Characterization

The comet moth cocoon is made of threads, each consisting of a pair of fibers bonded together by a coating of sericin.[28] We used focused ion beam (FIB) milling to expose the fiber's transverse and longitudinal cross-sections. The transverse cross-section of one fiber (Fig 4.2C) shows that it has a diameter of ~40 μm and is populated by irregularly shaped voids with sizes ranging from hundreds of nanometers to a micron. Smaller voids tend to be located more toward the edge of the fiber and larger voids more toward the center. The region where sericin joins the two fibers together is free of voids. The longitudinal cross-section of a fiber (Figure 4.2D) shows that the voids propagate for at least tens of microns without varying in size.

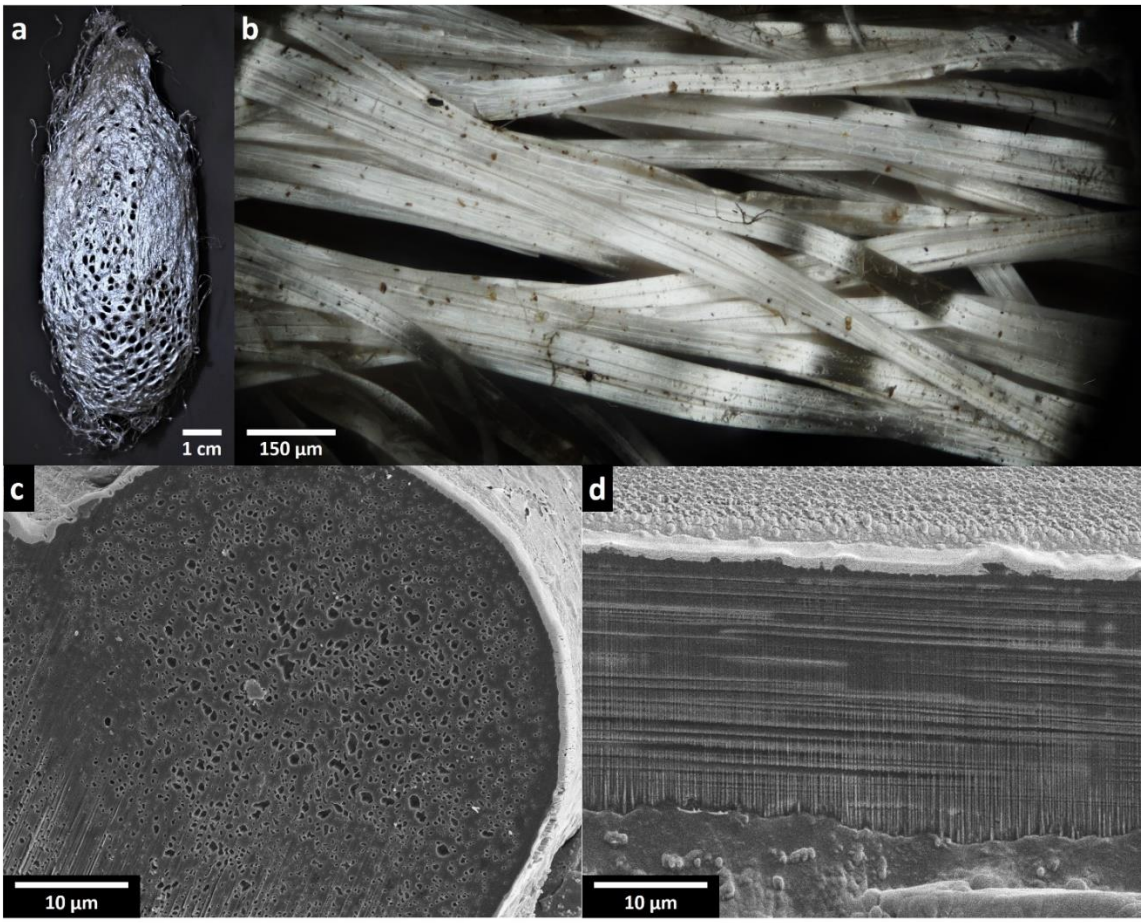

Figure 4.2 Morphology of the cocoon and silk fibers of the comet moth. (A) Photo of a comet moth cocoon, showing its reflective sheen. (B) Dark field optical microscopy image showing overlapping cocoon fibers. (C) Scanning electron microscopy (SEM) image of the transverse cross-section of a comet moth silk fiber, prepared with focused ion beam (FIB) milling. (D) SEM image of the longitudinal cross-section of a silk fiber prepared with FIB milling.

4.2.2 Reflectivity and emissivity characterization

Directional-hemispherical reflectance measurements on single silk fibers ~50 μm thick show that single fibers have a high reflectance of 0.66 normalized to the solar spectrum (Fig 4.3). The fibers' strong enhancement in reflectance is the result of multiple light scattering by the random voids inside the fibers, where the void sizes are comparable to the wavelengths of sunlight. At longer wavelengths, however, as the voids are now subwavelength in size and thus no longer act as strong scattering centers, reflectance is greatly reduced. In fact, the fibers become highly absorptive in the mid-infrared (λ=6-14 μm) due to strong and broadband absorption of a variety of chemical bonds of fibroin proteins that comprise the silk fibers. The wavelength range over which infrared absorptivity is enhanced overlaps well with the atmospheric transparency window (λ=8-14 μm) and the blackbody radiation spectrum of warm objects.[29], [30] Reduced reflectance and enhanced absorptivity in the mid-infrared enable the cocoon fibers to reach a high emissivity of 0.88, weighted by the thermal radiation spectrum at 300 K. In this way, the portion of solar energy absorbed by the cocoon can be efficiently dissipated back to the environment through thermal radiation. The combined effects of high solar reflectance and high thermal emissivity help prevent the pupae inside a cocoon from overheating when the cocoon is under direct sunlight.

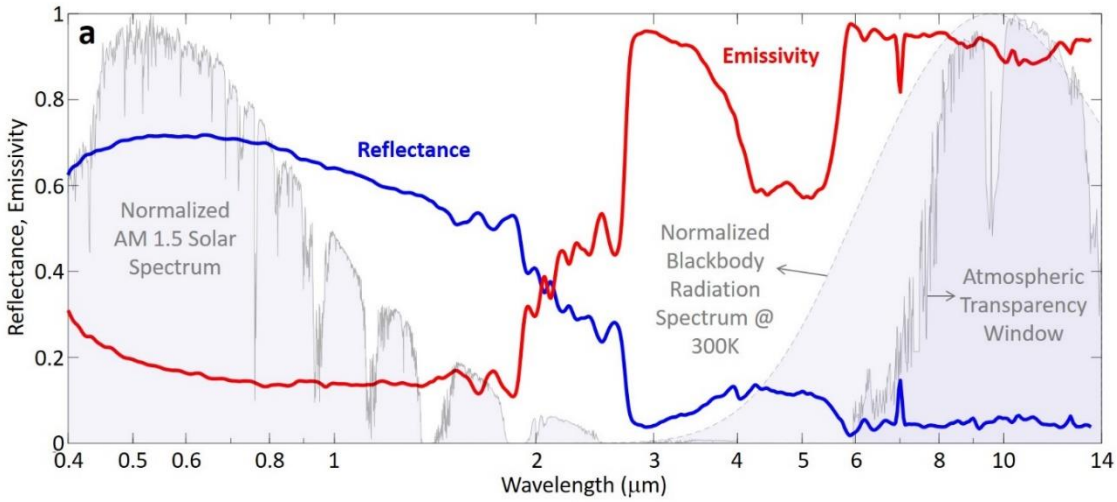

Figure 4.3 Optical characterization of single cocoon fibers. **(A)** Integrated hemispherical reflectance and emissivity (calculated by 1–reflectance–transmittance) spectra of a single comet moth cocoon fiber from the visible to the mid-infrared (λ=400 nm – 13.5 μm). Normalized spectral intensity of the AM 1.5 solar spectrum, the blackbody radiation spectrum at 300 K, and the atmospheric transparency window are plotted in the background.

4.2.3 Polarization dependent reflectivity

To further understand how these filamentary voids affect the optical properties of the fibers, and to understand the specular reflection of these fibers in the visible, we shone linearly polarized light onto single silk fibers and measured spatial, spectral, temporal, and polarization dependent properties of back- and forward-scattered light. The integrated reflectance of the silk fiber is significantly higher with an illumination of transverse electric (TE) polarized light compared to that with an illumination of

transverse magnetic (TM) polarized light (Fig 4.4D). Here, TE corresponds to the electric field parallel to the longitudinal direction of the fiber. This large difference in reflectivity is the result of form birefringence created by the filamentary voids, as is confirmed through finite-difference time-domain (FDTD) simulations.

FDTD simulations were used to investigate reflection of the cocoon fiber as a function of incident wave polarization. Actual transverse cross-sectional SEM image of a fiber was imported to obtain the structure used in FDTD simulations (Fig. 4.4). The voids were assumed to be completely invariant in the longitudinal direction of the fiber. A refractive index of n = 1.5 was assigned to the material at all wavelengths,[31] and no absorption was considered in the simulations.

The simulated reflectance results show that reflection of TE polarized incident light is higher than that of TM polarized light (Fig. 4.4). It is also observed that as the wavelength of light increases towards the near-infrared, reflectance decreases. This trend matches the measurement results, where the scattering strength of the material decreases as the wavelength of light becomes substantially larger than the size of the voids.

The scattering strength of these fibers can be quantified by using a cross-correlation measurement technique.[12] We measured the temporal profile of an ultrashort laser pulse at $\lambda = 600$ nm before and after it passed through a single cocoon fiber along the transverse direction (Figure 4.4E). The temporal profile before passing through the cocoon fiber was used as the instrument response function (IRF). The IRF was convolved with an exponential decay function to fit and extract the photon lifetime, which positively correlates with the strength of light scattering inside the random structures of the cocoon fiber. The measured photon lifetime is 210 fs for TE polarized light and 155 fs for TM

polarized light. The results agree qualitatively with the polarization dependent reflectivity measurements and FDTD simulation results, where TE polarized light interacts stronger with the filamentary voids when compared to TM polarized light.

The simulated temporal profile of an ultra-short pulse passing through a single cocoon fiber (Fig. 4.4C) confirms the time-of-flight measurement results, where TE polarized light interact stronger with the voids.. The simulated results estimated photon lifetimes of 270 fs for TE polarized light, and 230 fs for TM polarized light.

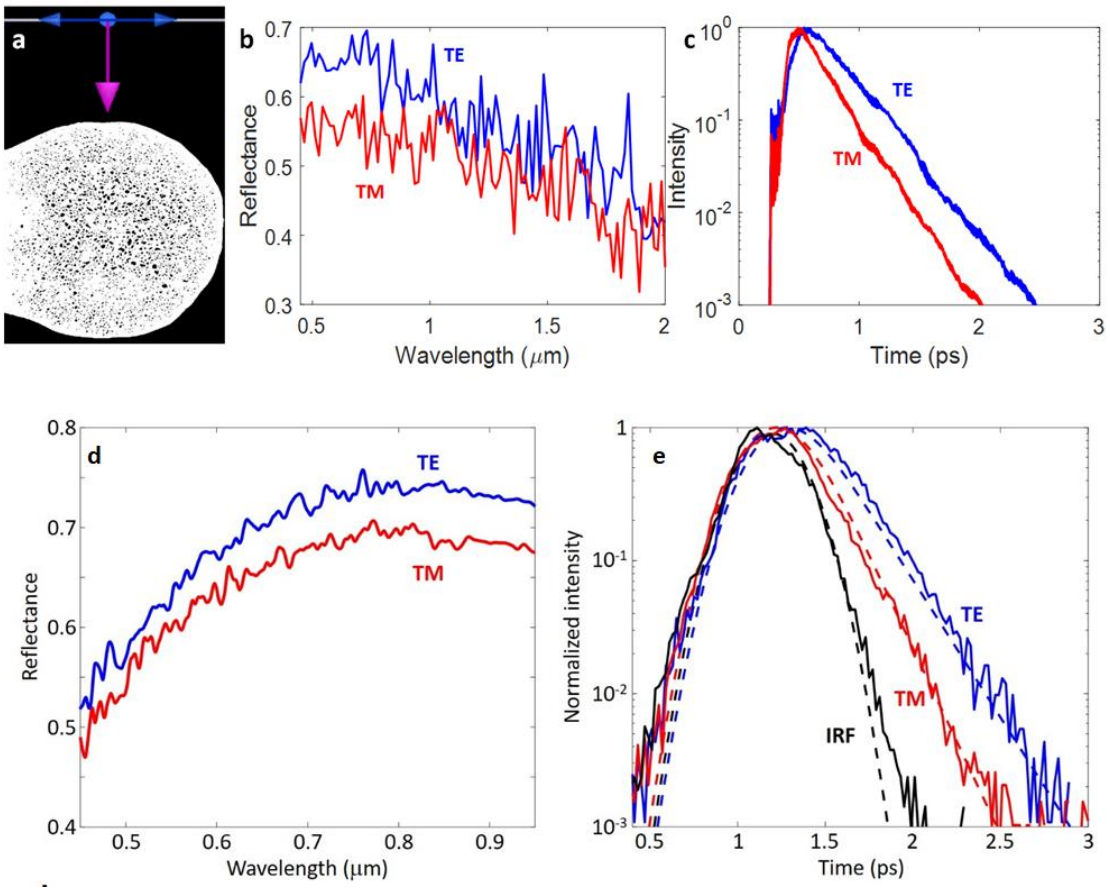

Figure 4.4 Polarization dependent optical simulation and measurement of single cocoon fibers. (A) Structure extracted from a cocoon fiber and used in the simulations. (B) FDTD simulations of the reflectance spectra of a single cocoon fiber with TE and TM polarized excitations. (C) FDTD simulations of the temporal profile of an ultrashort pulse passing through a single cocoon fiber with TE and TM polarized light. (D) Integrated hemispherical reflectance spectra of a single cocoon fiber illuminated with transverse electric (TE) and transverse magnetic (TM) polarized light at normal incidence, where TE polarization is defined with the electric field aligned to the longitudinal direction of the fiber. (E) Time-of-flight measurements of a single cocoon fiber. IRF stands for instrument response function, which is the cross-correlation of ultra-short reference (λ=800 nm) and probe (λ=600 nm) pulses.

4.2.4 Specularity of cocoon fibers

These filamentary voids are also what enable these silk fibers to exhibit a strong specular sheen, where the 1D nature of these voids limits the scattered light to within a narrow angular range in the far field. The effect was demonstrated by imaging the forward scattering pattern of a laser beam at λ = 633 nm focused onto a single fiber. Figure 2d shows that a single cocoon fiber has a far-field scattering pattern of a narrow horizontal stripe, perpendicular to the vertically oriented fiber, indicating highly directional scattering as a result of the filamentary voids. As a comparison, a regenerated silk fiber of similar width and thickness, filled with three-dimensional (3D) voids, produces a diffused scattering pattern with no preferential scattering direction (Fig. 4.5).

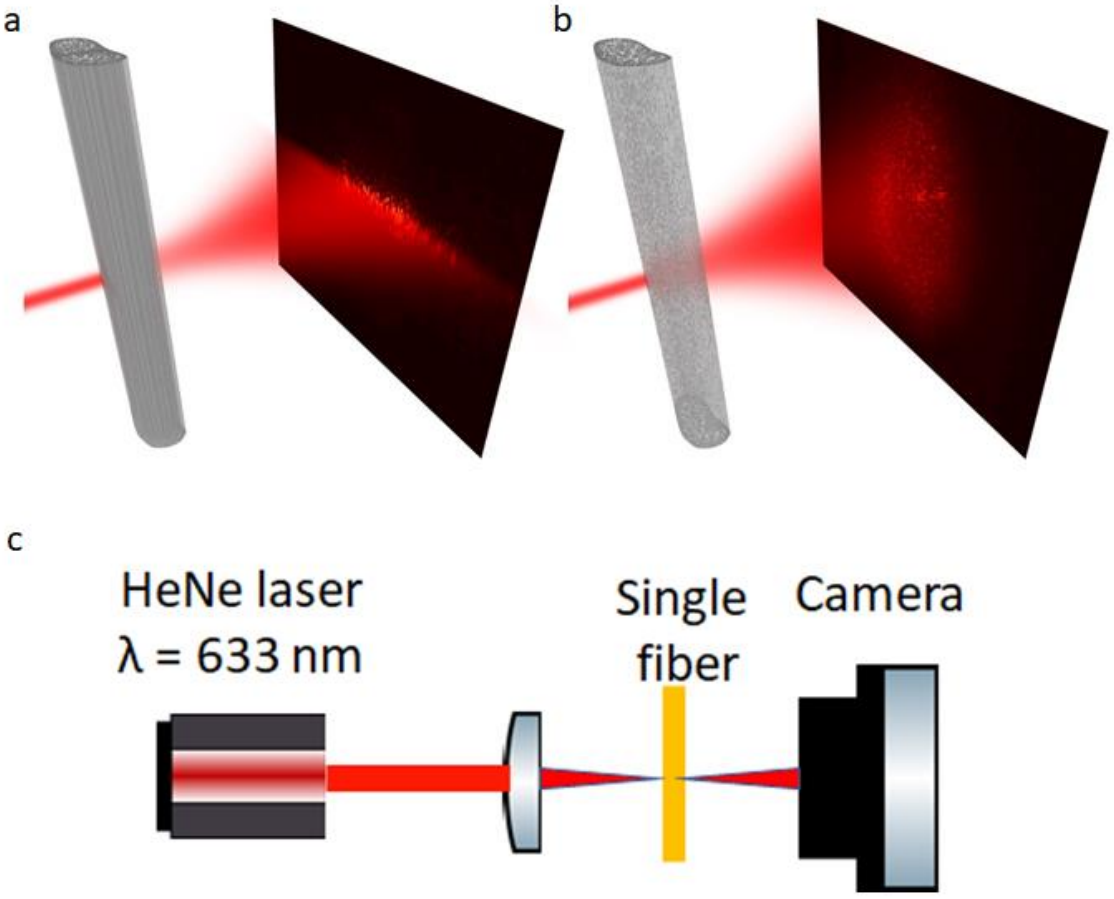

Figure 4.5 (A) Schematic showing a focused laser beam at λ=633 nm passing through a single cocoon fiber oriented in the vertical direction. Measured scattering pattern is shown on the right. Filamentary voids along the fiber prevents excessive scattering in the vertical direction, so the scattering pattern forms a horizontal narrow band. (B) Schematic showing the focused laser beam passing through a regenerated silk fiber bundle (as a control) containing a high density of nanoscale spherical voids (Fig. 4b). Measured scattering pattern on the right shows that there is no preferential scattering direction due to the 3D nature of the voids. (C) Schematic diagram of the far-field scattering pattern characterization technique.

4.3 Biomimetic fibers

We have shown that fibers of the wild comet moth possess passive radiative cooling capabilities. The capabilities, however, are limited by materials absorption in the solar spectrum and density of voids. Drawing inspiration from the natural silk fibers, we explored alternative materials of choice and fiber pulling techniques to create biomimetic fibers with optimized radiative cooling capabilities.

4.3.1 Regenerated silk fibroin fibers

We obtained regenerated silk fibroin from cocoons made by the domestic silk moth, *Bombyx mori*.[32] By chemically removing sericin, regenerated fibroin offers substantially reduced absorption in the visible and near-infrared part of the solar spectrum,[31] while providing similar absorption in the mid-infrared as natural silk fibers. Researchers have demonstrated that fibers extruded through wet spinning from a solution of regenerated fibroin have a larger tensile strength than natural *Bombyx mori* fibers.[33] We modified and optimized the fiber spinning recipes reported in the literature,[34] in particular, the concentrations of the silk fibroin solution and the coagulation bath, in order to maximize the density of voids inside the wet spun fibers (Fig. 4.6B). We found that a concentration of silk fibroin of 13.9% yields the highest density of voids. The regenerated silk fibroin fibers were first spun onto a motorized drum at a controlled speed to achieve a thickness of a few tens of microns. The voids were then further stretched into a filamentary form through a drawing process by a second motorized drum, two to four times faster than the first one. Spectral measurements of ~100-μm thick bundles of regenerated silk fibers with a high density of

voids showed that the fiber bundle has an integrated solar reflectance of 0.73 and an integrated thermal emissivity of 0.90 (Figure 4.6A).

4.3.2 Polymer based fibers

While the fibers made from regenerated fibroin provide good optical properties, silk fibroin's proneness to long-term UV radiation, and water and heat damage, and its cost as a raw material significantly limit its applications in radiative cooling applications.[35], [36] A widely available thermoplastic, polyvinylidene difluoride (PVDF), which is highly resistant to UV radiation, heat and water damage, and has low absorption in the solar spectrum, was explored as an alternative material.[37], [38] By properly choosing the solvent and the ratio between PVDF and the solvent, as well as the coagulation bath, we were able to pull PVDF fibers containing 3D voids (Fig. 4.6D). A similar drawing process was used to stretch the voids into a filamentary form (Fig. 4.6E). Optical measurements on pre-drawn thicker fibers, ~100 μm in diameter, showed that the fibers have a high reflectance of 0.93 in the solar spectrum and a high emissivity of 0.91 (Fig. 4.6a). We note that our regenerated silk and PVDF biomimetic fibers both have a higher solar reflectance compared to the comet moth fiber; this is primarily due to a higher density of voids created in the biomimetic fibers (i.e., 5.5 voids/μm^2 for the regenerated silk fiber, 17 voids/μm^2 for the PVDF fiber, and 2.2 voids/μm^2 for the comet moth fiber). We also note that the filamentary voids in our biomimetic fibers are not as long as those observed in the cocoon fibers made by the comet moth. The natural silk fibers' amazing capability of maintaining longitudinal invariance motivated us to investigate light

propagation along these nanostructured fibers confined by strong light scattering in the transverse direction.

4.3.3 Fabrication of biomimetic fiberse using silk fibroin and PVDF

Degummed *Bombyx mori* silk fibers were obtained and used as the starting point of the fibroin preparation process.[32] A solution of 9.3-M lithium bromide (LiBr) was used to dissolve the silk fibers. A 20% weight-to-volume ratio (i.e., 1 g VS 4 ml) between silk fibroin and the LiBr solution was used to prepare a fibroin-LiBr solution. The fibroin-LiBr solution was left to completely dissolve in an oven set to 60˚C for 4 hours. The dissolved solution was transferred to a dialysis cassette (10 ml, 3500 MWCO), and dialyzed against deionized water for 48 hours. A centrifuge step was used to remove impurities that were left in the solution. The fibroin-LiBr solution was further concentrated with a second set of dialysis cassettes (3 ml, 10000 MWCO), where the solution was dialyzed against a 10% Polyethylene glycol (PEG, 20 kDa) solution for 14-20 hours to achieve the desired concentrations (12-18%).

PVDF solutions were prepared by dissolving Poly (vinylidene fluoride-co-hexafluoropropylene) (PVDF-HFP) in Dimethylacetamide (DMA), with a weight ratio of 1:5 between PVDF-HFP and DMA.

Both silk fibroin and PVDF biomimetic fibers were fabricated using wet spinning. In the case of regenerated silk fibers, 30% ammonium sulfate solution was used as the coagulant, while in the case of PVDF fibers, deionized water was used as the coagulant. A syringe pump connected to a 28-gauge stainless steel, blunt-tip needle was used to extrude the solutions. As the solution entered the coagulation bath, phase separation and

polymer precipitation occurred, where a polymer lean phase and a polymer rich phase were generated in the fiber. Eventually the portion of the fiber with polymer lean phase became the voids. These newly solidified porous fibers were spun onto a motorized drum at a controlled speed to achieve the desired fiber diameters. The aspect ratio of the voids could be modified through a draw-down process using a second motorized drum at a higher speed compared to the first drum, where a certain degree of elongation of the voids could be achieved inside the fiber.

Silk solutions at various concentrations (12.7, 13.9, 14.5, and 18.9%) were extruded into the coagulation bath at 20 ml/hr. The speeds of the take up drum and draw-down drum were set at 4-8 m/min and 10-20 m/min, respectively. PVDF solutions were extruded into the coagulation bath at 10 ml/hr. The speeds of the take up drum and draw-down drum were set at 1-2 m/min and 2-4 m/min, respectively.

Cross-sectional scanning electron microscopy (SEM) images of the comet moth cocoon fibers were binarized by utilizing the image contrast between the voids and the surrounding solid fibroin regions (Fig. 4.7). An image processing software, ImageJ, was then used to obtain the sizes of all the voids inside the fiber. The histogram of void sizes is shown in Fig 4.7. The diameters of the voids are shown to range from a few tens of nanometers to about a micron in size. The average void size is 236 nm, the void density is 2.2 voids/μm^2, and the air-void filling fraction is 9.8% for this particular fiber. Similar processing techniques were used in the case of biomimetic regenerated silk and PVDF fibers, where the average void size is 145 nm and 106 nm in diameter, the void density is 5.5 and 17 voids/μm^2, and the air-void filling fraction is 14.5% and 17.7%, respectively.

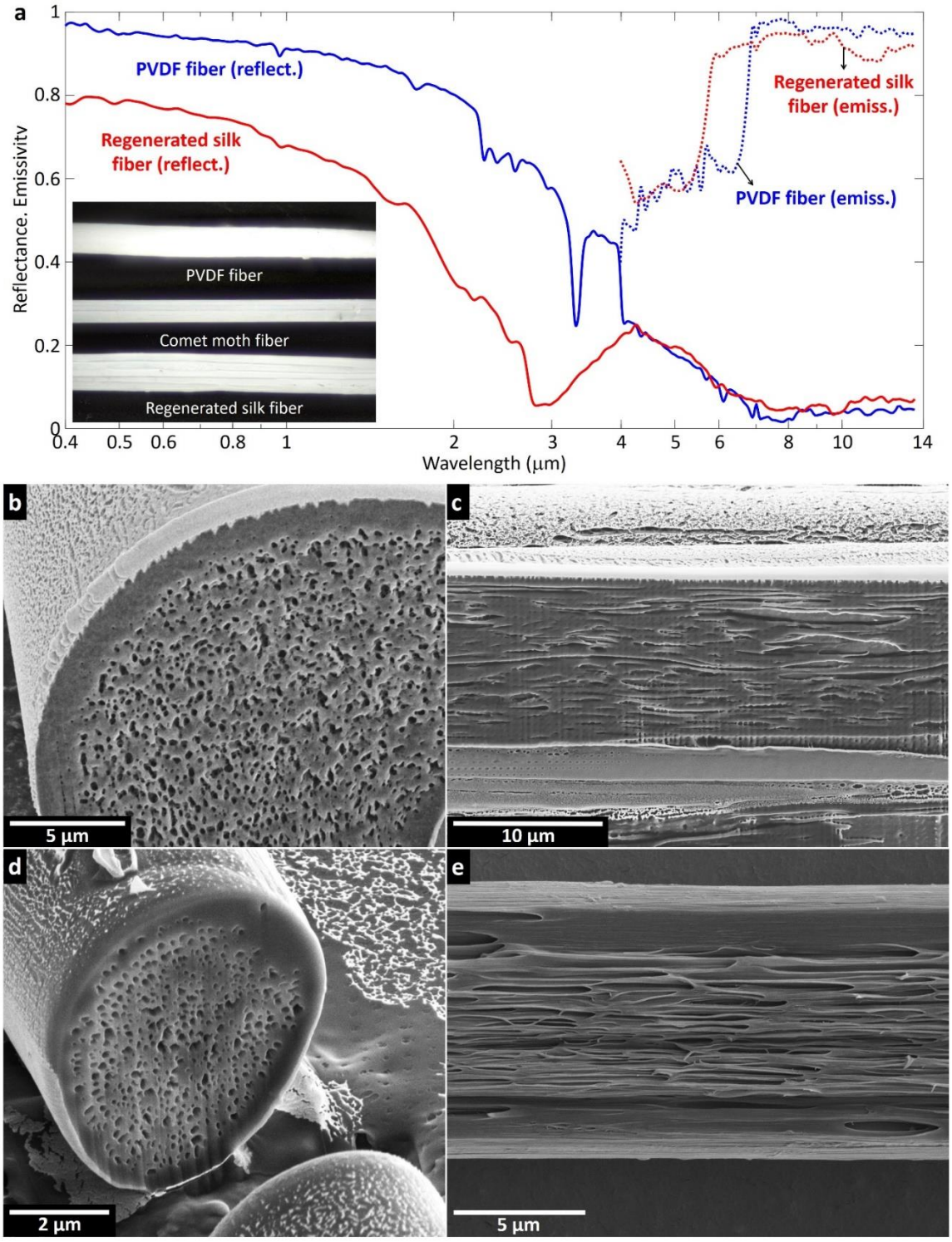
a
PVDF fiber (reflect.)
Regenerated silk fiber (reflect.)
Regenerated silk fiber (emiss.)
PVDF fiber (emiss.)
PVDF fiber
Comet moth fiber
Regenerated silk fiber
Reflectance. Emissivity
Wavelength (μm)
b
5 μm
c
10 μm
d
2 μm
e
5 μm

Figure 4.6 Biomimetic fibers with a high density of internal voids for radiative cooling. a) Integrated hemispherical reflectance and emissivity spectra of a ~100-μm thick bundle of regenerated silk fibers and a single PVDF fiber of ~100-μm diameter from the visible to the mid-infrared. Inset shows a photo of a nanostructured PVDF fiber, a bundle of nanostructured regenerated silk fibers, and a thread of the comet moth. b) and c) SEM images of transverse and longitudinal cross-sections, respectively, of a regenerated silk fiber containing a high density of voids. d) and e) SEM images of transverse and longitudinal cross-sections, respectively, of a PVDF fiber containing a high density of voids.

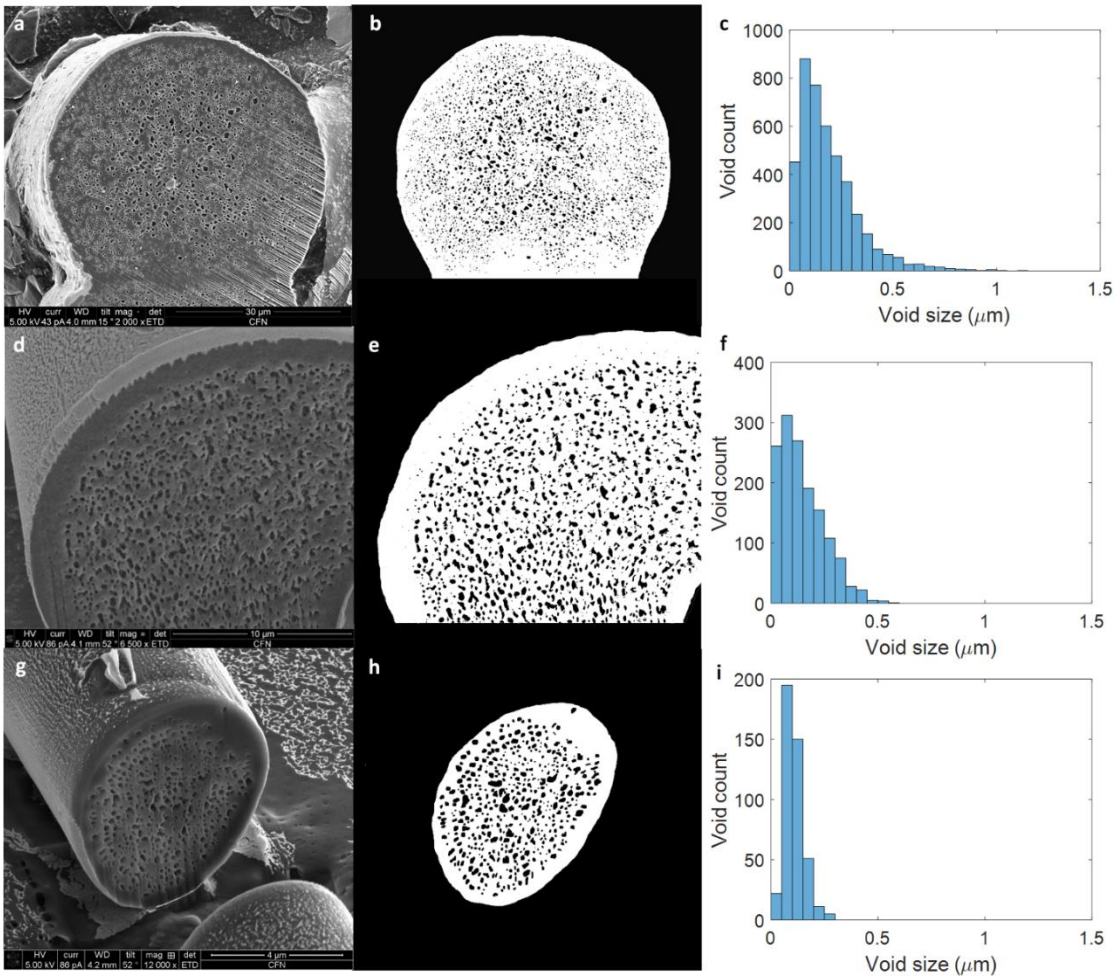

Figure 4.7 First column: SEM images of the transverse cross-section of a comet moth cocoon fiber (top), a regenerated silk fiber (middle), and a biomimetic PVDF fiber (bottom). Second column: Binarized images of the SEM images outlining all the voids. Third column: Histograms showing the size distributions of the voids.

4.3.4 Correlation between void concentration and reflectivity in the visible and NIR

To further clarify the correlation between void concentrations and fiber reflectance over the solar spectrum, we fabricated regenerated silk fibers and PVDF fibers with both high and low void concentrations and measured their reflectance over the solar spectrum (Fig. 4.8). The reflectance measurement clearly shows that PVDF and regenerated silk fibers with high void concentrations are significantly more reflective in the solar spectrum when compared to PVDF and regenerated silk fibers with low void concentrations. The correlation between void concentration and reflectivity is further confirmed by the dark field optical microscopy images of high and low void concentration PVDF and regenerated silk fibers, which shows high void concentration PVDF and regenerated silk fibers with a bright, diffused white shine, a clear indication of strong scattering. Low void concentration PVDF and regenerated silk fibers, on the other hand, appears to be semi-transparent as a result of low concentration of scattering centers.

The void concentrations of the regenerated silk fibers were controlled by the initial concentration of the regenerated silk solution, a concentration of 13.9% and 18.9% were used to fabricate high and low void concentration fibers, respectively (Fig. 4.8). The void concentration of the PVDF fibers were controlled by the amount of time the fibers stays in the coagulation bath after it has been drawn. The high void concentration fibers used here did not go through a coagulation bath soak, while the low void concentration fiber was soaked in the coagulation bath for 40 hours immediately after the fiber was drawn (Figs. 4.8C-D).

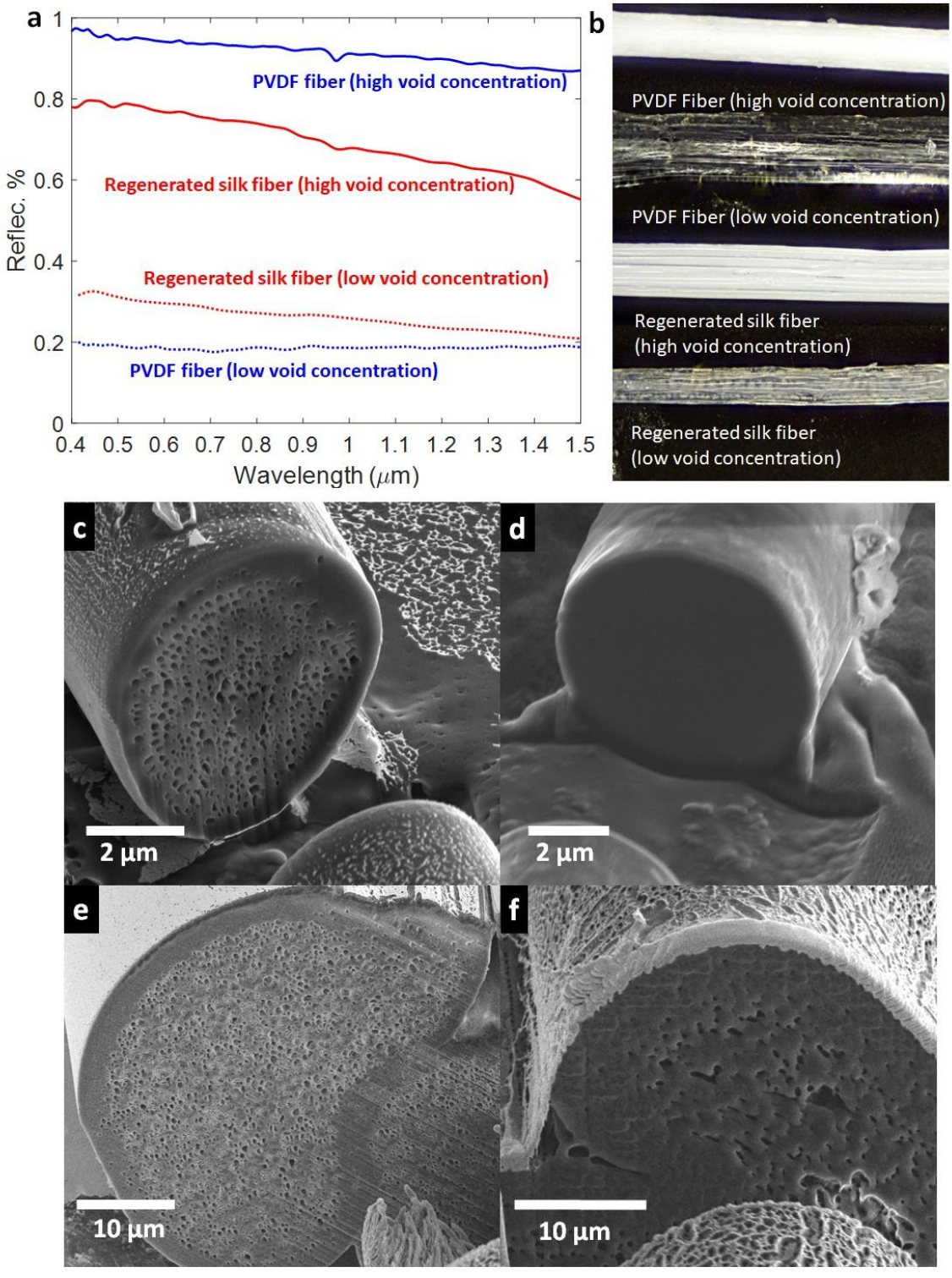
a
b
c
d
e
f
Reflec. %
Wavelength (μm)
PVDF fiber (high void concentration)
Regenerated silk fiber (high void concentration)
Regenerated silk fiber (low void concentration)
PVDF fiber (low void concentration)
PVDF Fiber (high void concentration)
PVDF Fiber (low void concentration)
Regenerated silk fiber
(high void concentration)
Regenerated silk fiber
(low void concentration)
2 μm
2 μm
10 μm
10 μm

Figure 4.8 Reflection study of biomimetic fibers with high and low void concentration (a) Integrated hemispherical reflectance in the visible and near-infrared (λ = 0.4 μm – 1.5 μm) for regenerated silk and PVDF fibers with high and low void concentrations. (b) Dark field optical microscopy images of regenerated slik and PVDF fibers with high and low void concentrations. (c-d) Cross-sectional SEM images of high and low concentration PVDF fibers. (e-f) Cross-sectional SEM images of high and low concentration regenerated silk fibroin fibers.

4.4 Transverse Anderson localization

Anderson localization in 3D systems requires a critical level of scattering strength, quantified by the Ioffe–Regel criterion, which can be satisfied in high refractive-index contrast materials systems.[39] However, the scaling theory of localization dictates that Anderson localization will always occur in random two-dimensional coupled waveguide arrays, even for low refractive-index contrast systems.[40] In the case of transverse Anderson localization, a beam first undergoes diffusive broadening as it propagates along the longitudinal direction of the waveguide array, but eventually reaches a mean localization radius, called localization length ξ, as it propagates further down the array. The onset of transverse localization can be characterized by an exponentially decaying tail of the beam's transverse intensity profile. The localization length ξ of guided light beam and the mean free path l^* of photons propagating in the nanostructured fibers can be estimated by using equations

$$I \sim \exp(-2|r|/\xi) \tag{4.1}$$

$$\xi = I^{*}\exp(\pi k_{\perp} I^{*2}/2) \quad (4.2)$$

where I is the beam intensity profile, r is the distance from the beam center, $k_{\perp} = 2/\omega_o$ is the transverse wavenumber, and ω_o is the initial width of the beam at the entrance facet of the fiber.[20]

4.4.1 Observation of transverse Anderson localization

We characterized how a light beam broadens and eventually reaches full confinement as a result of transverse Anderson localization in comet moth fibers. A set of fiber segments with different lengths (L = 300, 400, 720, and 1500 μm) were cut and the facets polished using FIB milling. All the fiber segments were from the same fiber and cut next to one another to minimize variations of their cross-sectional void pattern. A high numerical aperture (NA = 0.55) objective was used to launch a focused beam at one facet of a fiber segment, and the exit facet was imaged with a matching objective to characterize the beam upon exiting the segment. Figure 4.9A shows the intensity distribution at the exit facet of a fiber segment (L = 720 μm, λ = 600 nm). The black curve within Figure 4.9A shows the logarithm of the average line intensity profile through the center of the beam, and its linear slopes are an indication of transverse Anderson localization. The line intensity profiles for the four fiber segments with different lengths (Figure 4.9B) show the evolution of the beam profile from initial diffusive broadening to eventual full confinement as L increases. Figure 4.9C shows the line intensity profiles for the fiber segment with L = 720 μm at various wavelengths (λ = 450, 500, 600, and 700 nm). It is observed that, while the beam stays localized with increasing wavelengths (at least up to

λ = 850 nm), the localization length ξ increases with increasing wavelengths. The localization length ξ of the fiber at λ = 600 nm, for example, can be estimated by fitting equation. (4.1) to the exponentially decaying tail of the line intensity profile, yielding ξ = 4.6 μm, which is smaller than that of recent work utilizing a man-made high refractive-index contrast system of glass and air.[41] The mean free path l^* at λ = 600 nm can be calculated using equation (4.2), where the entrance beam size ω_0 is ~2 μm, yielding l^* ~ 0.98 μm, which is significantly smaller than those reported in early demonstrations of transverse Anderson localization with low refractive-index contrast systems,[20], [24]

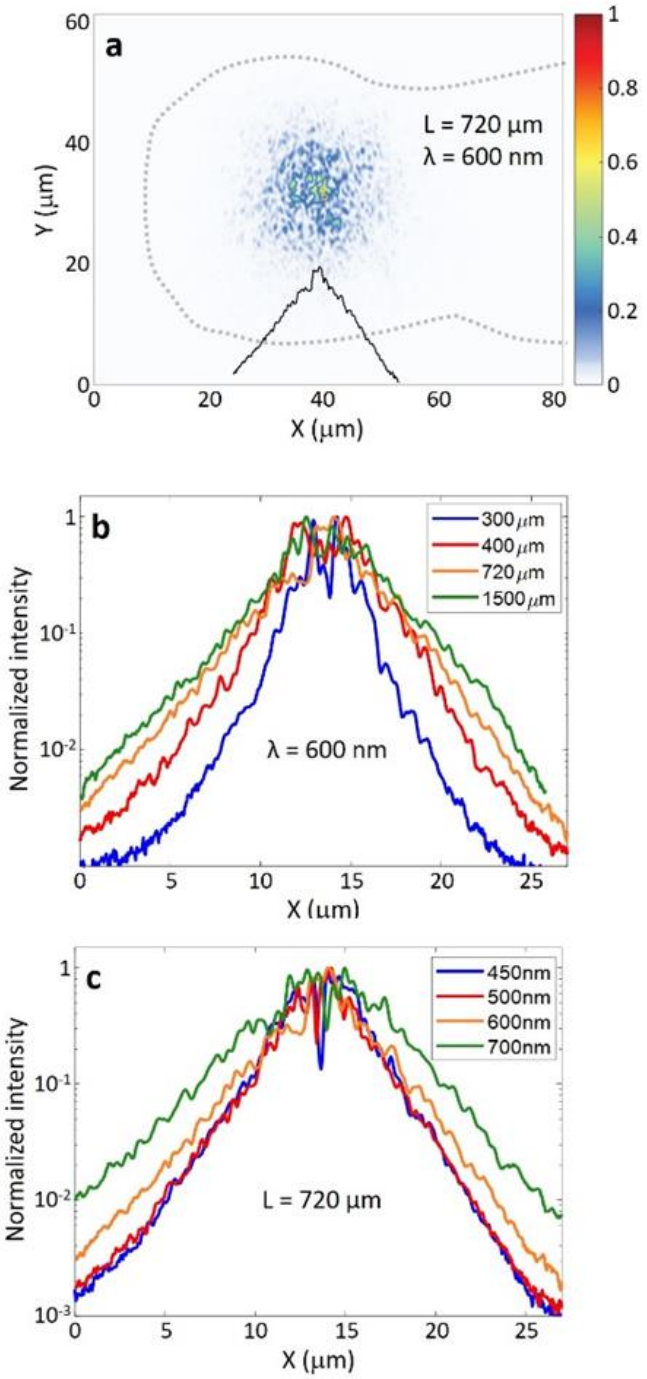

Figure 4.9 Transverse Anderson localization in comet moth cocoon fibers. a) Intensity distribution of a beam at λ = 600 nm under transverse localization exiting the end facet of

a cocoon fiber ~720 μm in length. The dotted line shows the outer edge of the fiber. The black curve in the figure shows the logarithm of the averaged line intensity profile of the beam. b) Logarithm of averaged line intensity profiles at the exit facet for fibers of different lengths. c) Logarithm of averaged line intensity profiles at the exit facet for a fiber with length L = ~720 μm at different wavelengths.

4.4.2 Waveguiding and image transport in comet moth cocoon fibers

The small localization length compared to the transverse size of the fibers also enables the fiber system to transport simple patterns. Figure 4.10F shows an optical image of a series of apertures 1 μm in diameter, milled using FIB in a gold thin film and forming a 30-μm diameter ring. The aperture pattern was then butt coupled to the entrance facet of a fiber segment of length 400 μm, and illuminated with a large-diameter beam at λ = 600 nm. The image at the exit facet of the fiber segment (Figure 4.10G) is a discernible ring pattern, where the resolution of the transported image is limited by the localization length of the system.

As the position of the fiber facet moves with respect to the input beam, light can sometimes be tightly confined in certain regions of the fiber that are free of voids (thus serving as a waveguide core) and surrounded by a high density of scattering centers. Figure 4A-D shows one of these confined hotspots, where the confinement is maintained as the wavelength varies from 425 to 650 nm. The full-width at half-maximum (FWHM) sizes of the hotspot at λ = 425, 550, and 650 nm are 0.75, 0.94, and 1 μm, respectively, which are smaller than the spot size of the entrance beam (~2 μm). The focusing abilities of the cocoon fibers have the potential to be further enhanced through wavefront shaping

and optimization with adaptive optics.[22] Aside from waveguiding through transverse Anderson localization, Figure 4.10E shows that these silk fibers can also act as a slab waveguide: the sericin region free of voids can act as a waveguide core and lateral confinement is provided by scattering centers in the fibers.

It's crucial to note that the silk materials have intrinsic absorption in the visible spectrum (sericin being more absorptive than fibroin in shorter wavelengths), and that the filamentary voids in fact slowly morph along the longitudinal direction. As a consequence, these interesting optical properties and potential applications discussed above related to transverse Anderson localization cannot be realized in fibers longer than a few millimeters. Potential reduction in propagation losses, however, is possible by chemically removing the sericin coating surrounding silk fibers.[42]

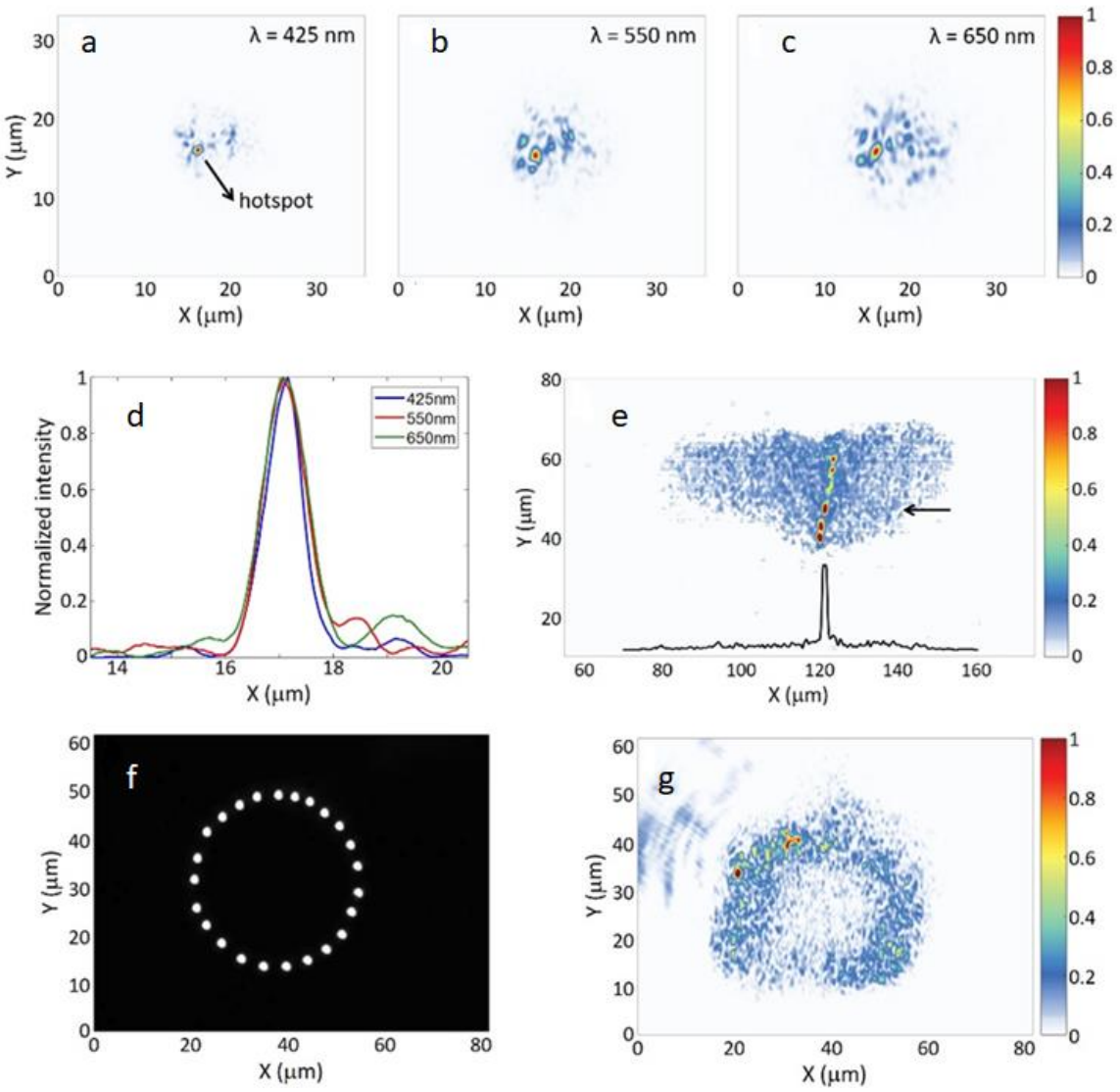

Figure 4.10 (A-C) Intensity distributions showing a highly localized hotspot in a fiber with length L = ~150 μm at three wavelengths. (D) Profiles of the hotspot at the three wavelengths. (E) Intensity distribution showing light being guided by a sericin slab region between two cocoon fibers. The black curve shows the profile of the guided mode at a location indicated by an arrow. (F) Optical image of a ring of 1-μm apertures used

for image transport through a cocoon fiber with length L = ~400 μm. (G) Intensity distribution at the exit facet of the fiber showing the transport of the ring pattern.

4.5 Conclusion

In summary, we explored nanostructured voids discovered in the silk fibers of the comet moth. We characterized the one-dimensional nature of these voids and their scattering strength through polarization dependent reflectance measurements, time-of-flight measurements, and far-field 9 scattering pattern measurements. We explored the radiative cooling properties of the silk fibers enabled by high solar reflectance through back-scattering of nanostructured voids in the visible and near-infrared, and high thermal emissivity enabled by intrinsic materials absorption in the midinfrared. Drawing inspiration from the natural system, we spun biomimetic fibers using regenerated silk fibroin and PVDF, which showed exceptional optical properties for radiative cooling applications. Furthermore, we observed for the first time transverse Anderson localization in a natural biological fiber system. These silk fibers have the potential to be used for delivering optical power and transporting images in situations where the fiber needs to be biocompatible and bioresorbable, such as optical therapy and imaging inside living tissues. Future work may benefit from investigating the mechanism behind the fiber pulling process utilized by wild silk moths that create silks with filamentary voids, in order to create bioinspired fibers with longitudinally invariant voids.

4.6 References

[1] Z. Shao and F. Vollrath, “Surprising strength of silkworm silk,” *Nature*, vol. 418, no. 6899, p. 741, 2002.

[2] J. Zhang, R. Rajkhowa, J. L. Li, X. Y. Liu, and X. G. Wang, “Silkworm cocoon as natural material and structure for thermal insulation,” *Mater. Des.*, vol. 49, pp. 842–849, 2013.

[3] C. S. Hieber, “The ‘insulation’ layer in the cocoons of Argiope aurantia (Araneae: Araneidae),” *J. Therm. Biol.*, vol. 10, no. 3, pp. 171–175, 1985.

[4] J. Kaur, R. Rajkhowa, T. Tsuzuki, K. Millington, J. Zhang, and X. Wang, “Photoprotection by silk cocoons,” *Biomacromolecules*, vol. 14, no. 10, pp. 3660–3667, 2013.

[5] J. Zhang, J. Li, X. Jin, S. Du, J. Kaur, and X. Wang, “Natural and highly protective composite structures – Wild silkworm cocoons,” *Compos. Commun.*, vol. 4, no. December 2016, pp. 1–4, 2017.

[6] G. H. Altman, F. Diaz, C. Jakuba, T. Calabro, R. L. Horan, J. Chen, H. Lu, J. Richmond, and D. L. Kaplan, “Silk-based biomaterials,” *Biomaterials*, vol. 24, no. 3, pp. 401–416, 2003.

[7] F. G. Omenetto and D. L. Kaplan, “A new route for silk,” *Nat. Photonics*, vol. 2, no. 11, pp. 641–643, 2008.

[8] F. G. Omenetto and D. L. Kaplan, “New Opportunities for an Ancient Material,” *Science (80-.).*, vol. 329, no. 5991, pp. 528–531, 2010.

[9] N. Huby, V. Vie, A. Renault, S. Beaufils, T. Lefevre, F. Paquet-Mercier, M. Pezolet, and B. Beche, “Native spider silk as a biological optical fiber OP - Applied Physics Letters, 2013, Vol.102(12),” *Appl. Phys. Lett.*, vol. 102, no. 12, 2017.

[10] Y. Reddy, Narendra; Jiang, Qiuran; Yang, “Biocompatible Natural Silk Fibers from Argema mittrei,” *J. biobased Mater. bioenergy*, vol. 6, pp. 558–563, 2012.

[11] P. GRIVEAUD, “The Invertebrates,” in *Key Environments: Madagascar*, vol. III, Elsevier, 1984, pp. 75–88.

[12] M. Burresi, L. Cortese, L. Pattelli, M. Kolle, P. Vukusic, D. S. Wiersma, U. Steiner, and S. Vignolini, “Bright-white beetle scales optimise multiple scattering of light,” *Sci. Rep.*, vol. 4, pp. 1–8, 2014.

[13] L. Cortese, L. Pattelli, F. Utel, S. Vignolini, M. Burresi, and D. S. Wiersma, “Anisotropic Light Transport in White Beetle Scales,” *Adv. Opt. Mater.*, vol. 3, no. 10, pp. 1337–1341, 2015.

[14] B. D. Wilts, X. Sheng, M. Holler, A. Diaz, M. Guizar-Sicairos, J. Raabe, R. Hoppe, S. H. Liu, R. Langford, O. D. Onelli, D. Chen, S. Torquato, U. Steiner, C. G. Schroer, S. Vignolini, and A. Sepe, “Evolutionary-Optimized Photonic Network Structure in White Beetle Wing Scales,” *Adv. Mater.*, vol. 1702057, pp. 1–6, 2017.

[15] D. G. Stavenga, S. Stowe, K. Siebke, J. Zeil, and K. Arikawa, “Butterfly wing colours: scale beads make white pierid wings brighter,” *Proc. R. Soc. B Biol. Sci.*, vol. 271, no. 1548, pp. 1577–1584, 2004.

[16] A. P. Raman, M. A. Anoma, L. Zhu, E. Rephaeli, and S. Fan, “Passive radiative cooling below ambient air temperature under direct sunlight,” *Nature*, vol. 515, no. 7528, pp. 540–544, 2014.

[17] N. N. Shi, C.-C. Tsai, F. Camino, G. D. Bernard, N. Yu, and R. Wehner, “Keeping cool: Enhanced optical reflection and radiative heat dissipation in Saharan silver ants,” *Science (80-.).*, vol. 349, no. 6245, pp. 298–301, 2015.

[18] P.-C. Hsu, A. Y. Song, P. B. Catrysse, C. Liu, Y. Peng, J. Xie, S. Fan, and Y. Cui, “Radiative human body cooling by nanoporous polyethylene textile,” *Science (80-.).*, vol. 353, no. 6303, pp. 1019–1023, 2016.

[19] J. K. Tong, X. Huang, S. V. Boriskina, J. Loomis, Y. Xu, and G. Chen, “Infrared-Transparent Visible-Opaque Fabrics for Wearable Personal Thermal Management,” *ACS Photonics*, vol. 2, no. 6, pp. 769–778, 2015.

[20] T. Schwartz, G. Bartal, S. Fishman, and M. Segev, “Transport and Anderson localization in disordered two-dimensional photonic lattices,” *Nature*, vol. 446, no. 7131, pp. 52–55, 2007.

[21] H. De Raedt, A. Lagendijk, and P. De Vries, “Transverse localization of light,” *Phys. Rev. Lett.*, vol. 62, no. 1, pp. 47–50, 1989.

[22] M. Leonetti, S. Karbasi, A. Mafi, and C. Conti, “Light focusing in the Anderson regime,” *Nat. Commun.*, vol. 5, pp. 1–6, 2014.

[23] M. Leonetti, S. Karbasi, A. Mafi, E. Delre, and C. Conti, “Secure information transport by transverse localization of light,” *Nat. Publ. Gr.*, no. June, pp. 1–7,

2016.

[24] S. Karbasi, C. R. Mirr, P. G. Yarandi, R. J. Frazier, K. W. Koch, and A. Mafi, "Observation of transverse Anderson localization in an optical fiber," *Opt. Lett.*, vol. 37, no. 12, p. 2304, 2012.

[25] S. Karbasi, T. Hawkins, J. Ballato, K. Koch, and A. Mafi, "Transverse Anderson localization in a glass optical fiber with random air-holes," *Opt. Fiber Commun. Conf. Fiber Opt. Eng. Conf. 2013*, vol. 2, no. 11, p. OTu2G.4, 2013.

[26] S. Karbasi, R. J. Frazier, K. W. Koch, T. Hawkins, J. Ballato, and A. Mafi, "mediated by transverse Anderson localization," *Nat. Commun.*, vol. 5, pp. 1–9, 2014.

[27] S. Karbasi, C. R. Mirr, R. J. Frazier, P. G. Yarandi, K. W. Koch, and A. Mafi, "Detailed investigation of the impact of the fiber design parameters on the transverse Anderson localization of light in disordered optical fibers," *Opt. Express*, vol. 20, no. 17, p. 18692, 2012.

[28] M. Mondal, K. Trivedy, and S. N. Kumar, "The silk protein,sericin and fibroin in silkworm,Bombyx mori Linn,-a review," *Casp. J Env Sci*, vol. 5, no. nE, pp. 63–76, 2007.

[29] M. Boulet-Audet, F. Vollrath, and C. Holland, "Identification and classification of silks using infrared spectroscopy," *J. Exp. Biol.*, vol. 218, no. 19, pp. 3138–3149, 2015.

[30] R. S. John R. Howell, M. Pinar Menguc, *Thermal Radiation Heat Transfer*, 5th ed.

Taylor & Francis Group, 2011.

[31] G. Perotto, Y. Zhang, D. Naskar, N. Patel, and D. L. Kaplan, “The optical properties of regenerated silk fibroin films obtained from different sources The optical properties of regenerated silk fibroin films obtained from different sources,” vol. 103702, 2017.

[32] D. N. Rockwood, R. C. Preda, T. Yücel, X. Wang, M. L. Lovett, and D. L. Kaplan, “Materials fabrication from Bombyx mori silk fibroin,” *Nat. Protoc.*, vol. 6, no. 10, pp. 1612–1631, 2011.

[33] G. Zhou, Z. Shao, D. P. Knight, J. Yan, and X. Chen, “Silk fibers extruded artificially from aqueous solutions of regenerated bombyx mori silk fibroin are tougher than their natural counterparts,” *Adv. Mater.*, vol. 21, no. 3, pp. 366–370, 2009.

[34] J. Yan, G. Zhou, D. P. Knight, Z. Shao, and X. Chen, “Wet-Spinning of Regenerated Silk Fiber from Aqueous Silk Fibroin Solution: Discussion of Spinning Parameters,” *Biomacromolecules*, vol. 11, no. 1, pp. 1–5, 2009.

[35] X. Zhang, I. Vanden Berghe, and P. Wyeth, “Heat and moisture promoted deterioration of raw silk estimated by amino acid analysis,” *J. Cult. Herit.*, vol. 12, no. 4, pp. 408–411, 2011.

[36] W. Lai and K. Goh, “Consequences of Ultra-Violet Irradiation on the Mechanical Properties of Spider Silk,” *J. Funct. Biomater.*, vol. 6, no. 3, pp. 901–916, 2015.

[37] J. Inderherbergh, “Polyvinylidene Fluoride (PVDF) Appearance, General

Properties and Processing," *Ferroelectrics*, vol. 115, no. 4, pp. 295–302, Dec. 1991.

[38] A. Bottino, G. Camera-Roda, G. Capannelli, and S. Munari, "The formation of microporous polyvinylidene difluoride membranes by phase separation," *J. Memb. Sci.*, vol. 57, no. 1, pp. 1–20, 1991.

[39] M. Storzer, P. Gross, C. M. Aegerter, and G. Maret, "Observation of the critical regime near anderson localization of light," *Phys. Rev. Lett.*, vol. 96, no. 6, pp. 1–4, 2006.

[40] E. Abrahams, P. W. Anderson, D. C. Licciardello, and T. V. Ramakrishnan, "Scaling theory of localization: Absence of quantum diffusion in two dimensions," *Phys. Rev. Lett.*, vol. 42, no. 10, pp. 673–676, 1979.

[41] J. ZHAO, J. E. Antonio-Lopez, R. A. Correa, A. Mafi, M. Windeck, and A. Schülzgen, "Image Transport Through Silica-Air Random Core Optical Fiber," in *Conference on Lasers and Electro-Optics*, 2017, p. JTu5A.91.

[42] G. Freddi, R. Mossotti, and R. Innocenti, "Degumming of silk fabric with several proteases," *J. Biotechnol.*, vol. 106, no. 1, pp. 101–112, 2003.

Appendix 1

Related contributed research

A1.1 Temperature of butterfly wing

Insect wings are complex tissues composed of both living and non-living components, and their function requires a suitable range of temperatures. They are strengthened by a characteristic matrix of veins that are closely associated with many mechanical and sensory receptors, and, in some butterfly species, pheromone-producing cells. Wings can rapidly overheat in the sun given their small thermal capacity. We develop an infrared technique to map wing temperatures, and show that despite diverse visible colors and patterns, regions containing living cells are always the coolest. Non-uniform wing thickness and diverse scale nanostructures create a heterogeneous distribution of radiative cooling that largely determines temperature across the wing. A series of assays also demonstrate how butterflies employ specialized behaviors to prevent overheating or overcooling of their wings.

A1.2 Selective solar absorber

A galvanic displacement reaction-based ‘dip-and-dry’ technique is demonstrated for fabricating selectively solar absorbing plasmonic nanostructure-coated foils (PNFs). The technique, which allows for facile tuning of the PNFs’ spectral reflectance to suit different radiative and thermal environments, yields PNFs which exhibit excellent, wide-angle solar absorptance (0.96 at 15°, to 0.97 at 35°, to 0.79 at 80°) and low hemispherical thermal emittance (0.10) without the aid of antireflection coatings. The thermal emittance is on par

with those of notable selective solar absorbers (SSAs) in the literature, while the wide-angle solar absorptance surpasses those of previously reported SSAs with comparable optical selectivities. In addition, the PNFs show promising mechanical and thermal stabilities at temperatures of up to 200°C. Along with the performance of the PNFs, the simplicity, inexpensiveness and environment-friendliness of the 'dip-and-dry' technique makes it an appealing alternative to current methods for fabricating selective solar absorbers.

A1.3 Passive radiative cooling devices based on polymer phase separation

The research study reports a simple, scalable and inexpensive phase-inversion-based method for fabricating hierarchically porous polymer coatings that exhibit high-performance passive daytime radiative cooling (PDRC). The room-temperature and solution-based technique can be applied to various surfaces by conventional approaches like painting and spraying, can incorporate colors, and is compatible with a range of polymers. In particular, hierarchical porous poly(vinylidene fluoride-co-hexafluoropropene) (P(VdF-HFP)HP) coatings created using the technique exhibit excellent, substrate independent hemispherical solar reflectances (0.96 ±0.03) and LWIR thermal emittances (0.97 ± 0.02) which surpass those of notable PDRC designs,4,5,7,9 and allow them to attain a high cooling power of 96 Wm-2 under a solar intensity of 750 Wm-2. Furthermore, P(VdF-HFP)HP coatings show durability under

accelerated thermal, environmental and mechanical tests, and are compatible with colors. The high performance of the coatings, and the simplicity of fabrication, make the method promising as an affordable and eco-friendly way to achieve high-performance PDRC.

Appendix 2

Publications and contributed talks

A2.1 Publications

1) N. Shi, C. Tsai, M. J. Carter, J. Mandal, A. Overvig, M. Y. Sfeir, M. Lu, C. L. Craig, G. D. Bernard, Y. Yang, N. Yu, "Nanostructured fibers as a versatile photonic platform: radiative cooling and waveguiding through transverse Anderson localization" (Accepted, *Light: Science and Applications*)
2) N. Shi, C. Tsai, F. Camino, G. D. Bernard, N. Yu, R. Wehner, "Keeping cool: Enhanced optical reflection and heat dissipation in silver ants" *Science*, vol. **349**, 298-301 (2015)
3) J. Mandal, D. Wang, A. C. Overvig, N. Shi, D. Paley, A. Zangiabadi, Q. Cheng, K. Barmak, N. Yu, Y. Yuang, "Scalable, 'Dip-and- dry' Fabrication of a Wide-Angle Plasmonic Selective Absorber for High-efficiency Solar-thermal Energy Conversion" *Advanced Materials* vol. **29**, 1702156 (2017)
4) Z. Li, Y. Zhou, H. Qi, Q. Pan, Z. Zhang, N. Shi, M. Lu, A. Stein, C. Y. Li, S. Ramanathan, and N. Yu, "Correlated perovskites as a new platform for super broadband tunable photonics," *Advanced Materials* vol. **28**, 9117–9125 (2016).
5) Y. Huang, E. Sutter, N. Shi, J. Zheng, T. Yang, D. Englund, H. Gao, P. Sutter, "Reliable exfoliation of large-area high-quality flakes of graphene and other two – dimensional materials" *ACS Nano* vol. **9** (11) 10612-10620 (2015)

6) J. Zheng, X. Sun, Y. Li, M. Poot, A. Dadgar, N. Shi, H. X. Tang, C. Wong, "Femtogram dispersive L3-nanobeam optomechanical cavities: design and experimental comparison" *Optics Express*, Vol. **20** Issue 24. P 26586 (2012)

A2.2 Contributed talks

1) N. Shi, C. Tsai, C. Craig, N. Yu, "Nano-structured wild moth cocoon fibers as radiative cooling and waveguiding optical materials" Light in Nature VI SPIE Optics + Photonics, San Diego, CA August 7, 2017
2) N. Shi, C. Tsai, C. Craig, N. Yu, "Nano-structured wild moth cocoon fibers as radiative cooling and waveguiding optical materials" CLEO San Jose, CA May 18, 2017
3) N. Shi, C. Tsai, F. Camino, G. D. Bernard, R. Wehner, N. Yu, "Radiative cooling nano-photonic structures discovered in Saharan silver ants and related biomimetic Metasurfaces", CLEO San Jose, CA June 9, 2016